Quick as a flick

All-optical control over ultrafast magnetization writing and spin transport

PROEFSCHRIFT

ter verkrijging van de graad van doctor aan de Technische Universiteit Eindhoven, op gezag van de rector magnificus prof. dr. ir. F. P. T. Baaijens, voor een commissie aangewezen door het College voor Promoties, in het openbaar te verdedigen op woensdag 7 december 2022 om 11:00 uur

door

Youri Louis Winandus van Hees

geboren te Geleen

Dit proefschrift is goedgekeurd door de promotoren en de samenstelling van de promotiecommissie is als volgt:

voorzitter:	prof. dr.	C. Storm	
1e promotor:	prof. dr.	B. Koopmans	
2e promotor:	dr. ir.	R. Lavrijsen	
leden:	dr. ir.	C. F. J. Flipse	
	prof. dr.	T. H. M. Rasing	(Radboud Universiteit Nijmegen)
	prof. dr.	M. Weinelt	(Freie Universität Berlin)
adviseur:	dr.	G. Malinowski	(Université de Lorraine)

Het onderzoek dat in dit proefschrift wordt beschreven is uitgevoerd in overeenstemming met de TU/e Gedragscode Wetenschapsbeoefening.

QUICK AS A FLICK

All-optical control over ultrafast magnetization writing and spin transport

Youri Louis Winandus van Hees

"Really don't mind if you sit this one out"
Jethro Tull – Thick as a Brick (1972)

CONTENTS

vii

1

2

3

4

5

6

7

1

GENERAL INTRODUCTION

Data storage and processing are increasingly important factors for the operation of the modern world. The projected exponential growth of data generation is driving the search for new ultrafast and energy-efficient technologies which can keep pace with these developments. Optical manipulation of magnetic materials is posed to play a significant role in future information technologies. In particular, the revolutionary possibility to write data in magnetic materials with femtosecond laser pulses could drive the next generation of data storage and logic devices. This phenomenon can also readily be combined with the rapidly developing field of photonic integration, providing on-chip data storage at unprecedented speeds.

This chapter provides a brief overview of the current technological challenges and developments that drive research into optical manipulation of magnetic order. The structure of the thesis is discussed at the end of this chapter.

1.1 CHALLENGES IN FUTURE INFORMATION TECHNOLOGY

Throughout human history, developments in the field of communication technology have led to ever increasing interconnectedness. With the advent of the information age in the past century, this process has sped up exponentially. The ease of access to unprecedented amounts of data appears to lead to only more rapid data generation, with seemingly no end in sight. In 2020 alone there were over 10 billion devices connecting to the internet,[1] generating more than 640 trillion GB of data.[2] A main challenge going forward is making sure that data processing capacity keeps up with the increasing rate of generation. Moreover, although a majority of this data is discarded after processing, a significant amount still needs to be stored in a reliable manner. This data often needs to be accessed at a moment's notice, driving demand for ever faster storage technologies. The energy usage of data centers, where massive amounts of data are processed and stored, is already reaching 1 % of the global energy demand;[3] new technologies are desperately needed to prevent energy consumption from growing at the same exponential rates as data generation. More than 10 % of the energy consumption in data centers is taken up by data storage alone,[4] making this an attractive area in which to implement more energy-efficient technologies.

Non-volatility is an essential component for stable long-term data storage. This refers to the capability of a storage device to retain written information when the supply of power is switched off. This capability is intrinsic in magnetically ordered media, making them prime candidates for data storage. Indeed, magnetic *hard-disk drives* (HDDs) have become the storage medium of choice for consumers and businesses alike since their introduction in the 1950s. In these devices, information in the form of bits ('0's and '1's) is encoded by the local orientation of the magnetic moments in a ferromagnetic recording medium. Detection and manipulation of these bits occurs at read/write heads, which contain electrical sensors to read out bits, and electromagnets to write bits via pulsed magnetic fields. The recording medium is contained in a coating on a platter, which is rotated beneath the moving head in order to access data. This need to physically move components is one of the major drawbacks of the HDD, as it requires relatively high amounts of energy and introduces with the risk of mechanical failure. In combination with the inherent speed limits of the electrical schemes used to write and read data, it also leads to typical timescales for accessing data in the order of milliseconds.[5]

As a matter of fact, electronics is proving to be the bottleneck in many data processing devices due to heating issues and crosstalk upon miniaturization of interconnects. An alternative to conventional microelectronics seeing rapid development is the field of *photonic integration*, where data is carried not by electrons, but by photons of light. The idea at the core of photonic integration is to develop and combine elemental photonic building blocks analogous to microelectronic components. Chips which consist of several of these building blocks are referred to as *photonic integrated circuits* (PICs). Crucial components such as on-chip lasers,[6] detectors,[7] and multiplexers[8] have seen continuous development and optimization. Integration of such components has led to an exponential increase of the complexity of these chips over the past decades.[9] This has increasingly given PICs the capability to perform tasks which were previously either relegated to the realm of electronics,[10] or required large and complex optical devices.[11] Specifically in data centers, the call for ever faster data processing can be answered by photonic chips which are capable of efficient operation at large bandwidths.[12] In recent years PICs have already been seeing increased use in data centers in easily integrated commercial modules.[13,14]

However, there is significant latent potential for further on-chip integration of photonics in data centers, in particular in data storage. This still largely takes place in conventional HDDs, which use electrical signals to write data in the magnetic storage medium. As such, an intermediate conversion of information from the photonic to the electronic domain is required before being able to access the storage device, reducing throughput and imposing additional heat generation.[*] The elimination of this conversion step is therefore highly desirable. This requires the capability to write data in a storage medium directly with light propagating in a PIC.

1.2   STORING DATA IN MAGNETIC MATERIALS WITH LIGHT

In certain magnetic materials it is actually possible to write data using only light, using a phenomenon known as *all-optical switching* (AOS).[15–18] This fascinating physical process is triggered by exposing the magnetic material to a light pulse with a duration of mere tens of femtoseconds (fs). A pulse with sufficient energy can then toggle the magnetization between the up ('0') and down ('1') states within only a few ps.[19] As a way to write data, this is orders of magnitude faster than competing technologies, where writing

---

*Solid-state drives (SSDs), where data is stored in electronic flash memory, are seeing increasing use in data centers. Although no second conversion step of information to the magnetic domain is necessary in this case, these devices still require conversion to the electronic domain, with the same associated drawbacks.

Ferromagnet   Ferrimagnet   Synthetic
ferrimagnet
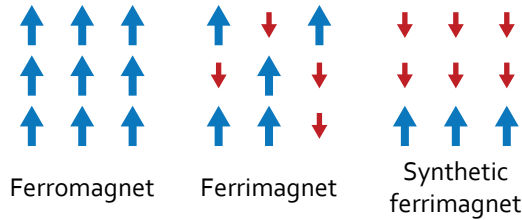
Figure 1.1: Sketch of the ordering of magnetic moments in a typical ferromagnet, disordered ferrimagnet, and (layered) synthetic ferrimagnet. Colors represent different magnetic sublattices.

times of several nanoseconds are already cutting-edge.[5] Additionally, this process is also highly energy-efficient, with energies in the order of tens of femtojoules needed to switch one bit.[20]

AOS is by no means a ubiquitous process; it is known to occur only in very specific *ferrimagnetic* materials. These differ in a key aspect from the more well-known ferromagnets. As sketched in figure 1.1, all magnetic moments in a ferromagnet align in the same direction. In a ferrimagnet there are instead two magnetic sublattices, often composed of different materials, with opposing magnetic moments; in general, the magnetization of these sublattices is not equal. AOS has mainly been discovered in *rare-earth transition metal* (RE-TM) ferrimagnets. Here generally one of the sublattices consists of the RE material Gd, and the other of TM materials such as Co or Fe. Most research into AOS has been performed on disordered RE-TM alloys, such as GdFeCo.[16,17] However, *synthetic ferrimagnets* where the sublattices are separated in different layers can also facilitate AOS, as was first demonstrated with Co/Gd bilayers.[20] The benefit of this class of materials lies in the increased possibilities for device engineering which are opened up by their layered nature.

A potential device that enables storage of data from PICs directly into a magnetic medium with the use of AOS is shown in figure 1.2. In this device, data would be stored in a so-called *racetrack memory* (RTM), where a Co/Gd bilayer is the magnetic storage medium. A striking difference between the RTM and conventional magnetic storage devices such as HDDs or magnetic tape is the absence of any moving parts.[21,22] The magnetic pattern which encodes the data is instead moved along the racetrack using electrical current pulses. Writing data occurs at the intersection of the racetrack and a photonic waveguide, through which an ultrashort light pulse propagates. AOS can occur when this light is locally absorbed by the Co/Gd racetrack, thus writing a bit. Reading out data could also be done all-optically by exploiting magneto-optical effects; interaction
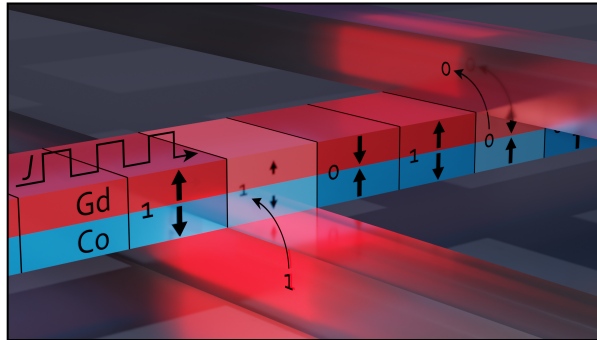
Figure 1.2: Artist's impression of a synthetic ferrimagnetic racetrack memory integrated in a photonic circuit. Data is written to and read from the racetrack with light pulses propagating through photonic waveguides; bits are moved along the racetrack with electrical current pulses.

with the local magnetic moment can for instance modify the polarization of the light propagating through the photonic waveguide, as has recently been demonstrated.[23]

Aside from being easy to engineer for AOS, synthetic ferrimagnets provide another benefit for this device. In order to efficiently move the magnetic pattern through the racetrack, it is critical to tune the net magnetization of the material. More specifically, motion of these magnetic domains is at its most efficient when the angular momentum of the two magnetic sublattices cancels, which is easy to achieve in synthetic ferrimagnets.[24] Typical speeds of hundreds to thousands of m/s, combined with envisioned bit sizes in the order of 50 nm, could see sequential writing speeds of tens of Gbit/s per track. As many tracks could be fabricated in parallel, reading and writing speeds as well as storage capacity are easily scalable.[5] Very low bit access times can also be achieved by including multiple reading and writing interfaces per track. Although most research towards the RTM has focused on electrical reading and writing schemes, a proof-of-principle of an optically addressed Co/Gd racetrack has already been presented.[25] Note that this demonstration made use of free-space optics, and integration with photonics for both reading and writing is still ongoing.

Present research indicates that moving the magnetic domains through the racetrack could be quite a challenge. Large current densities are needed to achieve motion, and pinning of domain walls at the edges of the track is still prohibitive to consistent device operation. A device architecture which circumvents this issue is the *magnetic random-access memory* (MRAM). In such a device, each bit is stored in an individual magnetic pillar and can be addressed at will. Reading bits in these devices is done using

1

electrical currents, making use of tunnel magnetoresistance (TMR), [26,27] hence the term *magnetic tunnel junction* (MTJ) for the individual magnetic pillars. In general bits are also written using current pulses, and commercial devices where this is done using spin-transfer torque (STT) are already on the market. [28] At the same time, spin-orbit torque (SOT) MRAM devices boasting faster writing speeds and lower current requirements are also seeing rapid development. [29] In both kinds of MRAM devices, bits are written by the angular momentum transferred from a spin-polarized current passing either through (STT) or along (SOT) the bit layer. Although there has been significant progress in this field, even the fastest writing times achieved using SOTs are still in the order of hundreds of ps. [30] It has therefore been proposed to use AOS as an ultrafast way to write data in MTJs. [31] Synthetic ferrimagnets are also particularly promising candidates for integration in such devices. In fact, recently a Co/Gd-based optically switchable MTJ compatible with industrial fabrication processes has been demonstrated, yielding writing times of only 10 ps. [32]

A major advantage of MRAM over the RTM is the absence of the latency induced by shifting a bit to a reading or writing device. However, the need for each bit to be individually addressable makes integrating optically-writeable MRAM in photonic chips somewhat more complicated. In principle the electrical signals generated with the conventional TMR reading schemes can be straightforwardly converted back to the photonic domain. For instance, electro-optical switches[33] could be used to reroute light in waveguides based on the bit state. Writing bits on the other hand is more involved, as requiring a separate waveguide for each bit would immensely increase fabrication complexity. One proposed solution is to use gratings to redirect light onto individual MTJs instead. [34]

Although significant strides in understanding have been made in the fifteen years since the discovery of AOS, several questions still remain which are highly relevant for future applications. For instance, while the switching speed of AOS is known (less than 10 ps), [19,35] the rate at which repeated AOS events can take place has scarcely been investigated. Second, the microscopic origin of the switching mechanism is not yet completely understood. It is known that ultrafast laser excitation of magnetic materials can lead to the excitation of mobile electrons carrying a magnetic moment, so-called spin currents. [36] However it remains unclear to which extent such laser-induced spin currents play a role during AOS, which is vital knowledge for future device optimization. Finally, the toggle nature of AOS provides another barrier to implementation in devices. With no consistent way to set a bit, a read or reset step is needed before every writing step, significantly slowing down operation speeds and limiting the potential of AOS.

1.3 OUTLINE OF THIS THESIS

In this thesis, we investigate AOS and ultrafast laser-induced spin current generation in synthetic ferrimagnets with an eye to their applications in the data processing devices of the future. To provide a background for the research presented in this thesis, chapter 2 gives an overview of the history and state-of-the-art of the research in the fields of ultrafast magnetization dynamics, AOS, and optical spin current generation. Chapter 3 describes the experimental concepts and methods used in this work, as well as two theoretical models which are used to deepen our fundamental understanding.

The first novel results are presented in chapter 4, where we endeavour to find the fundamental speed limits of repeated AOS events in synthetic ferrimagnets. In chapter 5 we investigate ultrafast optical spin current generation in synthetic ferrimagnets with the use of collective magnetic excitations, giving additional insight into the role of non-local spin transport in AOS. In chapter 6 we combine AOS and spin currents to provide novel device functionality, resulting in a way to optically write magnetic information in a deterministic manner.

Finally, chapter 7 consists of additional research on engineered synthetic ferrimagnets for high-density data storage, as well as insights into the dynamics of AOS in the presence of external spin currents. This chapter concludes with a general outlook on the applicability of the research presented in this thesis to future spintronic technologies.

2

BACKGROUND OF FEMTOMAGNETISM

Several fascinating physical phenomena can arise when a magnetic material is brought out of equilibrium at the femtosecond timescale. In this thesis we investigate and ultimately combine two of these phenomena, namely all-optical switching (AOS) and laser-induced spin-current generation. To place this work into context, this chapter serves as a summary of the diverse body of research in the field which has arisen in the past decade. First we introduce the field of femtomagnetism with a short discussion of some pioneering experimental and theoretical works. We then present an overview of the history and current state of the art of AOS, as well as existing research into ultrafast optically generated spin currents. The chapter concludes with a brief summary of existing work at the intersection of the two phenomena under investigation.
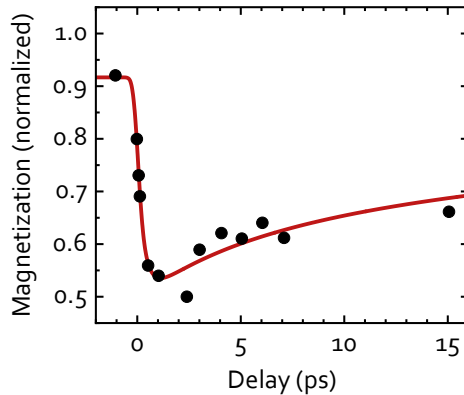
Figure 2.1: Magnetization dynamics of a Ni film after excitation with a fs laser pulse. The red line is a guide to the eye. Figure adapted from ref. 43.

2.1   ULTRAFAST MAGNETIZATION DYNAMICS

All-optical control of magnetization at ultrashort timescales inherently involves rapidly bringing the magnetic system out of equilibrium. Research into general ultrafast non-equilibrium dynamics was facilitated by the emergence of (sub-)ps optical spectroscopy tools in the 1980s.[37–39] Driven both by fundamental interest and a need for better understanding of the hot topic of thermal magnetization writing,[40] this new technique was quickly applied to thermally excited magnetization dynamics.[41,42] Although these measurements were able to probe the interactions between the spins and the lattice, the temporal resolution was insufficient to accurately map the initial excitation.

This was finally resolved in 1996, when Beaurepaire et al. published their results on the fs laser-pulse induced demagnetization of a Ni film.[43] The authors performed *time-resolved magneto-optical Kerr effect* (MOKE) measurements (see section 3.1.3), where the magnetization was measured in the first few ps after exciting the sample with a laser pulse with a duration of approximately 60 fs. The central result of this work, striking and unexpected at the time, is shown in figure 2.1. Here the normalized magnetization is plotted (black circles) as a function of the delay between the excitation (pump) pulse and the measuring (probe) pulse, with the red line serving as a guide to the eye. At the moment when the pump pulse hits the sample, a loss of magnetization occurs in less than a ps. After this initial rapid demagnetization, the magnetic order recovers relatively slowly, with a timescale in the order of tens of ps. The obtained data could be explained using a phenomenological *three temperature model* (3TM), taking into account

the electron, spin, and phonon systems which exchange energy in the form of heat. Here, the assumption was made that the laser pulse initially heats the electron system, which in turn heats up the spin and phonon systems. The temperature of the spin system can be related to the magnetization via a straightforward Curie-Weiss description, where the magnetization tends to zero as it approaches the Curie temperature (T_C). Further equilibration with the phonon system then leads to the relatively slow remagnetization.

Ultrafast laser-induced demagnetization was subsequently reported in several magnetic materials, such as the transition metals Fe and Co,[44,45] several alloys,[46,47] and the elementary rare-earth magnets, Gd and Tb.[48,49] This latter class of materials is of special interest due to their intrinsically slower magnetization dynamics, as we will see in section 2.2. Although the 3TM was to some extent successful in qualitatively reproducing the experimentally observed behavior, the exact mechanism responsible for dissipating the angular momentum of the spins was not discovered. In fact, a comprehensive understanding of the microscopic processes at play has remained elusive to this day. Several possible microscopic origins have been proposed, which can be generally divided into local and non-local explanations. In the former class, local scattering events are taken as the origin of angular momentum dissipation, leading to for instance angular momentum transfer between spin and orbital moments,[50] and electron-electron[51] scattering. In non-local models, demagnetization occurs via the transfer of angular momentum to itinerant magnetic moments, which are able to transport angular momentum away from the demagnetizing material. The proposed processes involved here include spin-dependent scattering of excited electrons,[52] and scattering between localized and itinerant magnetic moments.[53]

Here we highlight one specific local mechanism, namely electron-phonon scattering, which forms the basis of the *microscopic three temperature model* (M3TM).[54,55] As the name suggests, this model is an extension of the 3TM, taking into account a microscopic origin of angular momentum dissipation. The general concept is that an electron-phonon scattering event can cause a spin flip, thereby dissipating angular momentum to the lattice via so-called Elliott-Yafet processes. This model is discussed in more detail in section 3.2.1. The M3TM has been successful in describing a wide range of experimentally observed ultrafast magnetization dynamics. An especially significant results was its ability to capture the noteworthy difference in magnetization dynamics in transition-metal and rare-earth ferromagnets within the same description.[55] Interestingly, dissipation of angular momentum to the phonon system during ultrafast demagnetization has recently been experimentally demonstrated.[56,57]

The successes of the vast array of different models in describing ultrafast magnetization dynamics have made it difficult to reach a comprehensive understanding. In fact, the debate on the dominant microscopic origin of fs-laser-induced demagnetization is ongoing to this day, continually driving new theoretical work as well as novel experimental approaches. Alongside the need for better fundamental understanding, the potential technological impact and applications helped give rise to a diverse field of research into ultrafast laser-induced magnetization dynamics, often dubbed *femtomagnetism*.[58] Of the many phenomena discovered over the years, this thesis focuses mainly on all-optical magnetization writing, and laser-induced spin transport, both of which are introduced in the remainder of this chapter.

2.2   All-optical switching

Perhaps the most obvious application of ultrafast laser-induced changes in magnetization lies in recording data in magnetic materials via heating. In fact, this possibility had already been investigated for decades, albeit not in the ultrafast regime. Shortly after the introduction of the magnetic hard-disk drive by IBM in 1956, the possibility of using heat to record data in a magnetic film was already demonstrated.[59] In this work a hot needle was moved over a MnBi film, which was thereby heated above the Curie temperature, quenching the magnetization(hence the proposed name for the method, *Curie-point writing*). Upon cooling, magnetic order would return in the heated area according to the magnetic stray fields from the surrounding area, yielding a domain magnetized in the opposite direction. Although this particular method was quite slow and somewhat impractical, the concept could readily be extended to other forms of heating, such as electron beams[60] and pulsed laser beams with pulse durations from a few µs to tens of ns.[61–63] The reliance on stray fields to determine the final magnetization state provides limited possibilities for repeated writing of the same area; the use of external magnetic field pulses to set the final state therefore eventually became the standard.

It was soon realized that it is not necessary* to heat the material above the Curie temperature. At this point in time, ferrimagnets found their first entry into the field of *magneto-optical recording*.[65,66] Such materials, which consist of opposing but unequal magnetic sublattices, show a strong peak in the coercive field at the temperature

---

*And in fact not desirable, as temperature increases of hundreds of K are needed to reach the Curie temperature in materials which are suitable for data storage.[64]
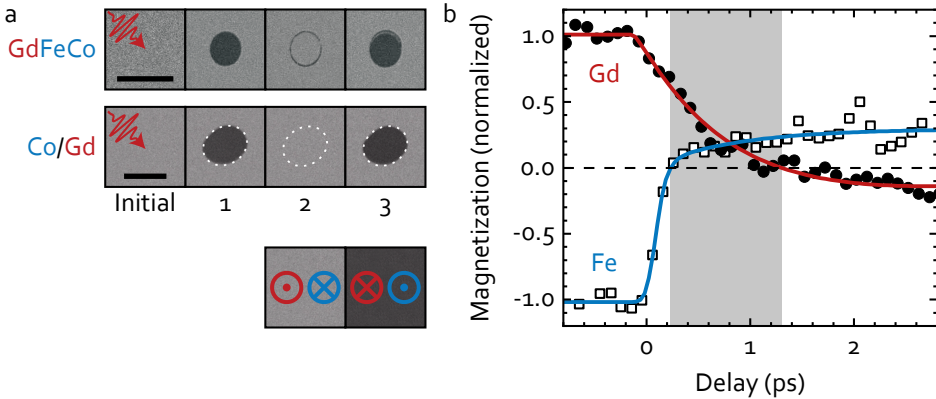
Figure 2.2: (a) Kerr microscopy images with out-of-plane contrast of AOS in a GdFeCo alloy and a Co/Gd bilayer. Scale bars represent 20 and 100 μm respectively. Adapted from ref. [16] and ref. [20]. (b) XMCD measurement of AOS dynamics in a GdFeCo alloy. The gray area indicates the transient ferromagnetic state. Lines are guides to the eye. Adapted from ref. [19].

where the magnetizations of the sublattices cancel each other (the *compensation temperature*). By heating a ferrimagnetic compound engineered to have its compensation temperature at room temperature with a laser pulse, the coercivity rapidly drops. The application of a magnetic field which is stronger than this reduced coercivity, concurrent with the laser pulse, then suffices to switch the magnetization. *Rare-earth transition-metal* (RE-TM) compounds became popular candidates due to the relative ease with which they can be tuned to have the desired compensation temperature.[67–70] These materials found limited commercial success in magneto-optical disk drives,[71] but have since been superseded by granular ferromagnetic media due to a need for high bit stability and compatibility with conventional magnetic storage media. The latest iteration of magneto-optical recording using external fields, known as heat-assisted magnetic recording (HAMR),[72–74] is just now being introduced in commercial hard-disk drives.

Still, RE-TM compounds proved to have another trick up their sleeves with potentially massive implications for magneto-optical recording. In 2007, Stanciu et al. presented surprising results obtained by exciting a GdFeCo alloy with fs laser pulses.[15] Without the application of any external magnetic field, the magnetization was found to reverse fully after exposure to a single 40 fs circularly polarized laser pulse. As the helicity of the laser pulse determined whether or not magnetization switching would occur, the interpretation was that the laser pulse was generating a transient magnetic field via the inverse Faraday effect. The conjecture was that this magnetic field could reverse the strongly quenched magnetization, analogous to field-assisted magneto-optical

recording. However, it was later discovered that upon increasing the laser power, each subsequent laser pulse toggles the magnetization between the two lowest-energy states, and linearly polarized pulses were equally suitable.[16] In figure 2.2a typical Kerr microscopy images (see section 3.1.4) are shown of magnetic domains written with this process, which was named *all-optical switching* (AOS).*

At first glance it seems counterintuitive that a laser pulse carrying no angular momentum is able to induce a coherent flip of magnetic moments. However, the actual mechanism is relatively elegant, and critically depends on the disparate magnetic sublattices in the material. Using *X-ray magnetic circular dichroism* (XMCD), Radu et al. were able to measure the AOS dynamics of a GdFeCo alloy with a pump-probe experiment in an element-resolved manner.[19] The main result of this experiment is shown in figure 2.2b. The ferrimagnetic nature of the material is apparent from the opposite sign of the Gd and Fe magnetization at negative time delay. When the pump pulse arrives, the electrons are rapidly heated, and the magnetization of both Gd and Fe is quenched. However, as discussed in the previous section, Gd intrinsically demagnetizes significantly slower than Fe and Co. This leads to a situation where the Fe magnetization is almost fully quenched while a significant Gd moment still remains. At this point the Fe magnetization crosses zero, creating a transient state where the magnetizations of the two sublattices point in the same direction, indicated by the gray area in the figure. As the Gd continues demagnetizing it is eventually also pushed through zero, which is assumed to be due to the antiferromagnetic coupling between the sublattices. This then results in a state where both of the sublattices have switched sign after less than 2 ps, eventually cooling and returning to saturation after some hundreds of ps.[76–78] Although this last step seems relatively slow, it is possible for a second laser pulse with only a 10 ps delay to induce a second switching event, as shown in chapter 4 and ref. 78.

Perhaps the most puzzling element of this process is the zero crossing of the Fe magnetization. Although the exact microscopic origin is still heavily debated, modelling efforts have convincingly shown that angular momentum needs to be exchanged between the two sublattices in some way. The mechanism for angular momentum transport has often been phenomenologically described with the exchange field between sublattices,[16,79–81] and was made explicit in the m3tm via scattering events between localized electrons.[82] The proposed role of non-local effects involving spin transport via itinerant electrons has been described by an s-d model,[83–85] an extension of which we will also use in this thesis (see section 3.2.2). Experimental work where AOS has been

---

*The helicity-dependence of the pioneering experiment has been explained as magnetic circular dichroism, a difference in light absorption for the two helicities depending on the magnetic state.[75]

achieved with laser pulse durations up to 15 ps[17] has called the necessity of a strongly non-equilibrium electron population into question.[86] However, similar to the issues in explaning ultrafast demagnetization, the exact microscopic mechanism at the heart of AOS has not yet been conclusively resolved.

Since the discovery of AOS in GdFeCo alloys the phenomenon has been observed for other alloys, such as GdCo[87] and GdFe.[78] A downside in all of these alloys is the requirement for a composition such that the magnetizations of the sublattices (nearly) compensate each other.[88] This requirement can prove somewhat limiting with regard to device engineering. However, a different class of systems was shown to be able to forego this requirement. In synthetic ferrimagnets, where the RE and TM sublattices are separated in different layers, the degree of compensation does not significantly seem to matter. AOS in synthetic ferrimagnets was first demonstrated in Co/Gd bilayers, where there was a 5:3 ratio between the magnetizations of Co and Gd.[20] Later it was even shown that these systems could still be switched when replacing the Co layer with a Co/Ni multilayer up to four times thicker.[89] In comparison, research suggests that AOS in GdFeCo alloys is no longer possible when varying the Gd concentration with more than 3-4 % from the compensation point.[88] As discussed in section 1.2, Co/Gd systems have already been successfully used in proof-of-concept spintronic memory devices.[25,32] As such systems are relatively easy to fabricate, and provide more possibilities for optimizing material parameters, they are the main focus of this thesis when it comes to AOS.

In the all-optically switchable systems discussed so far, Gd has been the RE component. However, the low intrinsic anisotropy of Gd makes these systems less suitable for stable data storage. Due to its high spin-orbit coupling, the chemically similar RE material Tb would make a good candidate for high-anisotropy systems.[90] While deterministic toggle-AOS has been achieved in hybrid GdTbCo systems,[35] it has been difficult to achieve in systems without any Gd. So far this has only been successful in Co/Tb multilayers, where the requirement for a very specific material composition reappears.[91,92] This result is somewhat strange, as one might expect that the critical requirements for AOS (antiferromagnetic coupling and exchange of angular momentum, and a difference in demagnetization rate) are still present in these systems. Note that although the magnetization dynamics of Tb are faster than those of Gd,[49,93] they are still significantly slower than those of Co or Fe. This begs the question what exactly the limiting factor is for achieving AOS in Tb-based systems. A potential solution to this conundrum will be discussed in chapter 5; novel hybrid synthetic ferrimagnets exploiting the benefits of both Gd and Tb are presented in section 7.1.
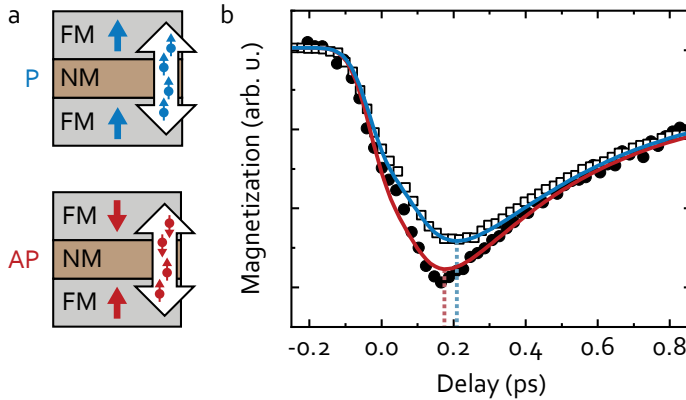
Figure 2.3: (a) Sketch of a magnetic heterostructure used to investigate non-local spin transport. (b) Time-resolved MOKE measurement of the demagnetization of the heterostructure. Lines are guides to the eye. Adapted from ref. 36.

2.3   OPTICALLY GENERATED SPIN CURRENTS

Non-local transport of angular momentum can be a significant factor in a large variety of magnetization dynamics. In fact, experiments on homogeneous precession of magnetic moments in applied fields yielded the first proposal and observation of angular momentum carried by spin-polarized electrons.[94–96] In general there is a high screening efficiency, such that there is no charge transport;[97] the mobile spin-polarized electrons are therefore often termed *spin currents*.

Evidence that ultrafast laser-induced demagnetization could also generate such a spin current was provided in 2008 by Malinowski et al.[36] The system investigated in this work is sketched in figure 2.3a. This system consisted of two ferromagnetic Co/Pt multilayers separated by a non-magnetic, conductive Ru spacer layer of 0.5 to 1 nm. As the ferromagnetic layers were only weakly magnetically coupled, both a parallel and antiparallel alignment of the layers could be obtained by applying an external magnetic field. Figure 2.3b shows a measurement of the laser-induced magnetization dynamics for both the parallel and antiparallel state. Here it can be seen that demagnetization after fs laser pulse excitation is notably faster and stronger in the antiparallel case, giving a strong indication that non-local angular momentum transport is occurring. Confirmation of the role of spin-polarized electrons was obtained with the disappearance of the difference in demagnetization upon replacing the conductive spacer layer with an insulating material, in this case NiO.

Although the origin of these ultrafast spin currents is still hotly debated,[52,98–101] their existence has been proven in other works with similar setups.[102,103] Aside from measuring their effects on other ferromagnets, these spin currents have also been detected via second harmonic generation,[104] via MOKE in the spin accumulation in a thick spacer layer,[99] or in THz excitation occurring in a neighboring heavy metal.[105–108] Moreover, they have been exploited to great effect to influence magnetization dynamics in a variety of magnetic heterostructures. Here we highlight two cases which are particularly relevant for the work presented in this thesis.

In one possible sample geometry, a spin current is injected into an adjacent ferromagnetic layer with its magnetization perpendicular to the spin current polarization. In such a system, the spin current can excite precessional magnetization dynamics, or *spin waves*, in the ferromagnetic layer. This is due to the injected spins acting as a torque on the local magnetic moments, causing a canting and subsequent relaxation to the effective magnetic field with a precessional motion. The simplest case is the excitation of the homogeneous *ferromagnetic resonance* (FMR), where all spins precess with the same amplitude and phase.[99,103] The typical frequencies of such oscillations are in the order of 10 GHz. Moreover, due to the short absorption length of the perpendicular spin current, the canting of the magnetic moments can be inhomogeneous along the layer thickness. This can then result in higher-order spin waves, with frequencies up to 1 THz.[109] Both the FMR and THz spin waves can be used to probe the spin-current characteristics, which in turn are strongly related to the magnetization dynamics of the generation layer.[110]

As hinted at previously, non-local transfer of angular momentum could also play a role in AOS. The strength of the spin current has been shown to scale with the lost magnetic moment;[99] intuitively, a full reversal of the magnetization can be expected to generate massive amounts of mobile spins. In fact it has experimentally been shown that a spin current generated during AOS in a GdFeCo alloy can be strong enough to fully switch an adjacent ferromagnetic layer.[111–113] Here it was deduced from geometric considerations that Gd should be the dominant contributor to the spin current. Quantifying this spin current would be a useful step towards determining the role of non-local effects during AOS, and might clarify why systems containing only Tb are much more difficult to switch. Although some research using alloys has also shown a significant contribution from Gd,[100] a comprehensive picture is still lacking. In chapter 5, analogous to ref. 110, we use FMR and THz spin waves to investigate spin current generation during the ultrafast demagnetization of synthetic ferrimagnets. Here we specifically focus on the differences between Gd and Tb, and reveal strong differences in their behavior.

Finally, one might expect that injecting a spin current, supplying additional angular momentum, into a system undergoing AOS could also strongly affect this process, as it is highly out of equilibrium. Based on the necessity of the transient ferromagnetic state for AOS, optimal switching conditions could be reached by assisting the rapid demagnetization of the transition metal, whilst further slowing down that of the rare earth metal. In chapter 6, we will investigate this scenario in synthetic ferrimagnets, where we show that it can even lead to novel device functionality.

3

METHODS AND TOOLS

The experimental methods and theoretical models that were used in this thesis are introduced in this chapter. The chapter starts with an explanation of the magneto-optical Kerr effect, which is used to probe the magnetization in many experiments. We explicitly discuss the use of this effect for time-resolved magnetization measurements and for microscopy with magnetization contrast. Finally, we discuss two models for ultrafast magnetization dynamics, namely the pioneering microscopic three-temperature model, and an s-d model which allows for the description of non-local dynamics.

3.1   MAGNETO-OPTICAL KERR EFFECT

Magneto-optics provides a straightforward way to probe the magnetization of a magnetic material using light. The first such interaction was discovered in 1845 by Michael Faraday.[114] This *Faraday effect* concerns the change of the polarization of light *transmitted* through a medium in the presence of a magnetic field. A few decades later John Kerr discovered the *magneto-optical Kerr effect* (MOKE), which instead occurs upon *reflection* from a magnetized medium.[115] We will limit the discussion to this latter effect as the samples in this thesis are generally opaque, prohibiting transmission measurements.

In this thesis we will generally use MOKE in the polar geometry, where the magnetization points out of the film, in the same plane as the incident light. This geometry and the polarization of light before and after reflection are sketched in figure 3.1. When a linearly polarized beam of light reflects off a magnetic material, the polarization will become elliptical, and its axis will rotate. These effects are termed Kerr ellipticity and Kerr rotation, respectively. They can be understood by decomposing linearly polarized light into a combination of left- and right-handed circularly polarized light. Initially these components are equal in magnitude and are in phase. However, the interaction of light with a magnetized material is actually dependent on the helicity of that light. A difference in absorption for the two helicities gives rise to the Kerr ellipticity; a difference in propagation velocity gives rise to a phase difference, the Kerr rotation.

The microscopic origin of this effect is to be sought in the coupling of electron spin to the electric field of the light via the spin-orbit interaction.[116] It is however more illustrative to examine the effect at a phenomenological level, for which we show a brief derivation following ref. 117.

In isotropic materials, the interaction between light and the material can be described with the complex refractive index $\tilde{n} = n + i\kappa$, where n is the index of refraction and κ the extinction coefficient. Such materials can also be described with a single dielectric constant $\varepsilon = \tilde{n}^2$. However, in a magnetic field (be it intrinsic or applied) the symmetry is broken, and instead the dielectric tensor $\boldsymbol{\varepsilon}$ is needed. For an isotropic magnetic material lying in the x-y plane this is given by

$$\boldsymbol{\varepsilon} = \begin{pmatrix} \varepsilon_{xx} & \varepsilon_{xy} & \varepsilon_{xz} \\ -\varepsilon_{xy} & \varepsilon_{xx} & \varepsilon_{yz} \\ -\varepsilon_{xz} & \varepsilon_{yz} & \varepsilon_{xx} \end{pmatrix}. \tag{3.1}$$

Now the off-diagonal elements depend on the magnetization, and are responsible
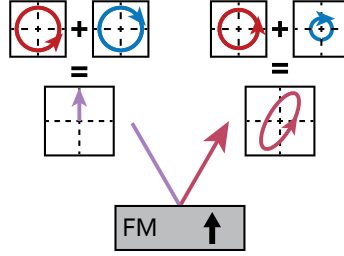
Figure 3.1: Schematic representation of the magneto-optical Kerr effect in the polar geometry. Light reflecting off a magnetic material experiences a rotation of its polarization axis, and becomes elliptically polarized.

for the magneto-optical interaction. We now consider the general case where the magnetization and the path of the incident light both lie along the z-axis, which is valid for most experiments in this thesis. Symmetry arguments then require that the dielectric tensor reduces to

$$\boldsymbol{\varepsilon} = \begin{pmatrix} \varepsilon_{xx} & \varepsilon_{xy} & 0 \\ -\varepsilon_{xy} & \varepsilon_{xx} & 0 \\ 0 & 0 & \varepsilon_{xx} \end{pmatrix}. \tag{3.2}$$

The eigenvalues of this matrix are related to incoming light with left- and right-handed circular polarization, and can be calculated to be

$$\varepsilon_{\pm} = \varepsilon_{xx} \pm i\varepsilon_{xy}. \tag{3.3}$$

Hence, the components making up the linearly polarized light will change relative to each other upon reflection according to $\varepsilon_{+} - \varepsilon_{-} = 2i\varepsilon_{xy}$. The change in polarization, expressed as the complex Kerr effect Θ, can then be calculated to be[118]

$$\Theta = \vartheta + i\eta = \frac{\varepsilon_{xy}}{\sqrt{\varepsilon_{xx}}\left(\varepsilon_{xy} - 1\right)}, \tag{3.4}$$

where ϑ and η correspond to the aforementioned Kerr rotation and Kerr ellipticity, respectively. As the off-diagonal element ε_{xy} depends on the magnetization, this can now be probed by measuring the polarization state of the reflected light.

3.1.1   MEASURING THE MAGNETO-OPTICAL KERR EFFECT

Perhaps the most straightforward way to detect the Kerr effect is to measure the polarization rotation. This can be done by placing polarizers with (nearly) perpendicular axes in the beam before and after reflection, such that the intensity of the beam will be related to the Kerr rotation. However, these effects are generally quite small; the difference in Kerr rotation between opposite magnetization states for the thin film samples used in this thesis is generally in the order of 0.01°. During measurements on laser-induced ultrafast magnetization dynamics, changes in the magnetization can routinely be less than 1%. It is clear that a more sensitive detection scheme is desirable.

Here we turn to polarization modulation, which is done with a *photo-elastic modulator* (PEM) placed into the beam before it reaches the sample. This device modulates the polarization by periodically compressing a birefringent crystal through which the beam passes, inducing a time-dependent phase difference between orthogonal linear polarization directions.[119] A modulation scheme generally provides a better signal-to-noise ratio due to the ability to discard unwanted interference by locking in to the modulation frequency.

The effect of the PEM and its particular usefulness in measuring MOKE can be understood using a matrix formalism, following ref. 120. The time-dependent Jones matrix M describing the PEM is given by

$$M_{\text{PEM}}(t) = \begin{pmatrix} 1 & 0 \\ 0 & e^{A \cos \Omega t} \end{pmatrix},$$ (3.5)

where A is the amplitude of the phase difference between the orthogonal polarization directions, and Ω is the modulation frequency (typically $\Omega/2\pi = 50$ kHz). If the incoming light is linearly polarized with an angle of 45° relative to the axis of the PEM, after passing through the PEM it is described by

$$\begin{pmatrix} E_x \\ E_y \end{pmatrix} = \frac{1}{\sqrt{2}} \begin{pmatrix} 1 \\ e^{A \cos \Omega t} \end{pmatrix}.$$ (3.6)

We now again consider the case of reflection of light off a magnetic material with an out-of-plane magnetization vector, and incidence along this same vector. The induced complex Kerr effect Θ can also be captured in a Jones matrix, namely by

$$M_{\text{FM}} = r_s \begin{pmatrix} 1 & -\Theta \\ \Theta & r_p/r_s \end{pmatrix},$$ (3.7)

where r_s and r_p are complex reflection coefficients for s- and p-polarized light respectively. It can be shown that in order to avoid a time-dependence in the signal in the absence of magneto-optical effects, a second polarizer (or *analyzer*) needs to be placed in the beam after reflection.[121] The intensity I at a detector can then be derived to be

$$I = R\left[\frac{1}{2} + \vartheta \cos\left(A \cos \Omega t\right) + \eta \sin\left(A \cos \Omega t\right)\right], \tag{3.8}$$

where $R = |r_s|^2$, defining the intensity in the absence of magneto-optical interactions. Expanding this in terms of spherical harmonics allows us to separate the constant and time-dependent contributions to the signal. Here it suffices to take the first three terms of the expansion, yielding the constant background intensity I_{DC}, and the intensity change at the frequency and double the frequency of the modulation, I_{1f} and I_{2f} respectively. These components are then given by

$$I_{DC} = R\left(\frac{1}{2} + \vartheta J_0(A)\right), \tag{3.9}$$

$$I_{1f} = \eta R J_1(A) \cos \Omega t, \tag{3.10}$$

$$I_{2f} = \vartheta R J_2(A) \cos 2\Omega t, \tag{3.11}$$

where J_n is the spherical Bessel function of the first kind, of order n.

Aside from the general benefit of any modulation scheme in increasing the signal-to-noise ratio, an additional benefit of using a PEM becomes clear here. By locking in to the modulation frequency, the Kerr ellipticity η can be measured; the Kerr rotation ϑ can be measured by locking in to the second harmonic. The relative magnitude of these two effects can vary strongly for different materials and sample geometries, making it useful to be able to selectively measure one or the other. Moreover, it opens up the possibility to separate the magneto-optical signals from different layers in magnetic stacks, as we will discuss in the following.

3.1.2 COMPLEX MOKE

Several of the samples of this thesis consist of multilayer stacks with two different magnetic subsystems, which can have wildly disparate magnetization dynamics. These two responses combine to make up the total MOKE signal, which often becomes difficult to interpret. It is therefore desirable to be able to disentangle these responses, which can be done using a technique known as *complex MOKE*. We limit the current discussion to a

brief explanation of this technique; a more detailed overview including an experimental demonstration can be found in ref. 103.

The complex Kerr effect Θ_j of layer j can be written as a vector with length Ω_j and angle ξ_j, as

$$\Theta_j = \vartheta_j + \mathrm{i}\eta_j = \Omega_j \mathrm{e}^{\mathrm{i}\xi_j}. \tag{3.12}$$

In this view, ϑ_j can be seen as the projection of Θ_j onto the real axis, whereas η_j is the projection onto the imaginary axis. Now, the signals from the layers combine simply via vector addition, and the total complex Kerr effect is given by $\Theta = \sum_j \Theta_j$. When the magneto-optical responses of the layers have different vector angles ξ_j, it is possible to rotate the projection axes such that one of the vector contributions lies along one of these axes. Measuring the projection along the other axis (using a PEM) then gives a signal that is purely composed of the remaining contributions, which in the case of two layers leads to isolation of a single layer.

A rotation of the projection axes can be effected by the addition of a quarter-wave plate (QWP) in the light beam.* Rotating the fast axis of the QWP by an angle α then causes a rotation of the projection axes. It can be calculated using Jones matrices that the time-dependent intensity components for a single magneto-optical response are now given by:[122]

$$I_{1\mathrm{f}} \propto [\vartheta \sin 2\alpha + \eta \cos^2 2\alpha] \, J_1(A) \cos \Omega t, \tag{3.13}$$

$$I_{2\mathrm{f}} \propto [\vartheta \cos^2 2\alpha - \eta \sin 2\alpha] \, J_2(A) \cos 2\Omega t. \tag{3.14}$$

By choosing α such that the term in brackets vanishes, the magneto-optical contribution is removed from the signal. It is clear that in the case of two separate magnetic layers with different ϑ_j and η_j, the angle α can be chosen to remove the signal of either of the layers.† Generally the Kerr vectors of the separate layers are quite similar, such that some signal is inevitably lost when projecting the isolated layer onto the new axes. However, this is often a small price to pay for the ability to disentangle complex signals in time-resolved measurements.

---

*Perhaps surprisingly, the exact location along the light path does not matter for the qualitative result.
†Note that this comes at the cost of mixing the rotation- and ellipticity-induced signals from the remaining layer. Especially during ultrafast demagnetization, these can behave quite differently.[123]
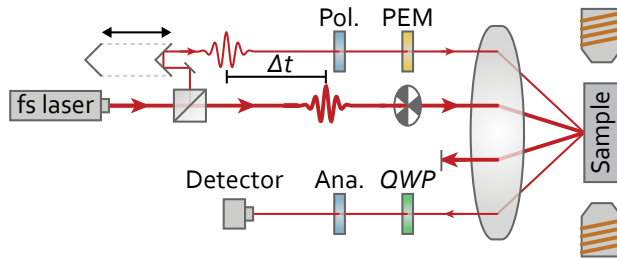
Figure 3.2: Sketch of a typical setup for time-resolved MOKE measurements. The quarter-wave plate (QWP) is only used in complex MOKE.

3.1.3   Time-resolved MOKE

Having discussed all elements necessary to measure MOKE, we now discuss the application of these techniques to measuring ultrafast laser-induced magnetization dynamics. A sketch of a general setup used to measure *time-resolved MOKE* is shown in figure 3.2. Both to excite and measure the magnetization dynamics, we start with a laser capable of generating pulses with sub-ps durations. In this thesis, two different laser systems are used. For 'low-fluence' measurements where a high signal-to-noise ratio is required we use a mode-locked Ti:Sapphire laser generating pulses with a duration of ~ 100 fs at sample position, at a repetition rate of 80 MHz. The central wavelength of this system is 780 nm, and the typical pulse energy is in the range of 1 to 10 nJ. In order to achieve all-optical switching, and measure the process in a time-resolved manner, higher pulse energies are required. In this case we use a pumped diode laser with a variable repetition rate up to 500 kHz, which in turn pumps a non-linear optical parametric amplifier tuned for a central wavelength of 700 nm. The pulse duration for this system is similar, but the pulse energy can be as high as 1.5 μJ.

In order to use the same laser to excite and probe the magnetization, the pulses are split by a beamsplitter. As only very little energy is needed in the *probe* pulse, the reflection of this beamsplitter can be as low as 5 %. The path of the probe pulse contains several optical elements. The polarizer and PEM have been introduced previously, and are vital to measure small changes in magnetization with a high signal-to-noise ratio. A lens is used to focus the probe pulse onto the sample, which is placed between electromagnets to generate magnetic fields where necessary. The reflected pulse is captured using the same lens and passes through the optional QWP for complex MOKE, and the analyzer. Finally, the pulse is detected by a photodetector. The signal at this photodetector consists of a train of pulses at the repetition rate of the laser. This signal

is fed to a lock-in amplifier (LIA) locked to the first or second harmonic of the PEM modulation frequency. However, in order to map the magnetization dynamics, it is necessary to be able to vary the time delay between the arrival of the pump and probe pulses. This is achieved with the delay line, consisting of a retroreflector on a moveable stage, placed in the probe path. Delay stages with translational accuracies in the order of 1 µm are readily available, giving a time resolution of 6.7 fs. As this is significantly smaller than the pulse duration, the latter is typically the limiting factor in the temporal resolution of the experiment.

The path of the *pump* pulse, consisting of the remaining 95 %of the original pulse intensity, is more straightforward. It is only used to excite the magnetization dynamics, and therefore simply needs to be focused onto the sample in the same location as the probe pulse using the same lens. When the pump and probe pulses enter the lens along parallel paths, alignment of the pulses on the sample is guaranteed when the sample lies in the focal plane of the lens. However, care needs to be taken to avoid the reflected high-intensity pump pulse from reaching the detector, as even with modulation this soon drowns out the signal from the probe pulse.

In order to increase the signal-to-noise ratio further, a double modulation technique is often employed. This is also sketched in figure 3.2, where the second modulation takes place in the pump path in the form of an optical chopper. This device periodically blocks the pump pulses, typically with a frequency between 50 to 500 Hz. The output of the LIA that is used to demodulate the probe signal is fed into a second LIA which is locked to the frequency of the chopper. The output of this system now consists of only that part of the signal which is modulated at both the PEM and the chopper frequency. This is made up precisely of the probe pulses arriving during the time intervals where the pump pulses are allowed to reach the sample. In this way, only the pump-induced changes of the magnetization are measured.

3.1.4   Kerr microscopy

In typical all-optical switching (AOS) experiments it is necessary to image the magnetic state of a sample after exposure to fs laser pulses. Although this can in principle be done by scanning a probe beam over the surface of a sample, this is a time-consuming process which is limited in resolution by the spot size of the probe beam (typically no smaller than 5 µm). As an alternative we use a wide-field microscopy technique which has been developed to optically image magnetic domains; this is typically referred to as *Kerr*
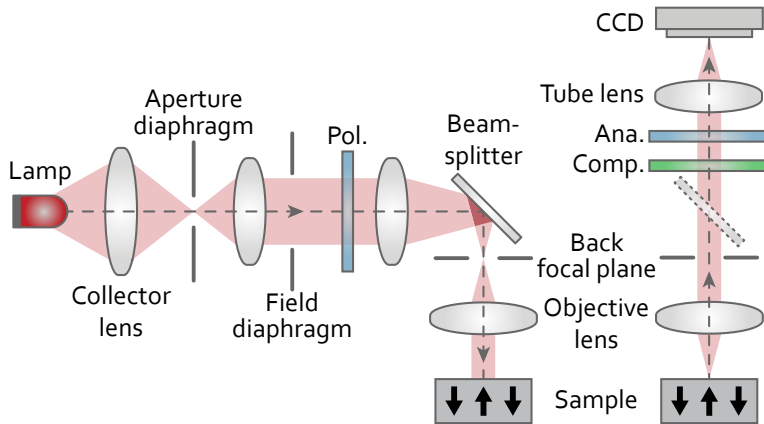
Figure 3.3: Sketch of a typical setup for Kerr microscopy to image out-of-plane magnetization in the case of perpendicular incidence. Based on ref. 124.

microscopy. We now briefly explain the components needed, following the discussion in ref. 124.

A typical setup for Kerr microscopy is shown in figure 3.3, where the path of the incoming light is shown on the left, and that of the reflected and captured light on the right. Light which is generated by a stable, high-intensity lamp is focused by the collector lens in the plane of the aperture diaphragm. This diaphragm is responsible for selecting the maximum angle of incidence of the rays which are allowed to reach the sample. In the case of imaging out-of-plane magnetization (polar geometry), the light should impinge (nearly) perpendicular to the sample. Therefore the aperture diaphragm is closed as much as possible while retaining enough light for proper imaging. Centering the aperture in the beam means that the net angle of incidence is zero, resulting in only out-of-plane magnetization contrast. Conversely, in-plane magnetization contrast can be achieved by aligning the diaphragm off-center with respect to the beam.

Next, the light passes through the field diaphragm, which is used to select the area of the sample that is illuminated. After passing through a polarizer, half of the light is deflected by a beamsplitter. The light is then collimated and directed onto the sample through the objective lens. After reflection this light, having experienced the Kerr effect and serving as a probe of the magnetization, now needs to be captured. When the sample lies in the focal plane of the objective lens, the reflected light is collimated by this same lens. It therefore determines the field of view, and as it can be readily swapped out, different levels of magnification can be obtained. The field of view can be

varied from mere tens of μm up to 1 cm, which is especially useful for imaging arrays of all-optically switched domains.

Half of the collimated light passes through the beamsplitter, and reaches the compensator and analyzer. In the absence of any modulation schemes, the polarization axis of the analyzer is generally (nearly) perpendicular to that of the initial polarizer. The compensator is typically a QWP, and can be used to convert the polarization of reflected light from elliptical to linear in order to obtain the highest possible attenuation by the analyzer. Finally the light is focused onto a CCD camera, generating a signal which can be digitally processed to maximize the magneto-optical contrast. One of the most common processing methods involves imaging an area of the sample where the magnetization is homogeneous. This image can then be saved, and subtracted from the live signal. Artefacts introduced to the live signal by the optics of the microscope are then effectively cancelled out.

The maximum resolution of a Kerr microscope depends on the wavelength of the illuminating light and the numerical aperture of the optics used, but is typically in the range of 0.5 to 1 μm. This is generally more than sufficient to image domains that have been all-optically switched, which usually have diameters in the order of tens of μm.

3.2   MODELING ULTRAFAST MAGNETIZATION DYNAMICS

Several models have been developed over the years in attempts to microscopically describe ultrafast laser-induced magnetization dynamics. In these complex systems, some abstractions always have to be made, taking care to discard as few essential elements as possible while retaining the core behavior. Although many efforts have been made with local[50] and non-local descriptions,[52] a fundamental understanding is still lacking. However, such models can still be very illustrative in the situations where their particular description approximates reality to a useful degree. In this section we discuss two models which are used in this thesis to simulate all-optical switching and spin transport, namely the *microscopic three-temperature model* (M3TM) and an *s-d model*.
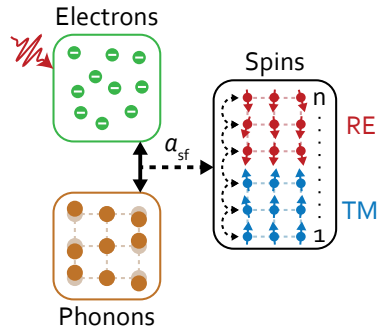
Figure 3.4: Schematic representation of the layered M3TM. The (spinless) electron system is heated by a laser pulse, and exchanges energy with the phonon system. Electron-phonon scattering events cause spin flips in the spin system, where angular momentum is transferred between layers via exchange scattering.

3.2.1 Microscopic three temperature model

As was discussed in section 2.1, the M3TM[55] can be seen as an extension of the very phenomenological three-temperature model (3TM), which was used by Beaurepaire et al. to describe their experimental observations.[43] In the M3TM, there is still an exchange of energy between the subsystems, but angular momentum dissipation in the spin system is now described with microscopic processes. The system has also been extended to describe layered stacks with different magnetic materials. In the following we will give a brief overview of the approaches to the subsystems, and show the resulting equations. A more in-depth treatment of the general M3TM can be found in ref. 121; a description of the layered extension is available in ref. 122.

Figure 3.4 shows a schematic representation of the three subsystems in the M3TM, namely the electron, phonon, and spin systems. The spinless mobile electron system, which is the only system initially excited by the laser pulse, is described as a free electron gas with a constant density of states. This results in a microscopic description for the heat capacity of the electron system, which is an improvement on the purely phenomenological description of the 3TM with regard to consistency with experimental results. The same is true for the phonon system, which is described by a Debye model. It is often assumed that the spin system, consisting of localized electronic magnetic moments, has a negligible heat capacity.

In that case transfer of energy is purely between the electron and phonon systems, which can then be described as temperatures T_e and T_p with the following differential equations:

$$\gamma T_e \frac{dT_e}{dt} = g_{ep}\left(T_p - T_e\right) + P(t), \tag{3.15}$$

$$C_p \frac{dT_p}{dt} = g_{ep}\left(T_e - T_p\right) + C_p \frac{T_{amb} - T_p}{\tau_d}. \tag{3.16}$$

Here the heat capacities are the temperature-independent C_p for the phonon system, and $C_e = \gamma T_e$ for the electron system, with γ a material-dependent constant. The parameter g_{ep} describes the efficiency of energy transfer between the subsystems. The heating induced by the laser pulse is represented by the term $P(t)$ in the electron system, which is typically a Gaussian function. Heat diffusion away from the lattice is phenomenologically described by the last term in the equation for the phonon temperature, where T_{amb} is the ambient temperature and τ_d a typical timescale.

A Weiss mean-field model is used for the spin system, with the assumption that the spin quantum number $S = 1/2$.* The angular momentum of the spin system is transferred to the lattice by an Elliott-Yafet mechanism, where scattering events between electrons and phonons can, with a certain probability a_{sf}, cause a spin to flip between up and down. The scattering probabilities can be evaluated using Fermi's golden rule. In the case of a single magnetic system, this yields a single differential equation for the normalized magnetization m:

$$\frac{dm}{dt} = Rm\frac{T_p}{T_C}\left[1 - m\coth\left(m\frac{T_C}{T_e}\right)\right]. \tag{3.17}$$

Here the demagnetization rate is governed by the parameter R:

$$R = \frac{8\,a_{sf}\,g_{ep}k_B T_C^2 V_{at}}{\left(\mu_{at}/\mu_B\right)E_D^2}. \tag{3.18}$$

This now contains only parameters which can be found in literature or extracted from experiments. Specifically, k_B is the Boltzmann constant, μ_{at} and μ_B the atomic magnetic moment and Bohr magneton respectively, and T_C the Curie temperature. V_{at} is the atomic volume, and E_D the Debye energy.

---

*Although not fully correct for materials such as Gd ($S = 7/2$), which require a more complicated implementation,[89] the discrepancy is subtle and generally does not impact qualitative results.

In order to describe AOS in (layered) synthetic ferrimagnets, an extension to the model is needed. Instead of treating only one magnetic system, we now consider the magnetic system to consist of atomic monolayers. Different material parameters can then be assigned to each of these layers.

Although the magnetization within the layers can in principle be calculated in the same manner as before, there is now the possibility within the Weiss model for the atoms in layers to 'feel' a different environment according to the composition of their neighboring layers. This is described by the exchange splitting $\Delta_{ex,i}$ for each layer i. Taking into account the nearest neighbors in an fcc lattice (6 and 3 in the own and adjacent layer respectively), the exchange splitting can be described as.

$$\Delta_{ex,i} = 2k_B \left(\frac{3T_{C,i-1}\, m_{i-1} + 6T_{C,i}\, m_i + 3T_{C,i+1}\, m_{i+1}}{12} \right). \tag{3.19}$$

Note that for neighboring layers, the parameter $T_{C,i\pm1}$ is not strictly the Curie temperature of that layer. Instead it is related to the coupling strength $J_{i\pm1}$ between layers via $J_{i\pm1} \propto k_B T_{C,i\pm1}$. As such, a positive (negative) $T_{C,i\pm1}$ denotes parallel (anti-parallel) coupling between layers.

Using this description, we arrive at a set of equations for the normalized magnetic moment per monolayer m_i by rewriting equation (3.17) as

$$\frac{dm_i}{dt} = R_i T_p \frac{\Delta_{ex,i}}{2k_B T_{C,i}^2} \left[1 - m_i \coth\left(\frac{\Delta_{ex,i}}{2k_B T_e} \right) \right]. \tag{3.20}$$

Next, an additional channel for angular momentum transport is introduced in the form of electron-electron scattering events between layers, referred to as *exchange scattering*, and indicated by the dotted arrows in the spin system in figure 3.4. This describes events where two electrons from different layers scatter and both flip their spin, resulting in a change in energy $\Delta_{ex,i,i\pm1}$ given by

$$\Delta_{ex,i,i\pm1} = \Delta_{ex,i} - \Delta_{ex,i\pm1}. \tag{3.21}$$

To calculate the transition probabilities according to this energy difference, a standard integral (SI) over the electronic transition needs to be solved; this integral is quite complex and therefore approximated numerically.[122] We denote the standard integral over the electronic states when a scattering event results in either a gain or a loss of energy as $SI_{\pm}$.

It can then be derived that the magnetization dynamics per monolayer as governed by exchange scattering with each of the neighboring layers $i \pm 1$ are described by

$$\frac{\mathrm{d}m_i}{\mathrm{d}t} = \frac{\eta_{i,i\pm1}}{\left(\mu_{\mathrm{at},i} / \mu_\mathrm{B}\right)} T_\mathrm{e}^3 \left[-\mathrm{SI}_- \left(\frac{1 + m_i}{2}\right)\left(\frac{1 - m_{i\pm1}}{2}\right) \right.$$
$$\left. + \mathrm{SI}_+ \left(\frac{1 - m_i}{2}\right)\left(\frac{1 + m_{i\pm1}}{2}\right) \right].$$

(3.22)

The efficiency of the exchange scattering is given by the dimensionless parameter $\eta_{i,i\pm1}$. The magnetization dynamics due to interlayer exchange scattering for each layer are then described by two differential equations, one for each neighboring layer.

The total magnetization dynamics for each layer are now obtained simply by adding the differential equations for intra- and interlayer dynamics, equations (3.20) and (3.22). Note that the electron and phonon temperatures are assumed to be constant across all layers, and can therefore be described with one parameter each for the entire system. This assumption is generally valid for systems where the electron equilibration time is not much larger than the timescale of heat diffusion across the film. For thin film systems these are typically both in the order of hundreds of fs.[55,125]

The M3TM has been successful in quantitatively reproducing ultrafast demagnetization experiments,[55] and can qualitatively model all-optical switching in alloys and layered systems.[89] However, as it only takes into account interactions between localized spin moments, it is not suitable to investigate spin transport. For this purpose, we now discuss a different approach, where the magnetic moment carried by itinerant electrons is also taken into account.

3.2.2   S-D MODEL

For cases where non-local spin transport between magnetic subsystems is a significant factor, we use an s-d model as described in ref. 101. The general idea of this model is sketched in figure 3.5. Akin to the M3TM, the system is separated into three subsystems. The basic description of the subsystems is similar, with the free electron gas, and Debye and Weiss model descriptions for the electron, phonon, and spin (localized electron) systems, respectively. There are however some key differences. Firstly, the mobile or itinerant electrons are no longer assumed to be spinless, and can carry angular momentum in conjunction with the localized electron system. Dissipation of the angular
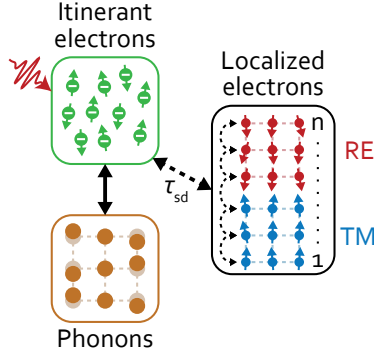
Figure 3.5: Schematic representation of the layered s-d model. Here the itinerant electrons also carry spin, and can exchange angular momentum with the localized electrons via s-d scattering.

momentum of the localized electrons now occurs not via electron-phonon scattering, but via scattering with the itinerant electrons.

As a thorough derivation of the basic model can be found in 101, we turn immediately to the resulting equations in the layered extension, analogous to the M3TM. The angular momentum carried by the itinerant electrons is described as a spin accumulation $\mu_{s,i}$ which is generated by each monolayer i. The time-evolution of this term is described as

$$\frac{d\mu_{s,i}}{dt} = \rho_{sd,i} \frac{dm_{d,i}}{dt} - \frac{\mu_{s,i}}{\tau_{s,i}}.$$ (3.23)

Here ρ_{sd} represents the scattering efficiency between localized and itinerant electrons, m_d is the moment carried by the localized electrons, and τ_s a timescale for the scattering events that dissipate angular momentum from the itinerant electrons. For our purposes we can simplify the general model by assuming that the total thickness of the magnetic system is small. In this case the generated spin instantaneously equilibrates across the structure, and diffusive transport can be neglected. Therefore the individual contributions to the spin accumulation simply sum up to a single μ_s. The moment per layer carried by the localized electrons is then described by

$$\frac{dm_{d,i}}{dt} = \frac{1}{\tau_{sd,i}} \left(m_{d,i} - \frac{\mu_s}{2k_B T_{C,i}} \right) \left[1 - m_{d,i} \coth\left(\frac{2m_{d,i} k_B T_{C,i} - \mu_s}{2k_B T_e} \right) \right].$$ (3.24)

Here the timescale $\tau_{sd,i}$ is similar to the previously discussed demagnetization rate R. It is interesting to note that in the limit where $\tau_{sd} \gg \tau_s$, the spin accumulation will

disappear instantaneously. The form of equation (3.24) then becomes strikingly similar to the M3TM, even though the microscopic processes responsible for angular momentum dissipation are different.

The s-d model has indeed been successful in describing several experimental results regarding ultrafast magnetization dynamics where spin transport plays a role. For instance, the demagnetization of a ferromagnet interfaced with a conductive metal acting as a receptacle for itinerant electrons is correctly reproduced.[101] Most relevant for this thesis, all-optical switching[84,85] and experiments concerning spin transfer between magnetic layers, such as the experiment of Malinowski et al.[36] (figure 2.3) can also be reproduced with the model.

4

RAPIDLY REPEATED ALL-OPTICAL SWITCHING IN SYNTHETIC FERRIMAGNETS

Although all-optical switching with fs laser pulses has garnered much technological interest, the ultimate data writing rates achievable in synthetic ferrimagnets have not been investigated at all. In this chapter we investigate the minimum time delay required between two subsequent switching events in synthetic ferrimagnetic Co/Gd bilayers using two fs laser pulses. We experimentally demonstrate that the minimum time delay needed for consistent switching can be as low as 10 ps. Moreover, we demonstrate the importance of engineering heat diffusion away from the magnetic material, as well as control over the laser pulse energy. This behavior is reproduced using modelling, where we find that the second switch can occur even when the magnetization is not fully recovered. We further confirm that heat diffusion is a critical factor in reducing the time delay for the second switch, while also confirming a critical dependence on laser energy.

4.1 Introduction

All-optical switching (AOS) of the magnetization of thin film ferrimagnets using single femtosecond laser pulses has been demonstrated to be a robust, ultrafast, and energy efficient method to write data with promise for future memory devices.[18] The mechanism was first discovered in ferrimagnetic GdFeCo alloys,[15–17,75,127] and was soon followed by demonstrations in synthetic ferrimagnets (Co/Gd and Co/Tb).[20,91] The switching was shown to be symmetrical, with each subsequent laser pulse toggling the magnetization between the 'up' and 'down' states, a process which can be repeated over hundreds of millions of cycles without failure.[77] The energy efficiency of AOS is especially interesting for applications, with typical energies of only tens of fJ needed to switch nanoscale bits.[20,128] Moreover, the magnetization only takes a few picoseconds to cross zero,[19,35] potentially implying near THz writing speeds. However, this is not the most relevant timescale for determining the ultimate data rates, as it is expected that the magnetization should relax to the opposite state after each switching event to facilitate the next switch. This remagnetization process can potentially take hundreds of ps,[77] and is expected to be governed by heat diffusion away from the magnetic layers.[45]

Despite the large body of research into AOS, understanding of the ultimate speed with which subsequent switches can actually take place remains scarce.[129] It has been shown experimentally that a second fs laser pulse can consistently switch the magnetization in a GdFeCo alloy again after 300 to 400 ps.[130] Here it was conjectured that this is likely not a fundamental limit of the switching process but rather a limit imposed by heat diffusion. Very recently it was demonstrated by Steinbach et al. that this is indeed the case, with a minimum possible waiting time of 7 ps in a GdCo alloy when a substrate with proper heat conductivity is used.[78] The remagnetization time of the alloy was emphasized by the authors as a critical factor for facilitating the second switch. In this light, one might expect longer waiting times between switches in technologically highly relevant synthetic ferrimagnets,[24,131,132] where the magnetic sublattices are less strongly coupled and therefore expected to remagnetize slower after AOS than in alloys.[133]

In this chapter we experimentally demonstrate that by taking into account the heat diffusion of the sample, switching events can take place with very short delays even in synthetic ferrimagnetic Co/Gd systems. The minimum time delay for the second pulse to consistently switch the magnetization is found to be as low as 10 ps, yielding potential writing rates of up to 100 GHz. The importance of the heat diffusion in this process is highlighted by demonstrating a larger minimum time for a substrate with
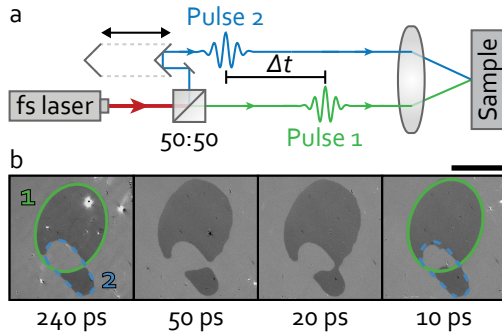
Figure 4.1: (a) Sketch of the experimental setup, colors are for illustrative purposes only. (b) Kerr microscopy images of the magnetic state of a Si:B//Ta(4)/Pt(4)/Co(1)/Gd(3)/TaN(4) sample after exposure to two ~ 100 fs laser pulses with varying time delay. The green and blue lines enclose the areas that would be switched by the two pulses individually. The scale bar represents 50 μm.

lower heat conductivity. Moreover, the absence of rapid double switching when slightly increasing the energy of the first pulse highlights the need for careful control of the irradiation conditions. Finally, we present modelling results using the Microscopic Three Temperature Model (M3TM)[89] confirming that heat diffusion is the dominant factor in reducing the delay for the second switch, and also illuminating the critical role of the laser pulse energy.

The experiments in this chapter are performed on Ta(4)/Pt(4)/Co(1)/Gd(3)/TaN(4) multilayer stacks (where numbers in parentheses indicate layer thickness in nm) known to exhibit AOS,[20] which are deposited on Si substrates using DC magnetron sputter deposition. These stacks are deposited on a degenerately Boron doped Si substrate, which should have similar thermal conductivity to the substrates used in previous work.[78] As sketched in figure 4.1a, individual ~ 100 fs laser pulses with a central wavelength of 700 nm are split in two using a 50:50 beam splitter, after which one pulse goes through a delay line so that the time delay between the two pulses can be adjusted. Both pulses are subsequently focused onto the sample via the same objective. The magnetic state of a sample after exposure is imaged using an ex situ Kerr microscope.

4.2   Experimental results

The magnetic state of the sample after exposing different regions to sets of two pulses with varying time delays is shown in figure 4.1b. Here, the regions that would be switched by the first and second pulse separately are indicated by the solid green and dashed blue shapes, respectively. For the longest time delay shown here (240 ps) a clear region within the overlap of the two pulses is observed where the magnetization is switched twice, returning to the initial state. This is comparable to previous work on GdFeCo alloys, where the second switch was possible after 300-400 ps.[130] Moreover, comparable to recent work on GdCo[78] we find that double switching also occurs when reducing the time delay to 50 ps, and even stays possible for time delays as low as 10 ps. As will be discussed later, this result is somewhat surprising, as magnetization recovery is expected to be faster in alloys than in synthetic ferrimagnets, where the magnetic sublattices are only coupled at the interface, and the Gd magnetization shows a stronger temperature dependence. Comparing the images for 240 and 10 ps time delay, we note the shrinkage of the region where double switching occurs for the shortest time delay, indicating a more critical dependence on the exact laser fluence of the two pulses. Switching in the region where the second pulse is below threshold, as was observed in similar experiments on GdFeCo,[130] has not been observed in the present research.

To investigate the effect of heat diffusion on the minimum double switching time, we now turn to a substrate with lower heat conductivity. A Ta(4)/Pt(4)/Co(1)/Gd(3)/TaN(4) stack is deposited on a silicon substrate with a 100 nm coating of SiO_2. The oxide layer is expected to be less efficient in conducting heat away from the metallic multilayer stack than the semimetallic Si:B substrate. Remagnetization therefore is expected to be slower, and the minimum time needed between two pulses for consistent switching should be larger. Although exact values of the thermal conductivity of the substrates are not known, the negative effect of the Si/SiO_2 is illustrated with experiments which are presented in appendix A.

We perform the same experiment presented in figure 4.1 on the multilayer stack grown on the Si/SiO_2 substrate, the result of which is shown in figure 4.2a. The areas switched by the two pulses separately are again indicated with solid green and dashed blue lines in the Kerr microscope image for 150 ps time delay. Note that although the total energy of the two laser pulses is identical, the first pulse has a narrower spatial distribution. This leads to a higher maximum in the energy density, which falls off more rapidly, resulting in a smaller switched area. Consistent double switching is again observed for time delays down to 20 ps. However for a time delay of 10 ps, where
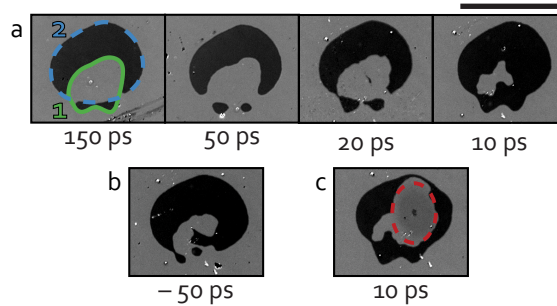
Figure 4.2: Kerr microscopy images of the magnetic state of a Si/SiO$_2$/Ta(4)/Pt(4)/Co(1)/Gd(3)/TaN(4) sample after exposure to two ~100 fs laser pulses with varying time delay. The solid green and dashed blue lines enclose the areas that would be switched by the two pulses individually. The scale bar represents 50 μm. In (a) and (c), pulse 1 arrives before pulse 2, whereas in (b) pulse 2 arrives first. The total energy of pulse 2 is 10 % higher in (c) than in (a) and (b). The red dotted ellipse in (c) indicates the area where the effect of the combined heating of both pulses was high enough to induce magnetic and/or structural damage.

double switching was possible previously, different behavior is observed. Only a small part of the area where both pulses overlapped has returned to the initial state, with this area being rather complexly bounded. This is an indication that this area is actually not consistently switched twice, but rather remagnetized in a random state after cooling down. Such a process can occur when the temperature of the lattice exceeds the Curie temperature for a longer time, leading to a complete loss of magnetization for a short period of time.[17] This observation is consistent with the expectation that heat remains in the system for a longer time when heat transfer is impeded by the oxide coating.

To illustrate the sensitivity of the double switching process, figure 4.2b shows the result of exposure when the order of the two pulses is swapped. For a delay as large as 50 ps, a more random state is found in the overlapping region, indicating a critical dependence on the energy density distribution of the two laser pulses. More specifically, when the pulse with higher maximum energy density ('pulse 1') arrives last, double switching is less consistent. This can again be understood by realizing that by strongly heating the sample with the second pulse before the heat from the first pulse has significantly dissipated, the lattice temperature can exceed the Curie temperature. As an additional demonstration of the criticality of the laser pulse energy, we increase the total energy of pulse 1 by as little as 10 %, leading to the magnetic state shown in figure 4.2c. Here we find a region (indicated by the red dashed ellipse) where the magnetic properties of the sample have changed due to laser irradiation. Both the

small dark dot in the center of this region as well as the lighter area around it have been annealed by the combined effect of both laser pulses, and can not be switched again with either a laser pulse or an external magnetic field. This indicates the high temperature of the sample, and further highlights the importance of proper heat engineering.

4.3   MODELING RESULTS USING THE M3TM

To better understand double switching at these ultrashort timescales we turn to modelling, which has been used to describe AOS in (synthetic) ferrimagnets.[16,79–81,85,86,134] Here we use the simplified Microscopic Three Temperature Model (M3TM) as introduced by Beens et al.,[89] which can describe AOS in layered ferrimagnets. In this model, the system is split in four interacting systems, namely separate spin systems for Co and Gd, mobile spinless electrons, and phonons. The two spin sublattices carry the magnetization, and are described using a Weiss mean-field approach, whereas the electrons and phonons are described in terms of temperatures. An incident laser pulse is initially absorbed by the electron system, raising the electron temperature (T_e). Due to electron-phonon scattering, the electron and phonon temperature (T_p) will equilibrate. Ultrafast demagnetization occurs via electron-phonon scattering events, which have a finite probability for an electron to flip its spin. Exchange of angular momentum between the magnetic sublattices is described using exchange scattering. The model parameters are taken from Beens et al.[89] Similar to previous work,[129] we include heat diffusion to the substrate by adding a phenomenological term to the phonon temperature, namely

$$\frac{\mathrm{d}T_p}{\mathrm{d}t} \propto \frac{T_{amb} - T_p}{\tau_d},$$

(4.1)

where T_{amb} is the ambient temperature (room temperature), and τ_d a characteristic time constant for heat diffusion. Although the timescale for full thermal relaxation can be many hundreds of ps,[78] this is not necessarily the timescale that needs to be considered here. Instead, strong absorption in the metallic film leads to a first, fast equilibration process with the cooler substrate, which can already have an effect within a few ps (see appendix A.2). It is this timescale which is of relevance to understand the experimental behavior, where the thermal conductivity is found to have an effect on repeated AOS within tens of ps. Therefore, τ_d is chosen in this same order of magnitude. We emphasize that it is difficult to make precise qualitative statements using this approach, and only investigate trends in the following.
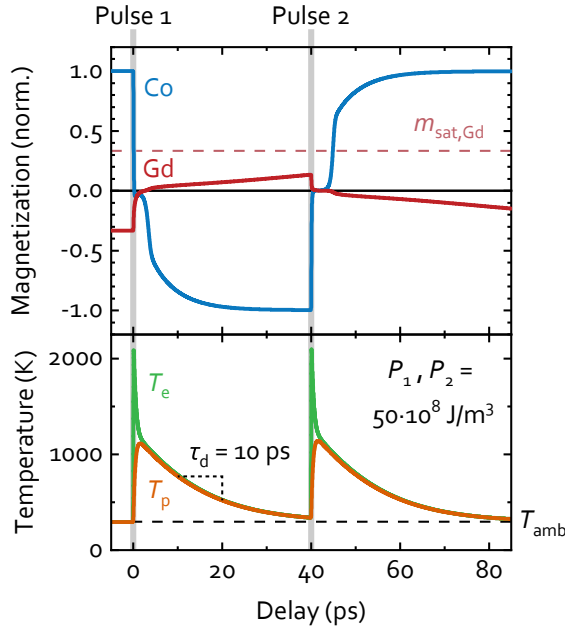
Figure 4.3: M3TM simulation results of excitation of a Co/Gd bilayer (3 monolayers each) with two laser pulses (gray lines) separated by 40 ps. The top graph shows the average magnetization response of both Co and Gd over time, with the dashed line indicating the Gd magnetization at saturation. The bottom graph shows the electron and phonon temperature of the combined system, with the ambient temperature T_{amb} (295 K) indicated by the dashed line.

Figure 4.3 shows the simulated magnetization dynamics (top) as well as T_e and T_p (bottom) of a layered Co/Gd system with $\tau_d = 10$ ps after excitation with two laser pulses separated by 40 ps. After the first pulse, the Co and Gd magnetization are switched, followed by remagnetization in the opposite direction. T_e increases rapidly due to heating by the laser pulse and equilibrates with T_p more slowly, while heat is being removed from the system with the characteristic timescale τ_d. As the intrinsic remagnetization rate of Co is faster than τ_d, the latter is dominant in determining the remagnetization time. By the time the second pulse arrives, the heat has nearly dissipated from the system, and the Co magnetization is very close to saturation. For Gd however, the remagnetization rate is an order of magnitude slower,[41,55,93] such that Gd has not returned to saturation (dashed line) when the second pulse arrives. This is in contrast with the expected behavior in alloys, where the Gd has more transition metal neighbors with which it can exchange angular momentum and therefore remagnetize more rapidly.

Nevertheless, this second pulse also leads to the switching of the magnetization of both layers, after which remagnetization towards the original direction proceeds. Although it might seem counter-intuitive that switching is still possible with a strongly reduced Gd moment, this is in line with previous research on AOS in synthetic ferrimagnets where a change in the relative magnetization of the sublattices was found not to hinder switching.[89] Conversely, in ferrimagnetic alloys it is known that AOS can only occur if the magnetizations of both sublattices (nearly) cancel each other.[88] As such, we conjecture that any possible detriment in remagnetization speed in synthetic ferrimagnets could be compensated by the absence of a need to wait for full magnetization recovery, leading to very similar timescales for repeated AOS. Moreover, as the heat diffusion is somewhat overestimated in this model, the Co magnetization will in reality still be partially quenched when the second pulse arrives. However, due to the much higher Curie temperature of Co compared to Gd, there should still be a major difference in the ratio between magnetic moments when compared to equilibrium. It should be noted that the exact minimum condition upon which a second switch is possible depends on a multitude of factors, and is not comprehensively understood at this time. We note that the magnetization dynamics modelled by the M3TM show a discrepancy around zero magnetization when compared to time-resolved measurements on the same system.[77] More specifically, a slowing down of the dynamics around zero net magnetization is observed only in modelling. This is likely to be a consequence of treating each layer as one single spin, as such behavior is not found in atomistic models.[16,19,129] This might lead to a shift in the minimum time between switches predicted by the model, but should not impede the deduction of qualitative behavior and trends from the M3TM.

Finally, we investigate the effect of heat diffusion on double switching in the M3TM. For different values of τ_d we model excitation with two laser pulses. By varying the time delay between the pulses and evaluating the final magnetization state, we extract a value for the minimum time delay needed for double switching as a function of τ_d. figure 4.4 shows these values for two different values of the absorbed laser energy density. We emphasize that our first order approximation of heat diffusion should not be used to draw quantitative conclusions. For $\tau_d > 5$ ps, the minimum waiting time between pulses depends approximately linearly on τ_d. In this regime heat diffusion seems to be the dominant factor, however a non-trivial dependence on the energy of both pulses is also found. Comparing the data for 40 and 50×10^8 J/m^3 (solid circles and open squares, respectively), it is found that the second switch can happen faster if the energy of both pulses is higher. Individual time traces for different pulse energies (not shown here) indicate that the switch occurs faster for higher pulse energies, giving more time for relaxation towards saturation. For $\tau_d < 5$ ps, the minimum time needed for the second
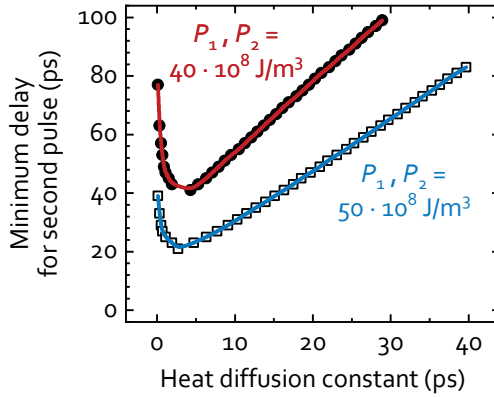
Figure 4.4: Minimum time delay needed between two pulses, with energy indicated in the figure, for consistent double switching. Calculated as a function of the heat diffusion constant τ_d with M3TM simulations.

pulse starts to increase, which is attributed to a hindrance of the switching mechanism in general by the unrealistically fast dissipation of heat. Here, the system already cools down enough for the sublattices to start remagnetizing at the timescale at which the switch would normally take place. From these results it is clear that although heat dissipation has a significant effect on the waiting times between subsequent switching events, the energy also needs to be carefully controlled. Combining this with the experimental observation that a slight increase in laser energy can already be detrimental, this highlights the narrow range of laser energies for which consistent as well as rapid double switching is possible. Finally, we note that double switching within 10 ps, as observed in figure 4.1b, is not reproduced in modelling even for very efficient heat dissipation. We believe this to be an intrinsic limit of the system modelled here, as this probably represents a minimum time needed for sufficient recovery of the Gd magnetization. It is possible, though not trivial, to extend the M3TM to include intermixing at the Co/Gd interface by treating each discrete layer as a Co_x/Gd_{1-x} alloy and varying the concentration x with the layer number.[133] Here it was found that intermixing leads to more efficient transfer of angular momentum between the two sublattices, driving a faster zero crossing of the magnetization. Hence we expect that in our sputter deposited system, which surely contains an intermixed interface region, both Co and Gd could remagnetize more rapidly than in a bilayer with perfect interfaces, potentially reducing the waiting time needed for the second switch. It should be noted that switching| back within a few picoseconds, as was reported using a different model,[129] does not seem to be possible using the M3TM for any combination of parameters.

In conclusion, we have investigated the timescales for repeated all-optical switching in synthetic ferrimagnetic Co/Gd bilayers, and have demonstrated a minimum waiting time of 10 ps between two subsequent switching events, implying writing speeds of up to 100 GHz. We have shown that the layered nature of these systems need not be a hindrance to achieve similar writing speeds as in alloys, explained by the notion that the slower remagnetization of Gd is compensated by a less critical dependence of AOS on the Gd moment. Furthermore, by changing the substrate we have confirmed the importance of engineering heat diffusion away from the magnetic system. Finally, with modelling efforts using the M3TM we have resolved the qualitative role of heat diffusion in ultrafast repeated switching, but we also stress that controlling the laser energy is critical to reliable integration in future optically written data storage devices.

4

5

SPIN-CURRENT GENERATION IN SYNTHETIC FERRIMAGNETS

The role of non-local spin transport in all-optical switching is thusfar scarcely understood. Using Co/Gd and Co/Tb bilayers we isolate the contribution of the rare-earth materials to the generated spin currents by using the precessional dynamics they excite in an adjacent ferromagnetic layer as a probe. By measuring THz standing spin-waves as well as GHz homogeneous precessional modes, we probe both the high- and low-frequency components of these spin currents. The low-frequency homogeneous mode indicates a significant contribution of Gd to the spin current, but not from Tb, consistent with the difficulty in achieving all-optical switching in Tb-containing systems. Measurements on the THz frequency spin waves reveal the inability of the rare-earth generated spin currents to excite dynamics at the sub-ps timescale. We present modelling efforts using the s-d model, which effectively reproduce our results and allow us to explain the behavior in terms of the temporal profile of the spin current.

5.1 Introduction

Over the past few decades, femtosecond (fs) laser excitation of magnetic materials has led to the discovery of a rich collection of physical phenomena. Among these, single fs laser pulse all-optical switching (AOS) of the magnetization in rare-earth transition-metal ferrimagnetic alloys[15,16] and multilayers[20,91] appears to be especially promising for future memory applications.[18] This phenomenon was shown to arise from the transfer of angular momentum between two magnetic sublattices.[19] In the same period the fs laser excitation of spin currents, mobile electrons carrying spin angular momentum, has been gaining significant interest from a fundamental perspective.[52,99]

    A particularly relevant use for these optically excited spin currents exploits their ability to transfer angular momentum between two ferromagnetic layers. This was first demonstrated in an experiment investigating the ultrafast laser induced magnetization dynamics of two ferromagnetic layers separated by a conductive spacer layer.[36] A diverse body of research into optically generated spin currents has since arisen.[52,104,108,136–139] In recent years it has been shown that novel device functionality can be achieved at the intersection of AOS and optically excited spin currents. These works focus on systems where an all-optically switchable ferrimagnetic layer is separated by a spacer layer from a ferromagnetic layer. Depending on the precise composition of the layers, either the spin current coming from the ferromagnet can influence the AOS process,[140] or the ferromagnet can be switched by the spin current coming from the switchable layer.[111–113] This last case demonstrates the strength of the spin current generated upon excitation of an all-optically switchable system, and begs the question to what extent this spin current plays a role in the switching mechanism.

    Although a great deal of AOS research has been performed on Gd(Fe)Co and Co/Gd systems, recent research indicates that Tb can be used as rare-earth (RE) component instead of Gd.[91,92] However, in these works AOS has been found only for very specific layer thicknesses, a requirement which is not present in layered ferrimagnets containing Gd.[89] Work by Choi et al. has shown that spin currents generation in Tb is significantly weaker than in Gd,[100] hinting at an explanation for the increased difficulty in attaining AOS. Here the accumulation of spins at the far end of a thick conductive spacer layer was measured, which can lead to a distorted spin current profile due to diffusive electron transport.[99] Moreover, the use of alloys makes it difficult to disentangle the spin current contributions originating from different elements.

    In this work, we systematically study spin current generation in synthetic ferrimagnets using the collective spin precession they excite in a neighboring layer as a probe.
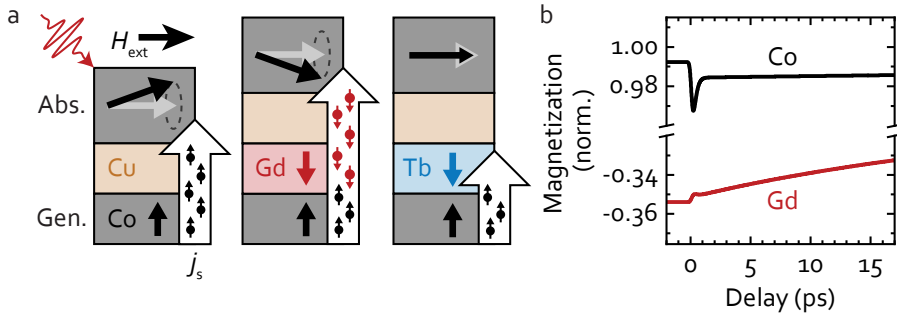
Figure 5.1: (a) Schematic overview of the experiments, where the effect of the generation layer composition on the response of the absorption layer is sketched for each of the three studied configurations (Co, Co/Gd and Co/Tb). (b) Example magnetization response calculated using the *s-d* model for Co and for Gd in a Co/Gd bilayer.

The basic experimental concept and the noncollinear magnetic bilayers used in this work are sketched in figure 5.1a. The generation layers are synthetic ferrimagnetic bilayers, consisting of Co which couples antiferromagnetically to either Gd or Tb. Although these latter materials are paramagnetic at room temperature in bulk, a ferromagnetic phase can be stabilized when interfaced with a ferromagnetic material,[141] which decays exponentially away from the interface. Upon laser excitation of the out-of-plane magnetized generation layer, a spin current which is spin-polarized in the direction of the local magnetization is excited and injected into a ferromagnetic absorption layer with in-plane magnetization. There the spins exert a torque on the local magnetic moments and excite both the homogeneous precessional mode[99,142] as well as higher-order inhomogeneous spin waves.[109,143] By extracting the phase, amplitude and frequency of the FMR mode and THz spin waves, we indirectly study the absorbed spin current,[110] which is commonly expected to scale with the time derivative of the magnetization (dm/dt), fulfilling conservation of angular momentum.[99,110] In this framework, these spin-wave parameters are directly proportional to the corresponding parameters of the Fourier component of the spin-torque pulse at the spin-wave frequency. Specifically, we probe the phase of the precessional dynamics to investigate the temporal profile of the spin current, and the amplitude to study the spin-current strength and attenuation. Changing the thickness of the RE layer changes both spin-current properties, which leads to significant variations in the measured parameters of the precessions. By measuring both the homogeneous FMR mode (~ 10 GHz) and the first-order inhomogeneous mode (~ 0.5 THz), the spin current can be studied on two distinct timescales, giving access to both the fast as well as the slow components of the spin current separately.

We corroborate our experiments with an *s-d* model which treats local and non-local spin dynamics in a joint description.[84,101,144,145]

Our results on the FMR mode show a strong contribution to the excited spin current from Gd, which is in line with previous work[100,111] and confirmed by our modelling efforts. In contrast, the THz mode cannot be efficiently excited by Gd, hinting at the relatively slow nature of the spin current contribution from Gd. In the Co/Tb system, both the FMR and THz modes are found to vanish with only a slight addition of Tb, indicating weak spin current generation in Tb but strong spin absorption, consistent with the high spin-orbit coupling (SOC) in this material. These results shed new light on non-local spin dynamics in highly technologically relevant synthetic ferrimagnets, and help elucidate the role of these processes in all-optical magnetic data recording.

5.2   EXPERIMENTAL DETAILS

The noncollinear magnetic bilayer central to this work, as sketched in figure 5.1a, consists of an out-of-plane magnetized Co/RE generation layer (where RE is either Gd or Tb) and an in-plane magnetized Co absorption layer. Spin transport between the two magnetic layers is facilitated by a thin Cu spacer layer, which also serves to magnetically decouple the layers. The samples are fabricated using DC magnetron sputtering, where we vary the RE layer thickness along the sample length to ensure consistency between measurements. The full sample stack is given by Si:B(substrate)/Ta(4)/Pt(4)/Co(1)/RE(X)/Cu(2.5)/Co(5)/Pt(2.5) (numbers in brackets indicate the thickness in nm, with X being the variable RE thickness).

We employ pump-probe spectroscopy to measure the magnetization dynamics upon laser-pulse excitation, using the magneto-optical Kerr effect (MOKE) in the polar configuration to probe the magnetization. The sample is placed in a magnetic field with a variable angle of up to 20° with the sample plane. A mode-locked Ti:Sapphire laser is used to generate pulses at a repetition rate of 80 MHz and with a wavelength of 780 nm. The pulse length at sample position is approximately 150 fs. Both pump and probe pulses are focused onto the sample with a spot size of approximately 16 and 8 μm^2 respectively, and the pump fluence is about 1 mJ/cm². We use *Complex MOKE* to separate the magnetic contrast of both magnetic layers.[103] To accurately determine the absolute spin-wave phase in our experiments, the so-called coherence peak is used, which arises at temporal and spatial pump-probe overlap due to interference effects.[146] For more details on the experimental setup, see appendix B.1.
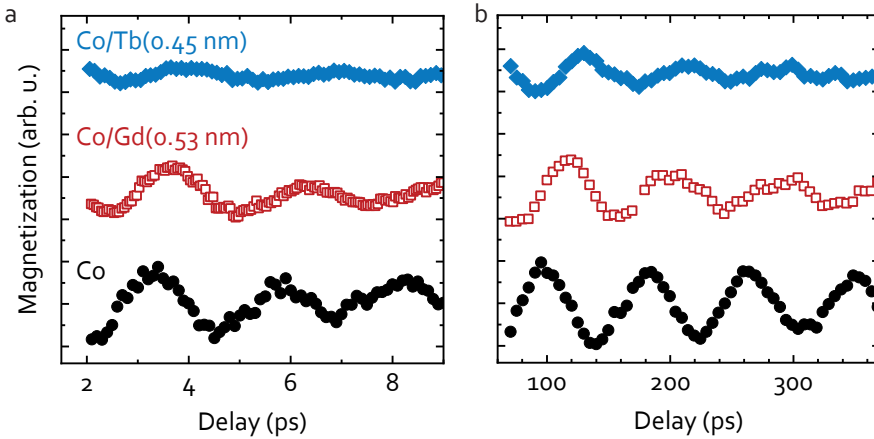
Figure 5.2: Response of the absorption layer for each studied configuration. Both (a) the first order inhomogeneous mode (H_{ext} = 0 mT) and (b) the homogeneous (H_{ext} = 100 mT) mode are plotted, where only the former is measured using *complex MOKE*.

5.3 EXPERIMENTAL RESULTS

As a first experiment, we investigate the general behavior of the precessional dynamics for the three different generation layer configurations (figure 5.1a). In order to isolate the contribution of the RE layers, in which the magnetization decays exponentially away from the Co interface, their thicknesses need to be chosen carefully. Previous work gives a typical lengthscale of the magnetization decay in Gd of 0.45 nm,[20] with a similar value to be expected for Tb. In figures 5.2a and 5.2b we present typical measurements of the THz spin-wave and FMR mode respectively for the three different generation layer configurations, namely Co(1), Co(1)/Gd(0.53), and Co(1)/Tb(0.45). Our results show that the composition of the generation layer significantly influences the spin-wave behavior, specifically the amplitude and phase. To better understand this observation, we show representative modelled traces (see appendix B.5) of the magnetization response of Co and Gd upon fs laser excitation, in figure 5.1b. The precessional behavior can then generally be understood with a simple picture where the generated spin current is assumed to be proportional to dm/dt.[99,110] Considering the antiferromagnetic coupling between Co and Gd (or Tb), the spin currents generated by the RE material and by Co should also have the opposite sign. Therefore, we expect that the polarization of the total spin current changes sign (figure 5.1a) when the RE material becomes the dominant contributor, which could explain the experimental observation of the large
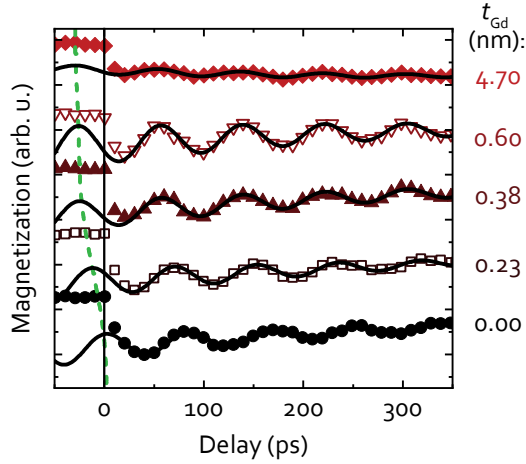
Figure 5.3: Measured FMR mode (H_{ext} = 100 mT) for several Gd thicknesses, fitted with a damped cosine function. The green dashed line indicates the FMR phase shift and the thickness calibration is discussed in appendix B.1.

phase shift of the FMR mode. However, no such sign change is observed in the THz measurements, hinting at a less significant contribution of the RE material to the sub-ps spin current dynamics. This is consistent with the expected magnetization dynamics plotted in figure 5.1b, which for Gd take place on the timescale of multiple ps, leading to a relatively slow spin current profile. Additionally, we find a strongly reduced amplitude for precession excited with a Co/Tb generation layer. This can be attributed to strong absorption of the spin current generated in Co, consistent with the large SOC in Tb,[93] as well as weak spin current generation in Tb.

5.3.1   FMR MODE

To get a better understanding of the observed behavior, we systematically measure both the FMR and THz mode as a function of the Gd and Tb thickness in the generation layer. First we discuss the results on the FMR mode, of which we show a selection of measurements for a Co(1)/Gd(X) generation layer in figure 5.3. To extract the phase and amplitude of the FMR mode, these measurements are fitted with a damped cosine function, indicated by the solid black lines, where the frequency is shared between all datasets.
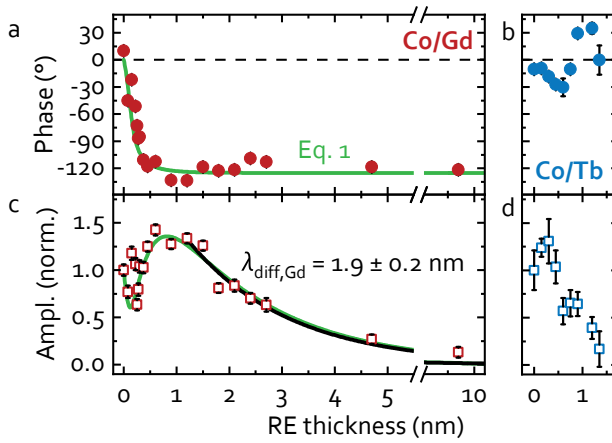
Figure 5.4: (a,b) FMR phase as a function of Gd (a) and Tb (b) thickness. (c,d) FMR amplitude as a function of Gd (c) and Tb (d) thickness, normalized to the amplitude without RE layer for both datasets. The green solid line in (a) and (c) represents the modeled behavior using equation (5.1), and the black solid line in (c) is a fit with an exponential function.

We first discuss the FMR mode phase, of which we already observe a shift as a function of Gd thickness in figure 5.3, as indicated by the dotted green line connecting the shifted maxima of the fits. The phase we extract from the fits is plotted in figures 5.4a and 5.4b for Co/Gd and Co/Tb respectively. With the addition of only 1 nm of Gd, a phase shift of more than 130° is observed, whereas no consistent phase shift is measured when adding Tb. This again indicates a strong contribution to the spin current from Gd, but a small to non-existent contribution from Tb. For large thicknesses of Gd the phase remains constant, which can be explained by the paramagnetic state further away from the Co/Gd interface.

Next, we focus on the amplitude of the FMR mode as a function of RE thickness, which is normalized to the amplitude for a pure Co generation layer and plotted in figures 5.4c and 5.4d for Co/Gd and Co/Tb respectively. This amplitude has been corrected for changes in light absorption using transfer matrix calculations,[147] as described in appendix B.2. For Gd, an initial dip and succesive rise of the amplitude is observed, followed by a gradual decrease. This behavior, in combination with the observed change of the FMR phase can be captured in a simple toy model where we assume the spin current contributions from Co and Gd excite two spin waves with different amplitudes and phases, but with the same frequency. As discussed previously, the Gd is magnetized due to exchange coupling with the Co, decaying at a characteristic length scale λ_{mag}

which determines its contribution to the total spin current. Furthermore, the addition of Gd introduces a characteristic length scale λ_{diff} over which spin information is lost due to spin flip scattering events, known as the spin diffusion length. For now we assume that spin diffusion is independent of the magnetic state of Gd. Writing the phase difference δ between the two excited precessions using Euler's formula, the FMR mode can then be described as

$$A_{FMR}\, e^{i\varphi} = \left[A_{Co} - A_{Gd}\, e^{i\delta} \left(1 - e^{-\frac{t_{Gd}}{\lambda_{mag}}} \right) \right] e^{-\frac{t_{Gd}}{\lambda_{diff}}} , \qquad (5.1)$$

where A_{Co} and A_{Gd} are the dimensionless amplitudes of the precessions excited by the magnetic volume of Co and Gd respectively. These then result in a combined precession with amplitude A_{FMR} and phase φ. Expressions for these two parameters can be derived, as is shown in appendix B.3. Now $A_{Co} = 1$ can be fixed by normalization, and $A_{Gd} = 3.2$ and $\delta = -140°$ are chosen to match the maximum of the amplitude and saturation of the phase, respectively. Within these constraints, valid values for the remaining parameters are found by manual adjustment, and are found to be $\lambda_{mag} = 0.4 \pm 0.1$ nm and $\lambda_{diff} = 2.0 \pm 0.2$ nm. The amplitude of the Gd-excited precession A_{Gd}, when corrected for the expected equivalent magnetic thickness of Gd (0.45 nm), gives a Gd contribution that is approximately 7 times larger per nm than that of Co. A complete understanding of this difference is outside of the scope of this work, but some factors of relevance are the differences in magnetization, the amount of magnetic moment lost during demagnetization, and the spin-wave excitation efficiency, which will be discussed later. The value for λ_{mag} closely matches the experimentally determined length scale for the loss of magnetization in Gd of ~ 0.45 nm.[20] We note that this length scale could also affect the rate of spin flip scattering, such that the parameter λ_{diff} might not provide a full description. Fitting the data for the FMR amplitude for thicknesses where Gd is expected to be paramagnetic (from 1.5 nm onwards) with an exponential function, indicated by the solid black line in figure 5.4c results in a $\lambda_{diff,Gd}$ of 1.9 ± 0.2 nm, which has not been measured before to the best of our knowledge. The close agreement between the two descriptions indicates that the magnetic state is not very relevant for spin flip scattering in these weakly magnetic systems.

The reasonable agreement between experiments and calculations indicate that the most important elements of this complex system are captured by this simple model. However, the model can not capture the behavior we observe for a Co/Tb generation layer, as plotted in figures 5.4b and 5.4d. Here we instead find only a rapid decrease of the amplitude with the addition of Tb. This could indicate a very short diffusion length λ_{diff} for Tb, which precludes any statements about the spin-current generation
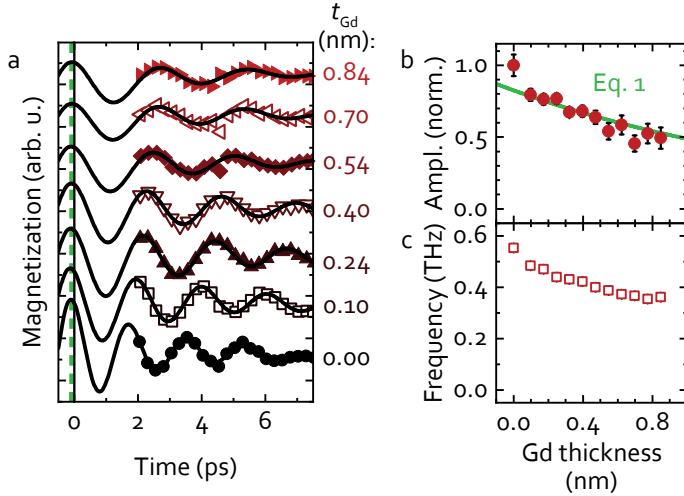
Figure 5.5: (a) Measured THz mode for several Gd thicknesses, fitted with a damped cosine function. The green dashed line indicates the spin-wave phase shift. (b) Spin-wave amplitude, green line indicates a solution of equation (5.1) using A_{Gd} = 0 and $\lambda_{diff,Gd}$ = 1.9 nm and (c) frequency as a function of Gd thickness.

strength in Tb. We attribute this discrepancy to a larger degree of scattering of the mobile electrons in Tb due to the high SOC compared to Gd,[93] leading to a loss of the spin information over shorter length scales.

5.3.2 THz mode

We measure the THz spin-waves as a function of RE thickness to investigate the spin-current generation on the ps timescale, and show a selection of the measurements for a Co/Gd injection layer in figure 5.5a. Because THz mode excitation takes place on the same timescale as laser-induced demagnetization and spin-current generation, we disregard the first 2 ps of the data, in accordance with ref. 110. We again used a damped cosine function to fit the data, indicated by the solid black lines, in order to extract the spin-wave amplitude, phase, and frequency. At around 1 nm, the signal-to-noise ratio is too low to extract spin-wave parameters reliably. The amplitude of the spin waves, which is plotted in figure 5.5b, drops significantly with Gd thickness. Contrary to the behavior for the FMR mode, no initial rise of the amplitude due to a Gd contribution is observed. We therefore show the expression for the amplitude derived from equation (5.1) using A_{Gd} = 0 and $\lambda_{diff,Gd}$ = 1.9 nm as the solid green line in the figure,

which is equivalent to an exponential decay describing only the spin diffusion due to Gd. The good agreement indicates that Gd is not actively contributing to the excitation of the THz mode, which shows that this mode is excited by the Co-dominated fast component of the generated spin current.[55] This is further confirmed by the observation that the spin-wave phase is independent of the Gd thickness, as indicated by the green dashed line in figure 5.5a. The same measurements are repeated for Tb and presented in appendix B.4. No significant difference between the THz spin-wave frequency and phase for the two materials is observed, again confirming the dominant role of Co in exciting these spin waves. However, a full analysis of the data is complicated by a more rapid decrease of the spin-wave amplitude with increasing Tb thickness, which could again be attributed to high spin-flip scattering due to SOC.

Contrary to our measurements of the FMR mode we observe a significant decrease of the THz spin-wave frequency for increasing Gd thickness, plotted in figure 5.5c, which is not predicted by our simulations (see appendix B.6). We believe there are several mechanisms that could explain this observation, the foremost being a growth related change of the exchange stiffness[109,148] and coupling between spin waves in the generation and absorption layers. The mechanisms are discussed in detail in appendix B.7 and predict the same direction of the shift of the THz spin-wave frequency. However, a full understanding of this effect is beyond the scope of this work and requires further research.

5.4   S-D MODELLING

To better understand the mechanisms governing our observations, as well as the underlying physics in general, we modeled the generated spin current in the synthetic ferrimagnetic generation layer using an extension of the s-d model.[53,84,99,101,144,145,149] This model describes the coupling of local spins, in this case the $3d$ and $4f$ electrons in the RE-TM ferrimagnet, to a system of itinerant spins (s electrons). The latter system includes diffusive spin transport, similar to refs. 99, 101, 145. To model the experiments, we define a discretized material system consisting of a ferrimagnetic (Co/Gd) region and a nonmagnetic spacer layer (Cu). The Co/Gd bilayer is modeled in a layered manner, where the local Co and Gd concentration is sampled from a function that represents an intermixed transition from pure Co to Gd, similar to ref. 133. This process is discussed in appendix B.5. Furthermore, the absorption layer is implemented as an ideal spin sink connected to the spacer layer, which is a valid assumption considering the experimental absorption layer thickness of 5 nm and the transverse spin diffusion length in Co of
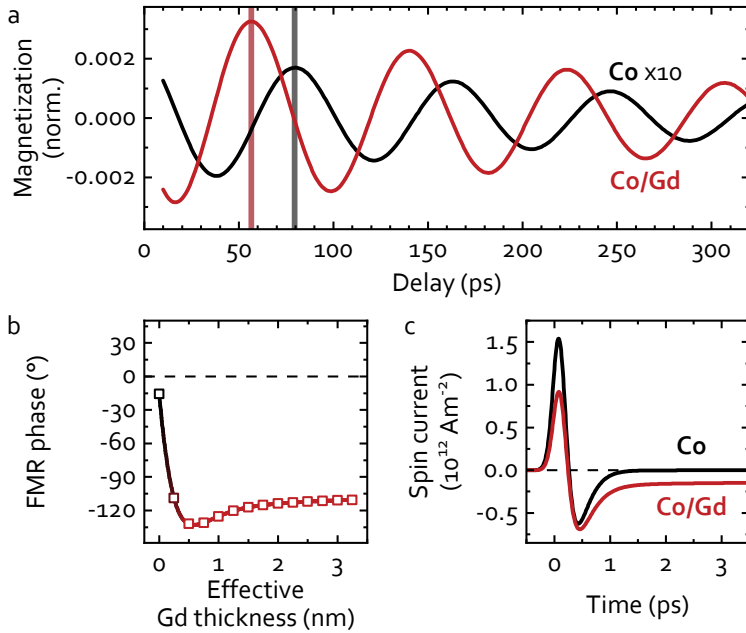
Figure 5.6: (a) Calculated FMR mode excited by the spin current from a Co(1) (black) and Co(1)/Gd(2) (red) generation layer. (b) Absolute phase of the excited FMR mode as a function of the effective thickness $t_{eff,Gd}$ of the (generation) Gd layer. (c) Absorbed spin current as function of time generated by a Co (black) and a Co/Gd (red) generation layer.

approximately 1 nm.[109] This allows us to calculate the absorbed spin current for varying composition of the Co/Gd layer. Using a linearized Landau-Lifshitz-Gilbert equation, including the anti-damping spin-transfer torque exerted by the absorbed spin current, we calculate the absolute phase shift of the excited homogeneous precession. Although the used model includes multiple assumptions that disqualify any precise quantitative statements, it gives a complete description of the qualitative characteristics of the spin current and excited precession. Further details on the modeling, including all the used material parameters, are presented in appendix B.5.

In figure 5.6a we present traces of the modeled z-component of the FMR mode excited by a Co(1) and a Co(1)/Gd(2) generation layer, in black and red, respectively. Note that the amplitude of the FMR mode excited by pure Co has been multiplied by 10 for clarity, as it is significantly weaker than that excited by Co/Gd. This is likely a result of the assumptions made in the model, such as the simplistic description of optical absorption and the parameters chosen for Gd, as the exact shape of the spin current

pulse strongly affects the excitation efficiency. Similar to the experimental results, our model shows a shift of the phase of the FMR mode when Gd is added to the generation layer. In figure 5.6b the absolute phase is plotted as a function of the effective Gd thickness $t_{\text{eff,Gd}}$, which for our purposes is analogous to the Gd layer thickness, and is further described in appendix B.5. The figure clearly shows a qualitative agreement with the experiments (figure 5.4c), with a shift of approximately 130° upon adding a few monolayers of Gd. The exact value of the phase shift can be explained by a combination of factors. Naively, one would expect a 180° phase shift if only the Gd spin-current would excite dynamics once it starts to dominate the total spin current. The actual shift however is lowered by the contribution of Co, as well as the relatively slow (Type II) magnetization dynamics of the Gd,[55] as will be demonstrated in the following.

To clarify the origin of the observed phase shift, we plot the absorbed spin currents for a pure Co(1) injection layer and a Co(1)/Gd(2) bilayer calculated using the *s-d* model in figure 5.6c. The addition of Gd leads to changes in both the amplitude of the first, fast peak of the spin current, as well as a much longer negative tail. Both of these can be understood by the demagnetization behavior of Gd, as plotted in figure 5.1b. The reduction of the amplitude of the first peak of the spin current is caused by the initial, relatively rapid demagnetization of Gd. At longer timescales, when the Co generated spin current is negligible, a long tail in the Co/Gd generated spin current is observed. This is in turn caused by the secondary, slower demagnetization of Gd, and results in a spin current that is mostly polarized in the opposite direction. This explains the abrupt phase jump in figure 5.4c and 5.6b for increasing Gd thickness. Moreover, the long duration of this component of the spin current gives rise to a deviation of the phase shift from 180°. This is to be expected, as the Gd demagnetization takes place over tens of ps, which is comparable to the precessional period (~ 80 ps). The small increase of the phase from -130° to -110° that is observed in figure 5.6b for a further increase of the Gd thickness is attributed to an additional slowing down of the Gd magnetization dynamics. More specifically, we find that transfer of angular momentum from the Co, which speeds up the Gd magnetization dynamics near the interface between Co and Gd, has a smaller total effect when the Gd thickness is increased.

In appendix B.6 we show calculated traces of the THz mode for increasing Gd thickness. Our calculations indicate a phase shift of up to 10° when adding a 2 nm thick Gd layer to a 1 nm thick Co layer. Contrary to previous work[110] we were unable to resolve this potential phase shift, because the resolution is determined by the strength of the spin current and thus the total magnetic moment of the generation layer. In future research, Co/Gd multilayers could be used to study THz spin-wave generation in rare-earth transition-metal ferrimagnetic system in more detail.

5.5 Conclusion

We have shown that examining the parameters of precessional modes excited by ultra-fast optically generated spin currents can be a powerful tool to elucidate the behavior of these spin currents. Synthetic ferrimagnets offer a novel platform to systematically investigate these phenomena. The large discrepancy in spin current generation between Gd and Tb could shed new light on the relative difficulty of achieving AOS in systems containing only the latter as RE material. Using spin-wave modes with THz frequencies has additionally allowed us to probe the high-frequency component of the generated spin currents. Here we again find a link between the intrinsic speed of the magnetization dynamics and the behavior of the excited spin current. This gives additional weight to the notion that angular momentum which is lost during demagnetization can be transferred to mobile spins.[99] This notion also underlies the *s-d* model, which we have successfully used to describe our experimental results. Our experiments give new insight in the magnetization dynamics of rare-earth materials, which could prove critical in future spintronic memory devices.

5

6

SPIN-CURRENT ASSISTED
ALL-OPTICAL SWITCHING

Although all-optical switching has shown potential for future data storage and logic de-vices, the toggle mechanism is not desirable for applications. Here we experimentally demonstrate conversion from toggle switching to a deterministic mechanism by biasing AOS in a Co/Gd bilayer with a spin polarized current which is optically generated in an adjacent ferromagnetic reference layer. We show deterministic writing of an 'up' and 'down' state using a sequence of 1 or 2 pulses, respectively, and demonstrate the non-local origin by varying the magnitude of the generated spin current. Our demonstration of determinis-tic magnetization writing could provide an essential step towards the implementation of future optically addressable spintronic memory devices.

6.1   Introduction

The explosive growth of data production and consumption rates in the past decades has driven the search for faster and more energy-efficient methods to record data. Among these methods, the use of optics to assist or even facilitate data recording in magnetic materials shows promise in terms of speed and energy efficiency.[18] More specifically, all-optical switching (AOS) of magnetic materials, whereby the magnetization can be reversed on a picosecond timescale using only femtosecond (fs) laser pulses, has striking potential. First discovered around a decade ago,[15] it has since been shown that two mechanisms can be distinguished, namely, (1) multiple pulse helicity dependent switching and (2) single pulse helicity independent switching. The helicity dependent mechanism has been observed in several magnetic materials,[15,150–155] and is believed to result from a dependence of the absorption of circularly polarized light on the magnetization direction.[156] Although this mechanism is deterministic in that the final magnetization direction is defined by the helicity of the incident light alone, it requires multiple laser pulses,[154] which limits speed and applicability. The second effect, single pulse helicity independent switching, has thus far been demonstrated in ferrimagnetic GdFeCo alloys,[16,17,19] synthetic ferrimagnetic Co/Gd bilayers[20] and very recently in a ferrimagnetic Heusler alloy.[157] This effect relies strongly on transfer of angular momentum between magnetic sublattices, as well as a difference in demagnetization timescales between the involved materials.

In the example of a ferrimagnetic rare earth-transition metal (GdFeCo) alloy, single pulse switching has been shown to be a toggle process.[19] In the ground state of these materials, the sublattices (Gd and FeCo) are aligned antiparallel due to an antiferromagnetic coupling. Upon fs laser pulse induced heating both sublattices will demagnetize, but FeCo will do so more rapidly than Gd. This means that at some point the FeCo magnetization will be nearly quenched whilst there is still a significant amount of Gd magnetization. Due to transfer of angular momentum between the sublattices the FeCo magnetization is pulled through zero, creating a temporary ferromagnetic state. While the FeCo sublattice now remagnetizes in the opposite direction, Gd continues to demagnetize, and is also pulled through zero due to the antiferromagnetic coupling between the sublattices. After relaxation both sublattice magnetizations end up opposite to the initial state. It should be noted that single pulse helicity dependent switching has also been observed in a narrow range of laser fluences for GdFeCo alloys,[15,158] owing to magnetization and helicity dependent light absorption.[75] This same switching process has also been demonstrated in synthetic ferrimagnetic Co/Gd bilayers,[20] which we will

6

use in this chapter. Switching in the latter materials has been shown to be more robust than in ferrimagnetic alloys, in the sense that it does not depend on the sublattices being close to magnetization compensation.[89]

Using a toggle mechanism for data storage applications would require prior knowledge of the state of a bit to overwrite it, imposing limits on speed and integration flexibility. Therefore it is desirable to find a deterministic AOS procedure using as few laser pulses as possible where the final magnetization direction is not always the opposite of the initial state but instead relies on a specific process to set and reset a magnetic bit. In this chapter, we will propose and experimentally demonstrate such a method.

Regarding the underlying physics, the single pulse AOS scenario described earlier has been confirmed by several complementary theoretical models.[16,79–82,85] These works have all included the exchange of angular momentum between the two sublattices as an essential ingredient to find switching. However, it is not yet clear to which extent this exchange is driven by local exchange scattering processes, or by non-local transfer of angular momentum. Recent work has shown that upon switching, angular momentum can be transferred from a switching layer to a ferromagnetic layer separated by a conducting spacer, thereby switching the ferromagnetic layer.[111] The inverse effect where angular momentum is transferred non-locally from a ferromagnetic reference layer to a switching layer has however not been addressed so far.

In this chapter, we experimentally demonstrate deterministic magnetization writing using either one or two laser pulses in a system consisting of a ferromagnetic *reference layer*, a conductive spacer layer, and an all-optically switchable *free layer*. When exciting the sample with a fs laser pulse, a spin polarized electron current will be generated in the ferromagnetic reference layer, governed by its magnetization.[98,99] Angular momentum carried by this spin current is transferred to the free layer, where it can assist or hinder switching depending on the relative magnetization orientation of the reference and free layer. This asymmetry between the parallel and antiparallel alignment of these layers leads to two incident laser fluence regimes. Above a certain threshold fluence, the final state is completely determined by the orientation of the reference layer. When increasing the fluence above a higher threshold, the familiar toggle switching mechanism is recovered. We demonstrate experimentally how these two regimes combined can be used to deterministically write both magnetization states of the free layer, regardless of its initial state. Moreover, we confirm that this effect scales as expected with the optically generated spin current, and demonstrate that its magnitude can be easily tuned.
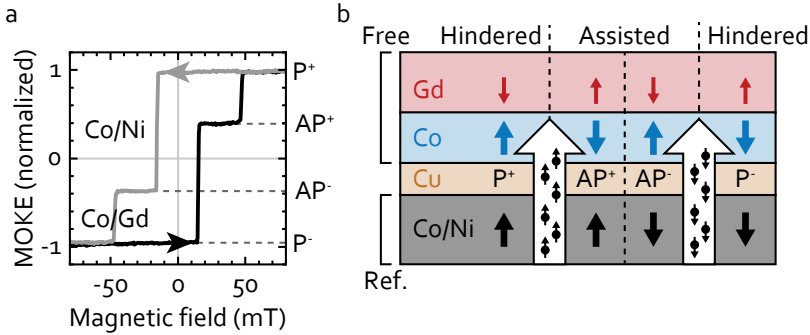
Figure 6.1: (a) Out-of-plane hysteresis loop of the $(Co/Ni)_{x4}$/Co/Cu/Co/Gd sample used in this chapter. The Co/Ni multilayer and Co/Gd bilayer switch independently at different applied magnetic fields, resulting in four possible magnetization states. (b) Simplified sketch of the multilayer stack used and how it breaks the toggle switching symmetry. The spin current generated in the reference layer upon demagnetization flows through the Cu spacer and aids or hinders switching in the free layer depending on the relative magnetization orientation of these layers.

6.2 DETERMINISTIC OPTICAL MAGNETIZATION WRITING

Our system consists of two magnetic layers, the previously mentioned reference and free layers. First is a ferromagnetic $[Co(0.2 \text{ nm})/Ni(x)]_{x4}$/Co(0.2) multilayer, which acts as the reference layer. This layer has an out-of-plane magnetization due to strong perpendicular magnetic anisotropy (PMA) and a relatively large magnetic moment compared to the switching free layer. The free layer is composed of a synthetic ferrimagnetic Co/Gd bilayer (1 and 3 nm respectively) with PMA, which is known to exhibit toggle AOS.[20] It should be noted that due to the antiferromagnetic exchange between Co and Gd,[131] the proximity induced Gd magnetization (corresponding to ~0.5 nm at room temperature) is aligned antiparallel with the adjacent Co in the ground state. When discussing the state of the free layer, we will refer to the dominant compound, i.e. Co. The reference layer and free layer are separated by a 5 nm Cu spacer layer, which decouples the layers magnetically whilst being transparent for spin-polarized electrons.[159] The stack is deposited using DC magnetron sputtering on a Si/SiO_2 substrate. The general sample structure for all measurements is Ta(4)/Pt(4)/[Co(0.2)/Ni(t_{Ni})]$_{x4}$/Co(0.2)/Cu(5)/Pt(0.5)/Co(1)/Gd(3)/Ta(4), where the numbers between parentheses indicate layer thicknesses in nm.

All four magnetization states of the system (Co/Ni up/down and Co parallel/antiparallel) can be realized using an external magnetic field. This is illustrated in figure 6.1a

using the out-of-plane hysteresis loop of the sample measured using the polar magneto-optical Kerr effect. Positive (+) and negative (−) states are defined as the reference layer having magnetization pointed up or down respectively, while parallel (P) and antiparallel (AP) refers to the relative orientation of the reference layer and Co in the free layer. The four states are thus defined as P^+, AP^+, AP^- and P^-. Note that since corresponding + and − states are simply time reversed versions of each other, they do not add any new physics. Therefore without loss of generality we only consider the positive (+) P and AP states, and drop the plus sign in the remainder of this chapter. Data on the corresponding negative states are shown in appendix C.1.

In our system both states of the free layer are no longer equivalent, due to a symmetry breaking provided by the reference layer. The nature of this symmetry breaking is sketched in figure 6.1b. Upon fs laser excitation, the ferromagnetic reference layer will demagnetize on a sub-picosecond timescale. The lost angular momentum is partially converted into a spin current, mediated by mobile electrons. Although multiple mechanisms for the generation of this spin current have been proposed, all find that the spin carried by the mobile electrons is aligned with the layer from which they originate,[98,99,160] i.e. the reference layer. The resulting spin current flows through the conducting Cu spacer layer to the free layer, where the spin angular momentum is deposited via scattering between mobile and localized electrons. Such non-local transfer of spin angular momentum can have a measurable impact on the ultra-fast magnetization dynamics of a magnetic layer.[36,109,136] Moreover, the spin current is expected to exist roughly on the timescale of the demagnetization of the reference layer, thereby transferring angular momentum to the free layer while Co and Gd are still demagnetizing. Because at this point the free layer is out of equilibrium with a strongly reduced magnetic moment, the additional angular momentum could significantly influence the switching process. We note that a spin current is also generated in the free layer, travelling towards the reference layer. However, as this particular spin current is much weaker due to the reduced magnetic moment of the free layer and is not found to significantly influence the receiving reference layer, we have not sketched it here. Moreover, it is precisely the threshold nature of AOS that allows us to observe the effect of a spin current much more clearly than in the reference layer, which is only partially demagnetized.

When the reference layer magnetization, and thereby the spin current polarization, is antiparallel to the Co magnetization in the free layer, the additional angular momentum should assist the demagnetization of Co and hinder the demagnetization of Gd. As switching is strongly dependent on the formation of a temporary ferromagnetic state aligned with Gd,[19] and this state can now form more easily, switching is assisted.
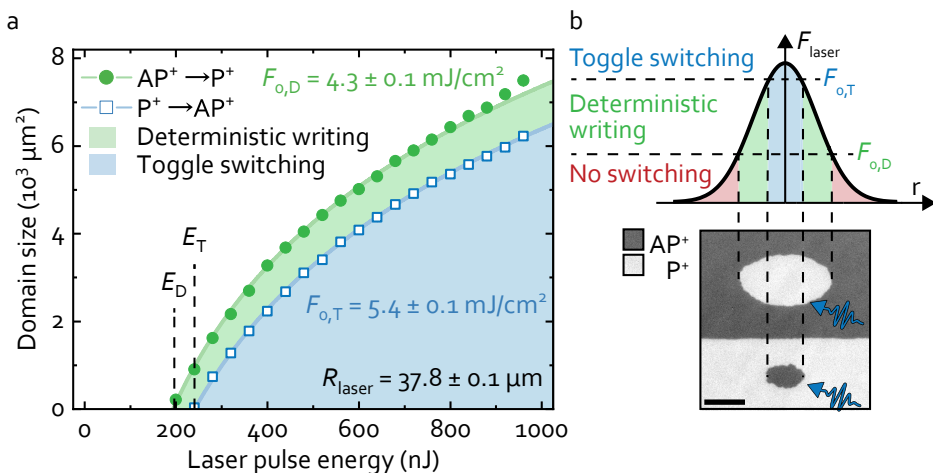
6

Figure 6.2: (c) Measurement of optically switched domain size as a function of incoming laser pulse energy for a sample prepared in either AP^+ or P^+ state. Fitting is done assuming a Gaussian laser spot profile to extract the threshold laser fluence F_o. (d) Top: Sketch of the threshold fluences $F_{o,D}$ and $F_{o,T}$ relative to the Gaussian laser spot profile. Bottom: Kerr microscopy images of switched domains after excitation by a single laser pulse of two regions with different initial magnetization. Scale bar represents 20 µm

In the case where the reference layer and free layer are aligned parallel the angular momentum transfer works in the opposite fashion, such that the formation of the ferromagnetic state, and therefore switching itself, is hindered. This results in a breaking of the symmetry of toggle switching, and could provide a regime where switching only occurs from an antiparallel to a parallel state, and not vice versa. In passing we note that due to the relatively high total magnetic moment of the reference layer in our samples compared to previous work,[111] we do not expect it to be significantly influenced by any spin current originating from the free layer. Moreover, in our stack the volume of magnetized Gd, which was conjectured to govern this 'reverse' spin current, is relatively small, yielding a small spin current in any case. After a few picoseconds, the reference layer should therefore start to remagnetize to its original saturation magnetization, ensuring that it remains fixed.

To experimentally confirm the expected behaviour of our system, we investigate the switching behaviour after excitation by single laser pulses with a duration of ~100 fs in a sample which is prepared in either the P or AP state. In figure 6.2a we present the results of these measurements, where we determine the threshold laser fluence F_o needed for switching by extracting the size of a switched domain as a function of

incident laser pulse energy(see 20). We find that the threshold fluences for switching are indeed not the same for both states. The fluence needed to switch from the AP state ($F_{0,D}$) is 1 mJ/cm² lower than the fluence needed to switch from the P state ($F_{0,T}$). Similar data for all four possible states are shown in appendix C.1.

The difference in switching fluence is in accordance with the expectation that the spin current generated in the reference layer either assists or hinders switching from the AP or P state, respectively. As a consequence, a regime of laser fluences (indicated by the green region between the fits in figure 6.2a) now exists where part of an excited region will only switch from an AP state to the corresponding P state, and never back with the same fluence. In other words, in this regime the magnetization is deterministically written to the P state. For higher fluences, indicated as the blue region in figure 6.2a, switching back from a P state is possible and toggle switching is recovered. Note that the laser spot radius is kept constant for both measurements, so the asymmetry between the states can also directly be seen in the different threshold energy for deterministic writing (E_D) and toggle switching (E_T).

By making use of both this difference in threshold fluence and the Gaussian spatial energy density profile of the laser pulse, we can demonstrate both deterministic writing and toggle switching in a single experiment, as shown in figure 6.2b. As sketched in the top part of this figure, both mechanisms should be present across a single laser pulse with high enough maximum fluence, assuming the switching is governed by local energy dissipation. In the bottom part of figure 6.2b we present microscope images with magnetization contrast (Kerr microscopy, see section 3.1.4 and appendix C.4) of a sample where both an AP and a P region are excited by a laser pulse with a such a high maximum fluence. Here it can now be directly seen that the size of the domain written by a single laser pulse indeed depends on the initial magnetization state, as seen previously in figure 6.2a. This is contrary to the 'standard' toggle AOS behaviour, where there is no such symmetry breaking for the energy needed to induce a switch. The demonstration of deterministic magnetization writing can be seen in the Kerr images by the larger area which is switched only when the magnetization starts in the AP state. This outer region does not switch when starting from the P state due to hindering by the spin current, which is aligned with the free layer in that case. Note that for lower total laser pulse energies, no switching will occur from the P state and an entire domain will be written deterministically, as we will demonstrate in the following.

As a full demonstration of the ability to deterministically write both states of the free layer, we present a scheme taking advantage of the switching behaviour in these samples in figure 6.3a. Two well-defined procedures can be used to write the desired
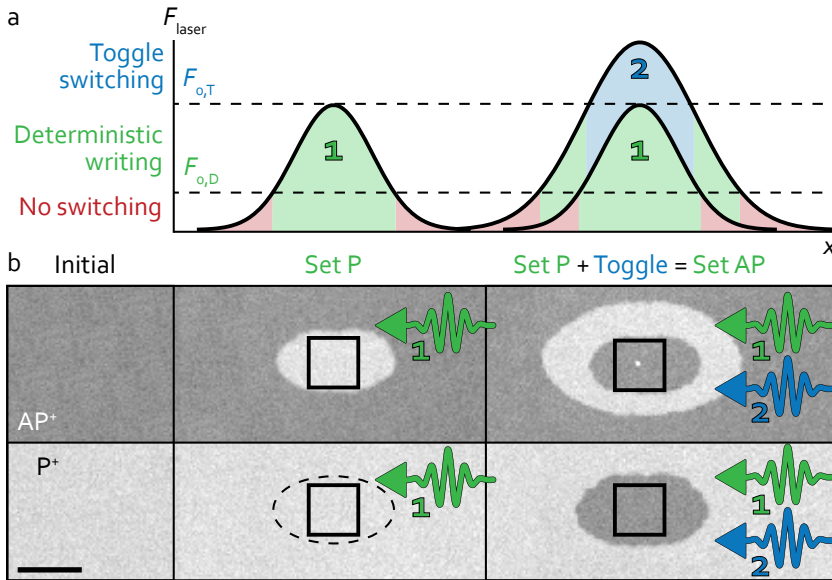
6

Figure 6.3: (a) Sketch of the scheme used to set the free layer magnetization parallel to the reference layer with one fs laser pulse (left) or antiparallel with two pulses (right). (b) Kerr microscopy images showing the deterministic writing of both a P and AP state (black squares) regardless of the initial state of the switching layer. Scale bar represents 20 μm

state of the free layer relative to the reference layer (P or AP). By using a single laser pulse with maximum fluence above the threshold fluence for deterministic writing $F_{o,D}$ but below the toggle switching threshold $F_{o,T}$, only a P state can be written. A second procedure is used to write the corresponding AP state. In this case, a single pulse with maximum fluence $F_{o,D} < F_{pulse} < F_{o,T}$ first ensures the magnetization is in the P state. Subsequently, the same region is exposed to a second pulse with maximum fluence $F_{pulse} > F_{o,T}$. The part of the pulse which meets this condition will then be able to switch the P region to AP. In figure 6.3b we experimentally demonstrate this scheme with Kerr microscopy images of samples exposed in the previously described manner. It can be seen that in the centers of all exposed areas (indicated by the black squares), the final state is indeed fully dependent on the writing procedure, and no longer on the initial magnetization state. Additionally we observe deterministic writing in the outer regions for the two-pulse procedure, due to the higher total energy of the second pulse. Nevertheless, the existence of any region where deterministic writing of both free layer states is possible is sufficient for applications using patterned media or by making use of plasmonic structures to provide local heating.[161] Although the use of two pulses might

6

somewhat limit the speed of this protocol, we have seen in chapter 4 that a second laser pulse can be used to switch the magnetization a second time in as little as 10 ps. Note that this only concerned 'simple' Co/Gd systems, and more experiments on the systems described in this chapter should be performed to determine the relevant timescales.

6.3   TUNING THE SPIN CURRENT MAGNITUDE

To verify that the origin of the symmetry breaking is truly non-local transfer of angular momentum, we investigate the impact of the magnitude of the generated spin current on the regime where deterministic writing is possible. Note that a more straightforward, though less quantitative verification is presented in appendix C.3. By tuning the Ni thickness in the reference layer, we change the total magnetic moment and consequently the magnitude of the spin current.[109] Here, a larger volume of magnetic material should result in a stronger spin current.

The thickness of each Ni layer (t_{Ni}) in the reference layer is varied from 0.5 to 1.0 nm, while keeping the amount of repetitions constant. We determine the threshold fluence for both deterministic writing and toggle switching ($F_{o,D}$ and $F_{o,T}$, respectively) for a range of t_{Ni}, using the same method as in figure 6.2a. Note that instead of preparing the sample in the AP or P state initially, this experiment is performed by exposing a sample prepared in the AP state to two identical subsequent laser pulses. This results in a ring-like domain as seen in the inset of figure 6.4a, as the first pulse will create a P domain, whereas the second will create a smaller AP domain within the first domain due to the higher threshold fluence $F_{o,T}$. This allows us to determine both sets of domain sizes from a single experiment, and reduces the variance between measurements. The extracted threshold fluences are presented in figure 6.4a. Here we observe two effects. Firstly, both sets of threshold fluences increase with increasing t_{Ni}. This behaviour can be explained by a decrease of optical absorption in the free layer with increasing reference layer thickness (see appendix C.2), as well as a probable increase in free layer roughness. More importantly, we observe that the gap between $F_{o,D}$ and $F_{o,T}$ also increases with t_{Ni}. This gap, defined as $\Delta F_o = F_{o,T} - F_{o,D}$, is plotted in figure 6.4b. The increase of ΔF_o is consistent with the hypothesis that the effect is driven by a spin current originating from the reference layer.

To verify the hypothesis more quantitatively, we model the trends for increasing t_{Ni}. To show that the increase in ΔF_o is not merely a consequence of scaling with the increase of both threshold fluences, we present this scaling as the purple dashed curve
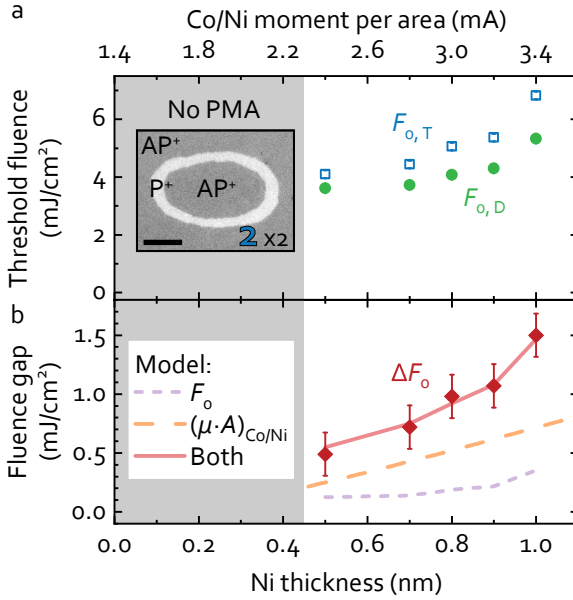
6

Figure 6.4: (a) The threshold fluence for switching from the AP state ($F_{o,D}$) and the P state ($F_{o,T}$) as a function of the Ni thickness t_{Ni} in the [Co(0.2)/Ni(t_{Ni})]$_{x4}$/Co(0.2) reference layer. The grey area indicates where t_{Ni} was too low to obtain PMA. Inset shows a Kerr microscopy image of a typical experiment used to obtain the threshold fluences, where a sample prepared in the AP state is exposed to two subsequent identical laser pulses with an energy of 300 nJ, yielding both domain sizes. Scale bar represents 20 μm (b) The difference ΔF_o between the fluences presented in (a). Lines indicate scaling behaviour with either these fluences, reference layer magnetic moment and optical absorption, or both combined. Error bars represent the standard deviation obtained through fitting.

in figure 6.4b. As it is clear that this behaviour alone can not explain the increase in ΔF_o, we now turn to the expected scaling of the spin current. The optically generated spin current should scale primarily with two factors, namely the magnetic moment of the reference layer ($\mu_{Co/Ni}$) and the optical absorption A. We model $\mu_{Co/Ni}$ as a function of t_{Ni} by assuming bulk values for the magnetization for each sublayer. For all proposed mechanisms of optical spin current generation, the spin current scales with the light absorption in either the magnetic layer (due to demagnetization[55,99]) or all metallic layers underneath (due to hot electron generation[98]). As the absorption in all layers should scale in the same fashion with increasing thickness, we use the absorption in the reference layer itself for the sake of simplicity. Moreover, it has been found in similar Co/Ni multilayers that the spin current originates from the full thickness of the generat-

ing layer.[109] We calculate the light absorption in the reference layer ($A_{Co/Ni}$) as a function of t_{Ni} by using a transfer matrix method[147,162] (see appendix C.2). The trend for both $\mu_{Co/Ni}$ and $A_{Co/Ni}$ is shown by the orange dashed curve in figure 6.4b. By now combining this with the scaling of F_0 discussed earlier, we find the red curve in this figure, which can be seen to adequately explain the increase of ΔF_0. This further confirms that the corresponding symmetry breaking is indeed the result of an optically generated spin current. Some effects are not included here, such as the dependence of the reference layer demagnetization rate on the multilayer composition. Indeed, different demagnetization dynamics could arise at high fluences for different Ni concentrations[163] or due to variation in the Curie temperature.[164] Moreover, it should be noted that the actual magnetization of the reference layer likely differs from the values assumed here due to an absence of perfectly sharp multilayer interfaces. However, assuming that these effects are small compared to the variation in absorption and magnetization we have shown that this relatively simple description can adequately explain the data. Finally, we would like to draw attention to the magnitude of the effect. For a $[Co(0.2)/Ni(1)]_{x4}/Co(0.2)$ reference layer the threshold fluence gap ΔF_0 has a relatively large magnitude, corresponding to 28 % of the base fluence $F_{0,D}$. This is expected to be scaleable towards even larger values, for instance by using stack engineering to increase the magnetization of the reference layer and light absorption in this layer.

In conclusion, we have experimentally demonstrated deterministic writing of the magnetization of a free Co/Gd bilayer using a fs laser pulse by using the symmetry breaking provided by a spin current generated in a neighbouring ferromagnetic Co/Ni reference layer. Moreover, we have demonstrated two protocols for reliably and controllably writing both (bit) states of the free layer, by using either one or two laser pulses. We have also shown that the spin current induced symmetry breaking scales as expected with the magnitude of the spin current generated in the reference layer, by tuning its composition. The system described here benefits from the strong binary threshold of all-optical switching and can provide a method to further enhance the general understanding of optically generated spin currents. In section 7.2.2 we model changing the delay between the arrival of the spin current and the switching of the free layer, showing that the resulting switching behavior could be used to investigate the spin current. Moreover, this system can provide insight into the role of spin transport versus local transfer of angular momentum in all-optical switching, which is essential for the implementation of future opto-spintronic devices, such as the optically written racetrack memory.[21,25,131] The deterministic magnetization writing presented in this chapter provides a stepping stone on the road to realizing such data storage devices.

6

7

FURTHER RESEARCH AND OUTLOOK

To conclude this thesis, we discuss additional research on all-optical switching and ultrafast spin currents in synthetic ferrimagnets. First we investigate novel synthetic ferrimagnets containing both Gd and Tb, showing the effect of the composition on AOS behavior and the stability of small domains. We also discuss preliminary measurements on the time-resolved dynamics of spin-current assisted AOS, and show modeling results using the s-d *model. The chapter concludes with a general outlook on further research and the potential technological applications of the work discussed in this thesis.*

7.1   SYNTHETIC FERRIMAGNETS WITH GD AND TB

The energy-efficiency and speed of all-optical switching (AOS) hold great potential for future data storage applications. However, the material systems investigated thus far have some drawbacks with regard to implementation. Here we focus on one specific factor, namely the anisotropy of the material, which is of crucial importance to facilitate high-density, stable data storage. In GdFeCo and GdCo alloys, it has been shown that nanostructures down to 200 nm in size can be all-optically switched.[87,127] For continuous media however, the minimum stable domain size after AOS has been reported to be up to tens of μm.[17,112,165] For Co/Gd bilayers, where the anisotropy originates from a Pt seed layer, it has been shown that the stable domain size in a continuous film is at most 2-5 μm.[166] It is clear that this is inadequate in order to be competitive in bit density with current hard disk drives, which are already working with bit sizes of only tens of nm.[*]

Due to its high intrinsic anisotropy, the rare-earth material Tb is a potential candidate for increasing the stability of magnetic domains in RE-TM systems. This anisotropy is magnetocrystalline in origin, and can be explained by taking a look at the orbital configurations of Gd and Tb. In these materials, the magnetic moment is carried primarily by the 4f electrons. As the 4f orbital of Gd has an orbital quantum number L of zero, the wave-function is symmetrical relative to the lattice.[49] This results in zero net spin-orbit coupling, and no intrinsic anisotropy of the 4f electrons. Instead, the anisotropy in Gd comes primarily from spin-orbit coupling of the 5d electrons, which is transfered to the 4f electrons via the exchange interaction.[167] In contrast, Tb ($L = 3$) has a non-symmetrical wave-function, resulting in high spin-orbit coupling for the 4f electrons and an anisotropy constant which is many times greater than that of Gd.[49]

Owing to this high intrinsic anisotropy, amorphous TbFeCo alloys have already been extensively researched[168,169] and have seen use in magnetic storage media. Stable domain sizes down to 50 nm have been created in TbFeCo alloys using local heating via plasmonic nano-antennas.[161] However, as discussed in chapter 5, AOS in systems where Tb is the only RE material is notoriously difficult. Indeed, consistent single pulse toggle AOS in TbFeCo alloys has to this date not been conclusively proven. Single pulse AOS has been shown in synthetic ferrimagnetic Co/Tb multilayers, albeit with a critical dependence on the Co and Tb thickness,[91,92] leaving little room for further engineering.

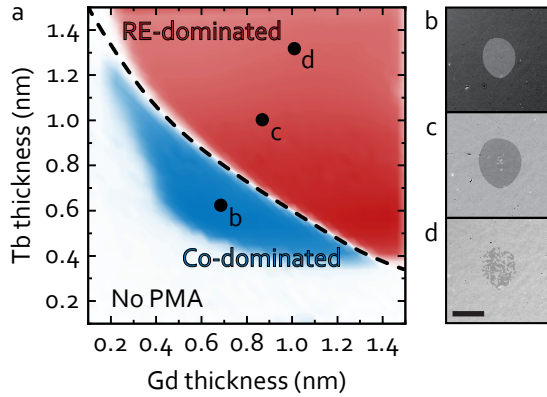*Based on areal densities of 0.1-0.3 Tbit/cm².

Figure 7.1: (a) Phase diagram of the hysteresis step of a Tb(y)/Co(0.8)/Gd(x)/Co(0.8)/Tb(y) sample measured using polar MOKE. The dotted line indicates the compensation region. (b,c,d) Kerr microscopy images of the magnetic state of the sample after excitation with a single fs laser pulse at approximate thicknesses indicated in (a). The scale bar represents 50 μm.

Systems containing both Gd and Tb offer an appealing alternative, using Gd as the main driving force for AOS while exploiting the high anisotropy of Tb. Recently, Ceballos et al. demonstrated single pulse AOS in GdTbCo alloys where Gd makes up at least 20 % of the total RE material.[35] The minimum stable domain size was not explicitly addressed in this work, but features down to a few μm are visible in Kerr microscopy images, potentially already providing an improvement on GdFeCo alloys. Although this system has some room for tuning, it is expected that the requirement common to alloys for the composition to be close to magnetization compensation still exists. Therefore, in this section we investigate AOS and domain stability in synthetic ferrimagnets containing both Gd and Tb.

7.1.1 COMPOSITION AND ALL-OPTICAL SWITCHING

The exact design of the synthetic ferrimagnetic stack is subject to two considerations. First off, as is the case with Gd, Tb has a Curie temperature (T_C) below room temperature (237 K); its magnetization needs to be stabilized by introducing an interface with a ferromagnet such as Co. Second, as the asymmetrical Dzyaloshinskii-Moriya interaction (DMI) could have an effect on the domain stability[166] and obscure the effect of Tb, we want to investigate a symmetrical multilayer stack where this effect is cancelled out. The choice is therefore made to investigate a Ta(4)/Tb/Co(0.8)/Gd/Co(0.8)/Tb/TaN(4) multilayer, where the Tb and Gd thicknesses are varied. By varying these thicknesses along

7

perpendicular directions on a single sample, we can investigate a wide composition range systematically while excluding any sample-to-sample variation.

We fabricate such a sample using DC magnetron sputtering, and investigate the static magnetic behavior, in order to determine for which compositions PMA is present. In figure 7.1a we show a phase diagram derived from the step in the hysteresis loop measured using MOKE, as a function of Gd and Tb thickness. No PMA is present for low Gd and Tb thicknesses, which can be understood as follows. As there are no Pt/Co interfaces in this stack, Tb is expected to be the main source of PMA. For sputter deposition of low Tb thicknesses (<0.4 nm) it is reasonable to assume that no closed layer has formed, which could be detrimental to achieving PMA. At too low Gd thicknesses we expect that the two Co layers are too strongly coupled, leading to an in-plane shape anisotropy which overcomes the Tb-induced anisotropy. For thicknesses where PMA is present, we observe a transition from Co-dominated to RE-dominated behavior.* The compensation line separating these regions is indicated by the dotted line in the figure. The curvature of this line indicates that the profiles of the induced magnetization are not the same in Tb and Gd, which might be expected due to their respective locations within the stack.

We now investigate AOS behavior as a function of composition by exposing the sample in several locations to a single fs laser pulse with a fixed energy, and show Kerr microscopy images in figures 7.1b, 7.1c, and 7.1d. In the first two locations we find consistent single pulse AOS, demonstrated for the first time in these hybrid synthetic ferrimagnets. However, for higher Gd and Tb thicknesses, only a multi-domain state is present. As discussed in chapter 4, this state arises when the phonon temperature temporarily exceeds T_C. Due to the low T_C of Gd and Tb, the effective T_C of the system decreases when adding RE material. Therefore the same amount of heating can bring the sample above T_C, fully quenching the magnetic moment and preventing AOS. Indeed, the resulting multi-domain state is already visible in figure 7.1c, although here it only occurs in the middle of the laser pulse, where the fluence is highest. In figure 7.1d, the fluence needed to quench the magnetization is larger than the switching threshold fluence, resulting in only a multi-domain state being formed. This imposes some limits on the extent to which the thicknesses in this system can be tuned, although a more systematic study would be needed to better understand these limits.

To get a clearer picture of the influence of Tb on AOS behavior, we fabricate several samples with varying Tb thickness, but a constant Gd thickness (1 nm). We extract

7

---

*Due to the sensitivity of MOKE to only the Co magnetization, this is apparent in an inversion of the hysteresis loop.
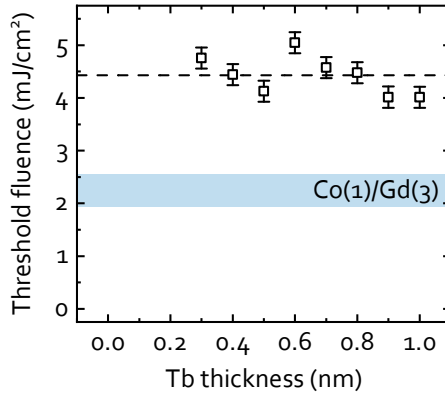
Figure 7.2: Threshold fluence for AOS in a Tb(x)/Co(0.8)/Gd(1)/Co(0.8)/Tb(x) sample. The blue band indicates the typical threshold fluence range for a Co(1)/Gd(3) sample.

the threshold fluence needed for AOS as a function of Tb thickness using the method described in chapter 6, and plot the results in figure 7.2. No clear trend is observed here, leading to the preliminary conclusion that Tb does not (actively) contribute to the AOS process in these samples. This is somewhat surprising considering the potential for AOS in Co/Tb multilayers.[91] In the work on GdTbCo alloys, the threshold fluence was found to increase with increasing Tb concentration,[35] which however also entails removal of Gd from the system. One might expect that upon increasing the amount of magnetic material by adding more Tb, our system would require more energy to sufficiently quench the magnetization for switching. However, it is important to note that at these thicknesses the laser pulse is not fully absorbed. Hence, adding more material also allows for more energy to be absorbed by the stack.

It is plausible that due to its low T_C, the Tb moment is fully quenched by the laser pulse, and aligns opposite to the (switched) Co upon remagnetization due to direct exchange coupling at the interface. Time-resolved measurements of the magnetization dynamics could shed more light on the exact switching process of Tb, and its influence on Co and Gd. Although element-selectivity can be achieved using X-ray measurements,[19] these are complicated experiments requiring access to dedicated facilities. As a more straightforward alternative, one could exploit the wavelength-sensitivity of MOKE to Tb and Co. It has been shown that Tb becomes the dominant contributor to the MOKE signal in TbCo alloys at wavelengths below 600 nm, making it possible to measure time-resolved MOKE in an element-selective manner.[170,171]
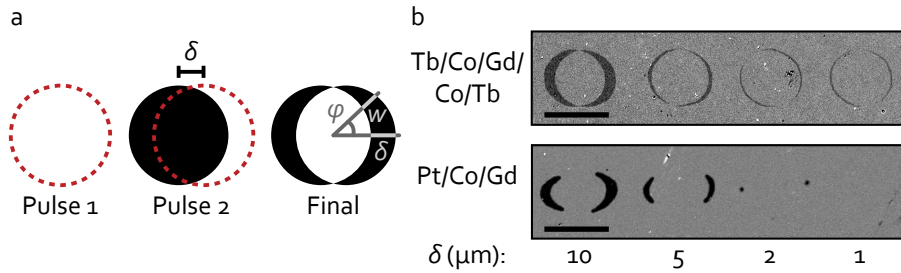
7

Figure 7.3: (a) Sketch of the process to create small domains using AOS to investigate domain stability. (b) Kerr microscopy images of domains created using this process on two different samples. Pt/Co/Gd results adapted from ref. 166. Scale bars represent 50 μm.

In passing, we note that value of the threshold fluence of approximately 4.5 mJ/cm² is around twice as high as the fluences of 2 to 2.5 mJ/cm² generally found for a Co(1)/Gd(3) system (indicated by the blue band in figure 7.2). Several factors make it difficult to disentangle this discrepancy, even when assuming that Tb does not assist or hinder switching in any way. On the one hand, the total Co thickness in our system is greater (1.6 nm), which would already cause a large increase of the threshold fluence, as was found by Lalieu et al.[20] Moreover, the Gd thickness is close to the magnetization decay length in Gd (~ 0.5 nm), leaving less magnetized Gd able to contribute to AOS compared to stacks with 3 nm of Gd. Conversely, there are also two Co/Gd interfaces, which could stabilize a larger total magnetic moment in Gd. To complicate matters further, preliminary results indicate that substrate choice can also have a large effect on the switching behavior in these systems. The current conjecture is that substrates with poorer heat conductivity reach higher temperatures during sputter deposition, driving increased intermixing. A more systematic study, controlling for as many variables as possible, is necessary to fully grasp the intricacies of AOS in these systems.

7.1.2   DOMAIN STABILITY

We now return to our stated goal of finding a high-anisotropy system capable of AOS. In order to determine the minimum stable domain size in our Tb/Co/Gd/Co/Tb system, we use the approach proposed by Cao et al.,[166] which is sketched in figure 7.3a. Here we expose the sample to two subsequent single fs laser pulses, while moving the sample with a distance δ between the two exposures. Toggle switching results in the formation of two crescent-shaped domains with a maximum width δ, which (ideally) meet at an infinitely sharp point. Due to the energy cost associated with the stabilization of a

domain wall, the domains are generally unstable at these tips. They will therefore start to shrink, whereby the width at the tip will gradually increase. At a certain point the minimum stable domain size is reached. We perform this experiment for different values of δ, and show Kerr microscopy images taken 5 minutes after exposure in figure 7.3b. Results from the same experiment performed on Pt/Co/Gd by Cao et al.[166] are shown for comparison. The most apparent result is the existence of stable domains in our sample for a δ of 2 and 1 µm, whereas these have already (mostly) disappeared in the Pt/Co/Gd sample. Clearly the minimum stable domain size in our Tb/Co/Gd/Co/Tb system is significantly lower than in Pt/Co/Gd.

Although the actual minimum width of the domain that remains is below the resolution of the Kerr microscope (~ 1 µm), we can make an estimate using the angle between the two domain edges. As sketched in figure 7.3a, we define φ as the angle between the displacement axis and the line intersecting the domain at the desired width w. From geometric considerations it can be derived that $w = \delta \cdot \cos \varphi$. For a δ of 1 µm, we then find $\varphi_{max} = 75 \pm 5\,°$, giving $w_{min} = 0.3 \pm 0.1$ µm. This is quite a large improvement on Pt/Co/Gd and GdFeCo systems, and it is plausible that further sample optimization would make it possible to reach the desired sizes of ~ 50 nm. Other techniques, such as *magnetic force microscopy*, would be needed to properly image domain sizes below 1 µm. A better understanding of the origin of the anisotropy in these samples could be obtained in future experiments by directly measuring the anisotropy, for instance using hard-axis hysteresis loops.

For applications, it would be interesting to investigate the efficiency of domain-wall (DW) motion in these samples. There are indications that Tb could give rise to a large spin Hall angle,[172] which could drive efficient DW motion using the spin Hall effect.[173] Note that the symmetry of the system should be broken in this case, so as not to cancel the net torque on the magnetization. Moreover, it is also relatively easy to tune the compensation in these systems, which is beneficial for exchange-torque-induced DW motion.[24]

Concluding, these results show that synthetic ferrimagnets containing both Gd and Tb are an interesting platform for optically written data storage. These systems exhibit consistent AOS over a significant range of layer thicknesses, and are able to contain stable sub-micron domains.

7

7.2   SPIN-CURRENT ASSISTED ALL-OPTICAL SWITCHING DYNAMICS

In chapter 6 we demonstrated the concept of *spin-current assisted all-optical switching* (SCA-AOS). Recapping, we used a spin current coming from a ferromagnetic reference layer to influence AOS and thereby deterministically set the magnetization state in a Co/Gd bilayer regardless of its initial state. Although this result has some interesting applications, we do not yet know much about the behavior at the ps timescale and the physics at play. In this section we present preliminary time-resolved MOKE measurements as well as calculations using the s-d model, which can be used as a starting point for a more in-depth investigation of SCA-AOS.

7.2.1   TIME-RESOLVED MOKE MEASUREMENTS

To better understand the effect of the spin current on AOS dynamics, measurements of the dynamics at the (sub-)ps timescale are essential. Although element-selective X-ray measurements would provide the most complete picture, as a more straightforward starting point we turn to time-resolved MOKE measurements. A drawback here is that only the transition metal dynamics (Co and Co/Ni) can be measured, and the Gd dynamics are inaccessible. Additionally, measuring AOS dynamics in a stroboscopic experiment poses a peculiar difficulty. As the magnetization switches between 'up' and 'down' with every pulse, the measured dynamics for each subsequent cycle will have the opposite sign and thus cancel each other out. A solution to this problem, proposed by Peeters et al., is to discard the signal of every other pulse before it reaches the lock-in amplifier.[77] For a typical toggle AOS process in a sample initialized in the 'up' state, measuring only the odd-numbered pulses as a function of pump-probe delay will then give the AOS dynamics for switching from 'up' to 'down', and vice versa for the even-numbered pulses.

   An added complication arises when applying this method to measuring the dynamics of SCA-AOS. Now, for a sample initialized in the anti-parallel (AP) state and a relatively low laser fluence, switching only occurs with the first incident laser pulse. Therefore a stroboscopic measurement would not pick up any pump-induced changes, no matter which pulses are measured. Alternatively, an external field could be used to reset the Co/Gd bilayer between each laser pulse. However, in typical samples used for SCA-AOS, the coercive field of the Co/Ni multilayer is lower than that of the Co/Gd bilayer
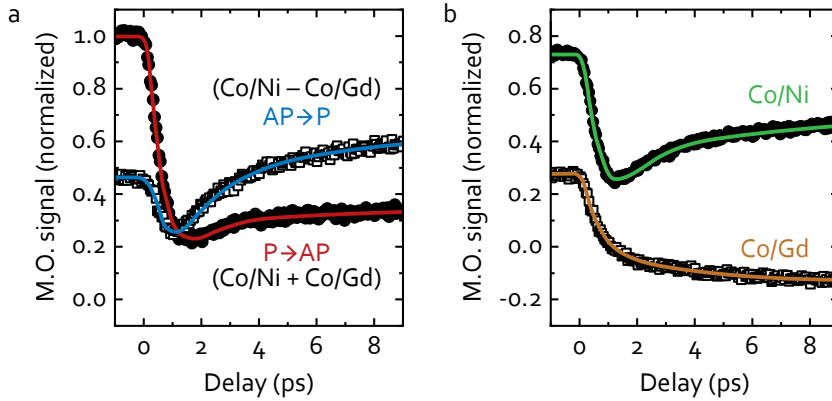
7

Figure 7.4: TR-MOKE measurements of spin-current assisted all-optical switching in a [Co/Ni]$_{x4}$/ Cu/Co/Gd sample. (a) Measurement when starting from the parallel (anti-parallel) state giving the sum (difference) of the two contributions. (b) Separated Co/Ni and Co(/Gd) dynamics via respectively adding and subtracting the signals from (a).

(see figure 6.1a). An applied field which is large enough to reset the Co/Gd bilayer after an AOS event will then also switch the Co/Ni multilayer, resulting in a parallel (P) alignment. As it is not possible to measure the switching dynamics within the fluence gap in a stroboscopic manner, we will limit the current investigation to dynamics at higher fluences, where switching is a toggle process again. We would then expect to see a speeding up of the switching dynamics when starting from the AP state as compared to the P state, analogous to the experiment of Malinowski et al. (see figure 2.3b and ref. 36).

A final consideration needs to be made due to the disparate magnetic layers in our [Co/Ni]$_{x4}$/Cu/Co/Gd samples. Because the total stack thickness is smaller than the laser penetration depth (~ 20 nm), both the Co/Ni multilayer and Co in the Co/Gd bilayer will contribute to the MOKE signal. If the laser fluence is chosen carefully, the Co/Ni multilayer will demagnetize and remagnetize to its original state between pulses, while the Co/Gd bilayer will switch with every pulse. For now we are mainly interested in the switching signal, which becomes more difficult to parse with the addition of the demagnetization signal.

This is illustrated in figure 7.4a, where we show results from time-resolved MOKE measurements using the previously described scheme to measure only the odd- or even-numbered pulses. When preparing a sample in the P state, measuring the odd-numbered pulses results in a signal which is the sum of the Co/Ni and Co/Gd signal. After

7

every odd-numbered pulse the Co/Gd bilayer has switched, and the Co is anti-parallel to the Co/Ni. Therefore, the signal from the even-numbered pulses consists of the Co/Gd signal subtracted from the Co/Ni signal. It is clear that these signals are difficult to parse; any difference in the switching behavior between the initial states becomes obscured.

Due to the fact that the Co/Ni multilayer remains in the same orientation, whereas the Co/Gd bilayer switches with every pulse, the signal from the two layers can be isolated, as is shown in figure 7.4b. The Co/Ni signal is obtained by adding the signal from the odd- and even-numbered pulses (and dividing by two). Taking the difference between the signals instead gives the Co/Gd signal. Here it is good to once again note that only the dynamics of Co in the bilayer can be measured with this technique.

The striking difference between the dynamics of the two layers now becomes clear, with typical de- and remagnetization behavior observed for the Co/Ni multilayer and switching behavior for the Co/Gd bilayer. The latter is similar to the switching dynamics measured by Peeters et al. for a solitary Co/Gd bilayer,[77] showing a zero crossing within a few ps and a slower relaxation towards saturation. It is important to notice that this approach actually does not provide information on the effect of the spin current on AOS dynamics. Because the isolated signals are in equal parts made up from the contributions from both the P and the AP state, we end up with one set of signals where the difference between these two situations is averaged out. To alleviate this problem, one final ingredient needs to be introduced.

As discussed in section 3.1.2 and already utilized in chapter 5, *complex MOKE* can be used to filter out the signal of the Co/Ni multilayer. Hysteresis loops are measured as a function of the angle of a quarter-wave plate inserted in the probe beam. At a certain angle the step in the hysteresis loop belonging to the Co/Ni multilayer vanishes, and only the signal of Co in the Co/Gd bilayer is left. By now measuring the time-resolved dynamics for odd- and even-numbered pulses, we obtain the AOS dynamics for switching from the P to the AP state and vice versa, respectively. A preliminary time-resolved MOKE result is presented in figure 7.5, with the inset showing the time-derivative of the Co/Ni dynamics seen in figure 7.4b as an indication of the spin current.[99,110] Note that the signal-to-noise ratio is significantly worse than before; this is a consequence of using complex MOKE, as unavoidably also signal from the desired layer is lost.

There indeed appears to be a difference between the switching dynamics depending on the initial state. Compared to the P state, when starting from the AP state (where the spin current assists switching) the magnetization crosses zero sooner, and reaches a higher absolute value before the dynamics begin slowing down. Considering that the
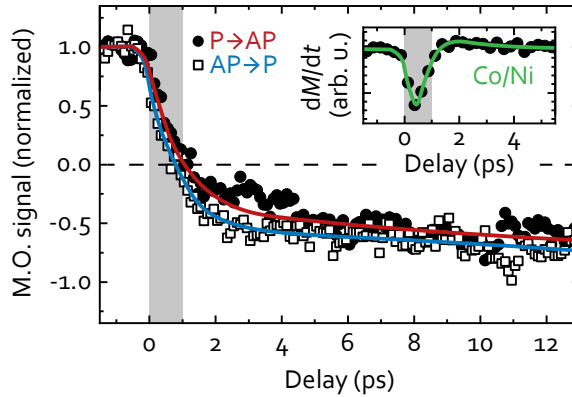
7

Figure 7.5: Time-resolved magnetization dynamics of spin-current assisted AOS measured using complex MOKE to filter out the Co/Ni dynamics. The inset shows the time-derivative of the Co/Ni signal. The gray band in both graphs indicates the time during which this time-derivative is largest. Lines are guides to the eye.

approximate temporal profile of the spin current (shown in the inset) shows a peak in the first ps after the pump pulse hits, it is not surprising that the deviation between the datasets also grows in this timespan. This deviation seems to remain constant after the spin current has decayed, and the dynamics are governed only by intrinsic remagnetization processes and heat diffusion.

It should be noted that these are preliminary results, and more systematic measurements with a better signal-to-noise ratio are needed to draw concrete conclusions. One barrier that needs to be overcome here is the relatively high threshold fluence for switching in these samples. The high fluences needed lead to heat-induced changes in the magnetic behavior of sample over time, which limits both the maximum measurement time and the range of fluences that can be investigated. As discussed in chapter 6, the high threshold fluence could be a consequence of the growth of Co/Gd on rougher interfaces; other sample geometries should therefore be considered for further research. Here the high anisotropy of Tb could once again be exploited, as the main difficulty in designing samples for SCA-AOS is the need for PMA in both the reference layer and the switching layer.

7
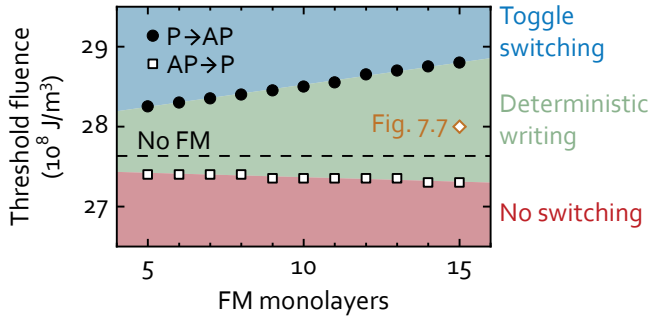
Figure 7.6: Threshold fluence for AOS in an FM/Cu/Co/Gd stack calculated using the s-d model. The dashed line indicates the threshold fluence in the absence of the FM reference layer.

7.2.2 MODELING SPIN-CURRENT ASSISTED AOS

Next to time-resolved measurements, modeling can provide valuable insights into the dynamics of SCA-AOS. Of the two models used in this thesis, the M3TM and the s-d model (sections 3.2.1 and 3.2.2), the latter is clearly more suitable due to its ability to describe non-local dynamics. The structure is described as a series of pure atomic monolayers, analogous to the implementation of the M3TM in ref. 89. We use a generic ferromagnet as the spin-current generating reference layer, and implement the non-magnetic spacer layer by setting the exchange coupling between the ferromagnet and the Co/Gd bilayer to zero. The assumption that the spin current instantaneously equilibrates across the layers is also valid in the structures considered here. Material parameters are taken from references 89 and 101, with the exception of a reduced Co and FM Curie temperature (T_C) of 1000 K chosen to better reflect the thin film nature of the system. It is worth bearing in mind that quantitative predictions should not be expected, as the exact choice of material parameters strongly influences the numerical results.

To determine if the model is capable of reproducing the experimental observation of SCA-AOS, we simulate the magnetization dynamics as a function of laser fluence for a system initialized in the P and in the AP state. We extract the threshold fluence from the magnetic state after several tens of ps, and plot this result as a function of the amount of monolayers in the reference layer (n_{FM}) in figure 7.6. We indeed find a significant difference in the threshold fluence between the two initial states, which grows with increasing reference layer thickness. This result also agrees with the experimental observation in figure 6.4. In contrast to the experiment, the model predicts a slightly

decreasing threshold fluence with increasing n_{FM} when starting in the AP state. This can be simply understood, as the main cause for the rising trend seen in the experiment is assumed to be growth-related changes of interfaces, which are of course not taken into account here.

A second interesting observation relates to the threshold fluence in the absence of a reference layer, indicated by the dotted line in the figure. Looking at this value we find that the spin current mainly hinders switching from the P state, while the degree of assistance when starting from the AP state is significantly smaller. Due to the same growth-related issues previously mentioned, this would be difficult to experimentally investigate; a 'pure' measurement of only the effect of increasing spin current strength hardly seems possible. However, if a reversed (Co/Gd/Cu/FM) stack could be fabricated, a spin sink such as Pt (see appendix C.3) could be inserted between Cu and the FM layer without affecting the intrinsic switching behavior of the bilayer. In exploratory attempts, achieving PMA with a traditional Co/Ni multilayer as FM layer has proven to be a challenge. However, Tb could again be used to strengthen the anisotropy. The arrival of the spin current in Gd first rather than in Co could also lead to different results, which would require systematic investigation. Alternatively, the switching layer could instead be a Co/Gd/Co stack, such that the spin current again arrives first in a Co layer.

Finally, it is good to note that although the material parameters have hardly been tweaked, the relative difference in threshold fluence is similar to that found in experiment. Specifically, we find a relative fluence gap of approximately 10 % for n_{FM} = 15, close to the experimental range of 10 to 20 %, giving confidence that the model description is sensible.

Next we can take a look at the time-resolved dynamics for a laser fluence where switching is one-directional. A fixed laser fluence of $28 \cdot 10^8$ J/m^3 and n_{FM} = 15 gives the curves shown for the parallel and anti-parallel state in figures 7.7a and 7.7b, respectively. Note that for the sake of clarity, the reference layer instead of the bilayer has been switched to obtain the anti-parallel state. The behavior found here is as expected, with only de- and remagnetization found in the P state, whereas the Co/Gd bilayer switches when starting from the AP state. Note that switching of the Gd layer takes place on a timescale of several tens of ps, and is not visible in this figure.

The FM layer is also affected by the spin current generated by Co and Gd, as evident in the difference in the maximum quenching between the two states. In fact, when increasing the laser fluence above $36 \cdot 10^8$ J/m^3 (not pictured), the FM layer is also found to switch. This is consistent with observations in FM/Cu/GdFeCo systems,[111,112] but is
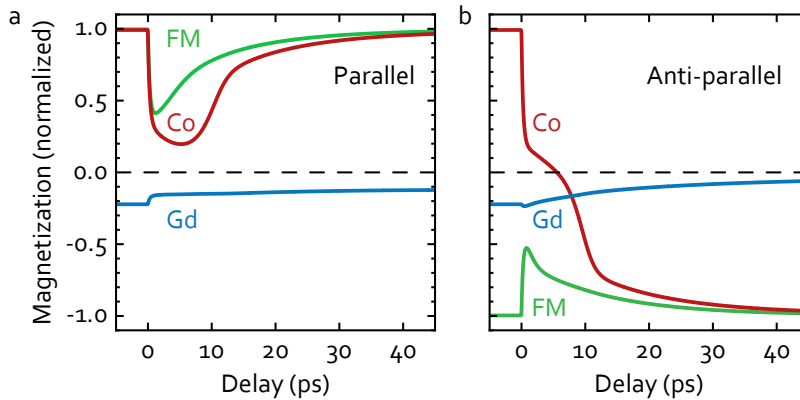
7

Figure 7.7: Laser-induced magnetization dynamics in an FM/Cu/Co/Gd stack calculated using the s-d model for (a) parallel) and (b) anti-parallel alignment of FM and Co. Laser fluence is the same in both situations.

not observed in our experiments. For higher fluences we experimentally instead find full demagnetization of the Co/Ni reference layer, evident by a multi-domain state after relaxation (see appendix C.4). As one explanation of this discrepancy, it is possible that the T_C of the FM layer is too high in our model description, as in the experiment it would be closer to that of the main component, Ni (627 K). A lower T_C could entail a complete quenching of the Co/Ni moment at higher fluences, preventing a spin current from the Co/Gd bilayer from switching the reference layer. At the same time, the spin current responsible for switching the FM layer in FM/Cu/GdFeCo systems was found to be dominated by the Gd contribution. Although we have shown that this contribution can still be large in layered Co/Gd systems in chapter 5, in this case this spin current would have to pass through the Co layer in order to reach the reference layer, already reducing its magnitude. To investigate the possibility of switching the FM layer in these systems, the previously discussed Co/Gd/Cu/FM stacks could be used here as well.

It is also interesting to note the large difference in the Gd dynamics between the two states in figure 7.7. Starting from the P state a rapid demagnetization of Gd is followed by slow dynamics over a longer timescale; in the AP state the rapid demagnetization is absent, and the Gd magnetization is even slightly enhanced at very short delays. This is a clear effect of the spin current generated by the FM layer, which is aligned antiparallel to Gd in the P state (and thus assists demagnetization), and vice versa. We can see this as an indication that, no matter where in the bilayer the spin current is absorbed, it has the same qualitative effect on AOS. In the P state for instance, the spin current would
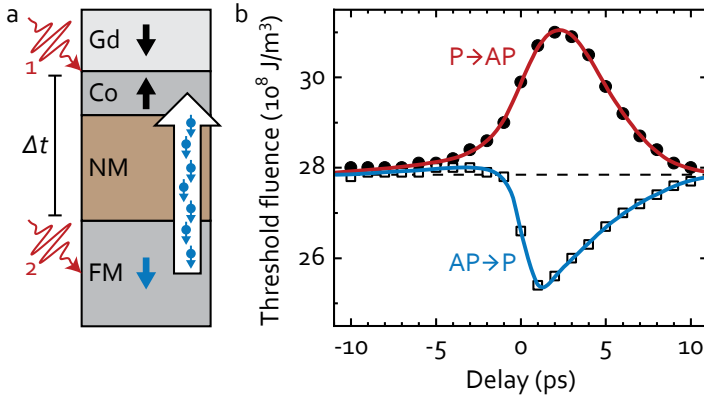
Figure 7.8: (a) Sketch of the sample geometry to measure SCA-AOS for different time delays t between AOS and spin current injection. (b) Calculated threshold fluence using the s-d model of the threshold fluence as a function of the delay between the two laser pulses in (a). Lines are guides to the eye.

hinder demagnetization of Co, and assist in Gd. For both materials it would be more difficult to form the transient ferromagnetic state necessary for switching;[19] sufficient quenching of Co would be prevented, or the Gd moment would be reduced such that the angular momentum transferred is insufficient to pull the Co moment through zero. We note that the slowing down of the Co dynamics around the zero crossing in figure 7.7b does not seem present in the time-resolved MOKE measurements of figure 7.5. This discrepancy was also noted in the M3TM in chapter 4 and ref. 77, and is likely an artefact of treating the magnetization as a single spin for each layer and neglecting thermal fluctuations, which is common factor in both models.

As a final use case of the s-d model we investigate a novel sample geometry, sketched in figure 7.8a, which can be used to study ultrafast optically generated spin currents. Although the materials and their order are the same as in the previous discussion and experiments, the difference lies in the thickness of the non-magnetic (NM) spacer layer. Here, this thickness is chosen such that a laser pulse impinging from the top of the sample will not (directly) heat the FM layer. For Cu approximately 99 % of the light would be reflected or absorbed for thickness of 50 nm onwards. The idea is now that the FM layer can be excited separately from the Co/Gd bilayer with a second laser pulse from the bottom of the sample through a transparent substrate. The time delay Δt between the two laser pulses can then be varied, depositing the angular momentum

from the spin current into the Co/Gd bilayer at different times. *

We implement this system in the s-d model by defining two sets of electron and phonon temperatures, one for the Co/Gd bilayer and one for the FM layer. These can then be separately excited by Gaussian laser pulses with a time delay Δt. The FM layer is now excited by a pulse with a fluence of $30 \cdot 10^8$ J/m^3, whereas the fluence for the bilayer is again varied to find the threshold fluence. Doing this for both the P and AP state as a function of the delay between the two pulses gives the result shown in figure 7.8b. Understanding the exact shape of the curves is quite complicated, as the effect of the spin current is in essence a convolution of the profile of the spin current and the magnetization dynamics of the switching layers. As there is also an effect of the former on the latter and vice versa, reducing the observed behavior to the spin current profile is exceedingly difficult. However, some interesting observations can still be made.

The highest difference in threshold fluences is found for delays of 1 to 3 ps, which is when the Co and Gd dynamics are evolving rapidly. This implies that, in this description, adding additional angular momentum to the system at lower time delays, while it is still demagnetizing is not optimally effective; the angular momentum acts more efficiently when the net Co and Gd moments are already low. In fact, the magnitude of the maximum fluence gap increases from 10 % at zero time delay to 18 % at its maximum. There is also a marked difference in the shape of the curves for the two initial states. An asymmetry is present in the curve for the AP state, but nearly absent in the curve for the P state. This could potentially be a second order effect, namely the result of the spin current from the Co/Gd bilayer acting on the FM layer, affecting its dynamics and therefore modifying the spin current generated by the FM. Additionally, there appears to be a slight increase of the threshold fluence for switching from the AP state for negative time delays. Potentially this is the result of the remagnetization of the FM layer generating a spin current with the opposite polarization, due to the source term scaling as $\frac{dm}{dt}$.

Implementing this scheme in an experiment poses some challenges. As a consideration for sample design, PMA is needed in the Co/Gd layer, which would now be grown on a thick Cu layer. Any crystalline texture induced by the seed layers at the bottom of the stack, needed for inducing PMA via a Pt/Co interface, is likely lost within the Cu layer. Here Tb could again come to the rescue, for instance in the form of a Co/Gd/Co/Tb switching layer. Additionally, aligning the two laser beams to illuminate the same area of the sample could also be challenging. Nanofabricated markers could

---

*Although the travel time of the electrons through the NM layer would already cause a delay, a Fermi velocity of $1.57 \cdot 10^6$ m/s for Cu[174] gives a delay of 32 fs, which is very close to the limits of the experimental resolution.

assist in this process, using reflectance measurements to accurately overlap the beams. Measuring the time-resolved dynamics of this system itself is likely quite complicated, as the accumulated heating from two laser pulses could quickly become prohibitive for stroboscopic measurements. A major benefit in this approach therefore lies in the setup only requiring single-shot switching. The created domains can be straightforwardly analysed using Kerr microscopy, which could give quite reliable results. In combination with a more rigorous implementation of the s-d model, this experiment could add to the body of knowledge on ultrafast optically generated spin currents, while also providing some insights into the crucial factors in AOS itself.

7.3 GENERAL OUTLOOK

The results presented in this thesis demonstrate the diversity of the physics that can be investigated using synthetic ferrimagnetic layered systems. We have seen that the intersection of many fascinating physical phenomena enables rapid repeated AOS (chapter 4), spin current generation (chapter 5), and the use of external spin currents for novel functionality(chapter 6). In regard to the latter two results, we have shown that these systems can even function as a probe of the often elusive non-local processes inherent to ultrafast magnetization dynamics (chapter 5 and section 7.2). Naturally there are still burning fundamental questions on the microscopic origins of all types of laser-induced ultrafast magnetization dynamics. However, we have shown that existing models such as the M3TM and the s-d model can at least qualitatively reproduce the novel experimental observations, giving confidence that we are on the right track towards better fundamental understanding.

   Circling back to technological applications, the systems investigated here show robust operation and a versatility that can be exploited in several device architectures. For instance, one spintronic device which is starting to see use in commercial products is the magnetic tunnel junction (MTJ),[28] which uses electrical currents to both switch and read out the magnetization. As discussed in section 1.2, hybrid opto-spintronic MTJs using Co/Gd bilayers have been demonstrated with a high tunnel magnetoresistance and robustness in the face of industrial processing steps.[32] In these devices, writing would be performed via AOS, whereas the reading process remains in the electrical domain. Although this yields a massive speed boost in terms of writing, the toggle switching limitation of AOS would be a hindrance to the efficient functioning of a device; either a read or a reset operation is required before a write operation can take place. Integrating SCA-AOS in these devices would provide a way around this issue, making it

7

possible to write a bit without having to know the initial state. Although the need for two laser pulses to write one of the two bit states somewhat complicates the device, we have shown that switching events in Co/Gd bilayers can take place within 10 ps. Therefore this need not be a hindrance to the operation speed of the device.

An alternative device geometry exploiting plasmonics could circumvent the need for two laser pulses altogether. It has been demonstrated in GdFeCo/SiN/GdFeCo structures where the light is coupled in via a prism, that the absorption can be localized to either the top or the bottom GdFeCo layer depending on the polarization of the laser pulse.[175] Now envision an all-optically switchable multilayer, sandwiched between two ferromagnetic reference layers with opposite magnetization. By careful plasmonic design, the system could then be engineered such that a laser pulse will excite the switchable layer and only one of the two reference layers, depending on its polarization. With the proper laser fluence, the choice of polarization then uniquely defines the final state of the switchable layer, requiring only a single laser pulse.

Synthetic ferrimagnets are particularly promising for future spintronic devices due to their inherent versatility; engineering of layers affords a wide spectrum of possibilities for optimization and functionality. As demonstrated in section 7.1, Tb can be used to maintain PMA and stabilize small domains without sacrificing AOS efficiency. Additionally, the already low energy consumption inherent to AOS could be further reduced by careful engineering of intermixing[133] and optical absorption.[176] At the same time, thermal engineering is essential to ultrafast device operation, as demonstrated in chapter 4. It should be noted that although repeated writing of the same bit at a frequency of 10 GHz is not a likely scenario, thermal engineering is still essential to prevent device degradation due to accumulated heat, even at lower operating frequencies.

Finally, possibilities at the intersection with the emerging field of integrated photonics should not be understated. All-optical switching makes it possible to convert information from the optical domain directly into the magnetic domain, without the need for intermediate electronics. These processes also inherently have a strong nonlinear response, and magnetic systems in general present a tried and tested way to store information in a non-volatile manner. These are factors which are highly sought after in current photonic technology, potentially paving the way for synthetic ferrimagnetic spintronic devices to function as crucial building blocks for the ultrafast and energy-efficient data processing devices of the future.

7

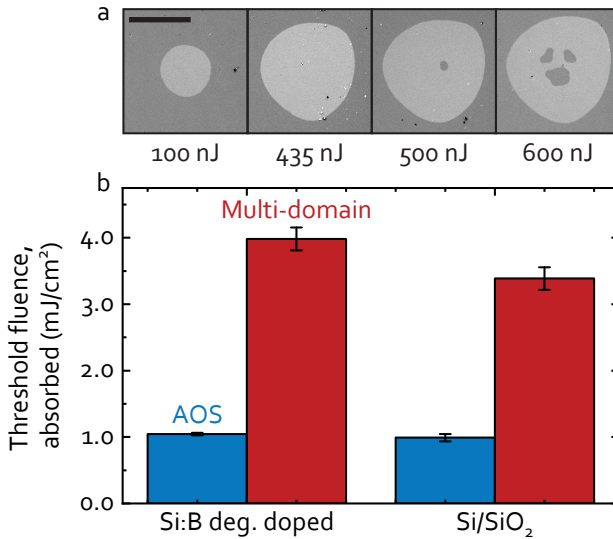# Appendix A

SUPPLEMENTARY INFORMATION FOR CHAPTER 4

Figure A.1: (a) Kerr microscopy images of a Si:B//Ta(4)/Pt(4)/Co(1)/Gd(3)/TaN(4) sample after exposure to single fs laser pulses with indicated total energy. The scale bar represents 50 μm. (b) Threshold fluence, corrected for absorption, for single laser pulse AOS and multi-domain formation on both Si:B and Si/SiO$_2$ substrates.

A.1   THRESHOLD FLUENCE FOR AOS AND DEMAGNETIZATION

Due to a lack of data on the thermal conductivity of the Si:B and Si/SiO$_2$(100) substrates used, we have performed additional experiments to gain an indirect measure of this parameter. The first experiment is presented here, and involves exposing Co/Gd samples to single fs laser pulses with varying total energy. After exposure, we again image the magnetic state of the samples using Kerr microscopy, of which we present some representative images in figure A.1a. The size of the written domain size increases with increasing laser pulse energy, which is simply a consequence of the Gaussian profile of the energy density of the pulse. Moreover, above certain laser pulse energies (in this case ~ 500 nJ) a random multi-domain state will form in roughly the center of the switched area. As mentioned in chapter 4, this occurs when the laser energy is so high that the magnetization is fully quenched and remagnetizes into a pattern driven by dipolar interactions. This only occurs when the phonon temperature exceeds the Curie temperature after equilibration with the electron temperature.[17] This logically also depends on the thermal conductivity of the sample, as a substrate that more efficiently

conducts heat away from the metallic layers should equilibrate to a lower temperature. Therefore, comparing the laser energy at which a multi-domain state begins to appear within the switched region between samples can give us an idea of the relative thermal conductivities of the samples.

To be able to properly compare the two substrates, we first determine the threshold fluence for AOS on both substrates. This can be done by extracting the area A of the switched domain as a function of the laser pulse energy E and fitting the data with[20,177]

$$A = \pi r^2 \times \ln\left(\frac{E}{F_0 \times \pi r^2}\right). \tag{A.1}$$

Here, r is the radius of the laser pulse, defined as the standard deviation of the Gaussian energy density distrubtion, and F_0 is the threshold fluence. A complicating factor here is the difference in optical properties between the two substrates, meaning that we should compare absorbed rather than incident laser pulse energy. The most significant difference is the SiO_2 layer, which acts as a reflective coating, increasing the absorption in the metallic stack.[176] To calculate the absorbed fraction of the laser pulse energy in the metallic stack, we perform transfer matrix calculations.[147] This gives the threshold fluences plotted in figure A.1b, which are found to be the same for both substrates. This is expected, as the occurrence of AOS is driven by the immediate rise in temperature of the electron system,[17] and is therefore not influenced by the substrate thermal conductivity.

We now extract the energy E at which a multi-domain state starts to appear within the switched area from our Kerr microscopy images. The value is defined as the average of the pulse energy where a multi-domain state is first observed and the next-lowest pulse energy that was applied, with the error given by the difference between this value and the two applied pulse energies. When again corrected for absorption, filling this in in equation (A.1) together with the laser radius r obtained from the fit gives the threshold fluence for multi-domain formation, plotted as the red bars in figure A.1b. We clearly find a lower threshold fluence for the Si/SiO_2 substrate as compared to the Si:B substrate, indicative of lower thermal conductivity at the relevant timescales for repeated AOS.
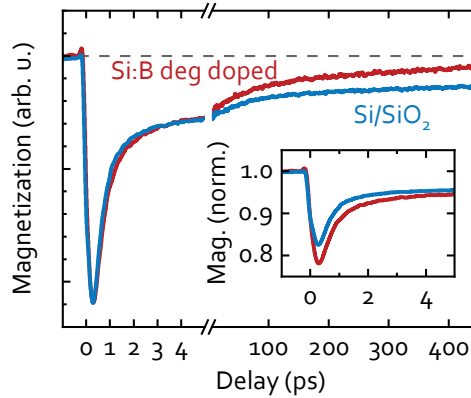
Figure A.2: Time-resolved MOKE measurements of low fluence demagnetization of Co(1)/Gd(3) bilayers on two different substrates. This experiment mainly measures the Co dynamics. Here the measurements are normalized to the maximum demagnetization to facilitate comparison. The inset shows the raw data, normalized instead using magnetic hysteresis measurements.

A.2   TIME-RESOLVED MOKE MEASUREMENTS

As a second experiment to characterize the thermal conductivity of the substrates, we perform time-resolved MOKE experiments on Co/Gd bilayers to measure the magnetization dynamics after laser excitation. Although the laser energy used here is not high enough to result in AOS, simple de- and remagnetization dynamics can also give information on the thermal conductivity. We use a mode-locked Ti:Sapphire laser to generate laser pulses with a duration of approximately 150 fs at a repetition rate of 80 MHz The pulses have a central wavelength of 780 nm, at which we are dominantly sensitive to the Co magnetization.

In figure A.2 we plot the fully normalized results on both the Si:B and the Si/SiO$_2$ substrate. Note that the maximum demagnetization on both sublattices is not equal, and the raw data is plotted in the inset. There, the relative magnetization loss is extracted using magnetic hysteresis measurements. In the main figure, we observe rapid demagnetization and subsequent remagnetization on a short timescale (< 5 ps). Already at this timescale, a difference is present between the two substrates. Here it should be noted that, as seen in the inset, demagnetization on the Si/SiO$_2$ substrate was lower. This leads to faster magnetic dynamics than on the Si:B substrate,[55] as is observed in the behavior below ~ 4 ps. After this time a relative slowing down of the dynamics on the Si/SiO$_2$ substrate is found. This indicates a clear effect of the thermal conduc-

tivity of these substrates on the ultra-short timescale, which is relevant for repeated switching events. For longer timescales, the difference in behavior becomes even more pronounced. Although the timescale for full recovery of the magnetization is quite long (>500 ps), we emphasize that this is not the critical condition for allowing a second switching event. Instead, this depends on a number of factors such as the Co and Gd magnetization, their ratio, and the remaining temperature in the electron and phonon systems. However, the relatively slow recovery will be of interest in moving to many repeated writing events, as accumulated heat will most likely prove detrimental in that case.

Appendix B

SUPPLEMENTARY INFORMATION FOR CHAPTER 5

B.1   ADDITIONAL EXPERIMENTAL DETAILS

In our samples, the Gd and Tb layers were deposited while moving a shutter over the sample, leading to a thickness gradient along the sample. In order to determine the absolute thickness on this wedge an additional marker layer of Pt was deposited while keeping the shutter at the starting point of the path followed in the previous step. The reflectivity of the sample as a function of position then exhibits a step where this marker layer starts, giving a calibration point for the gradient. Due to shadowing effects the width of the step in this measurement is ~0.3 mm, which corresponds to 0.3 nm of RE thickness. Also due to imperfections in the positioning of the shutter, the exact starting point of the gradient can not be determined with greater accuracy than this 0.3 nm. Within this range, we define 0 nm as the final measurement point along the sample before the behavior of the FMR or THz mode begins to change. Note that the length of the gradient can be accurately determined, and the relative variation in thickness is accurate to within a few percent.

To accurately determine the exact moment of excitation, the so-called coherence peak is used,[146] which is centered around the temporal pump-probe overlap. This is a non-magnetic effect, so it can be measured by measuring the demagnetization after saturation in opposite directions. Adding the two curves leaves only the non-magnetic effects that are independent of the magnetization direction, which in our case is only the coherence peak. Using this technique, the moment of excitation can be determined with an uncertainty in the order of 10 fs, necessary for phase measurements of the THz spin waves. A more detailed description of the measurements, as well as an example, can be found in ref. 110.

B.2   TRANSFER MATRIX CALCULATIONS FOR OPTICAL ABSORPTION

In figure 5.4a we show the amplitude of the FMR mode for Gd thicknesses in the generation layer of up to 10 nm. At these thicknesses the optical absorption starts to play a significant role, and needs to be taken into account when determining the actual amplitude. As the film thickness increases, the absorbed laser energy also increases. Therefore heating and thus demagnetization is greater for thicker Gd layers, potentially generating stronger spin currents. To calculate the size of this effect, we perform trans-
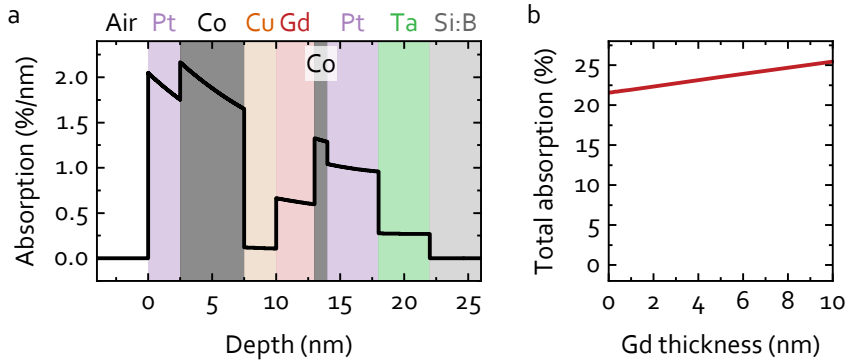
Figure B.1: (a) Instantaneous light absorption profile calculated with transfer matrix method for a Si:B(substrate)/Ta(4)/Pt(4)/Co(1)/Gd(3)/Cu(2.5)/Co(5)/Pt(2.5) stack. (b) Total absorption in the metallic layers as a function of the Gd thickness.

fer matrix calculations[147] using the *tmm* Python package.[162] Values for the refractive indices at the central laser wavelength (780 nm) are taken from literature.[178,179]

We calculate the instantaneous absorption profile for the metallic stack used in the experiments (with t_{Gd} = 3 nm), which we plot in figure B.1a. In metallic layers with thicknesses of only a few tens of nm, thermal equilibration between the layers proceeds on the timescale of mere hundreds of fs.[125] As this is comparable to the demagnetization timescale in Co, and much shorter than this timescale in Gd,[55] the absorption in the entire metallic stack is the relevant parameter to determine the ultimate magnetization quenching. Integrating the absorption profile over the thickness of the metallic layers then gives this total absorption. Repeating this for the range of Gd thicknesses used in the main work gives the curve shown in figure B.1b. Here we indeed find an increase of the absorption with the Gd thickness. To finally arrive at the data shown in figure 5.4a, the measured amplitude of the FMR spin-waves is divided by the total absorption for each value of the Gd thickness.

B.3   DERIVATION OF THE PHASE AND AMPLITUDE OF TOY MODEL FMR MODE

In section 5.3.1, we explain the Gd thickness dependence of the FMR amplitude and phase by decomposing the total FMR signal into a separate Co and Gd contribution, each with its own respective amplitude (A_{Co} and $A_{Gd}^{\dagger} = A_{Gd}(1 - \exp(-t/\lambda_{mag}))$) and phase (0 and δ). Using Euler's formula, this can be written as:

$$A_{FMR}e^{i(\omega t+\varphi)} = A_{Co}e^{i\omega t} + A_{Gd}^{\dagger}e^{i(\omega t+\delta)}. \tag{B.1}$$

As the frequency ω is assumed to be the same for all contributions, we can multiply equation (B.1) with $e^{-i\omega t}$, yielding:

$$A_{FMR}e^{i\varphi} = A_{Co} + A_{Gd}^{\dagger}e^{i\delta}. \tag{B.2}$$

First, we find an expression for A_{FMR} by taking the complex absolute value of equation (B.2).

$$A_{FMR} = \sqrt{|A_{Co} + A_{Gd}^{\dagger}e^{i\delta}|^2}$$
$$= \sqrt{A_{Co}{}^2 + A_{Gd}{}^2\left(1 - e^{-\frac{t}{\lambda_{mag}}}\right)^2 + 2A_{Co}A_{Gd}\cos(\delta)\left(1 - e^{-\frac{t}{\lambda_{mag}}}\right)}. \tag{B.3}$$

Next, an equation for the phase of the FMR mode is derived by taking the real and imaginary part of equation (B.2):

$$\left.\begin{array}{l} A_{FMR} = \dfrac{A_{Co} + A_{Gd}^{\dagger}\cos\delta}{\cos\varphi} \\[3mm] A_{FMR} = \dfrac{A_{Gd}^{\dagger}\sin\delta}{\sin\varphi}, \end{array}\right\} \quad \varphi = \tan^{-1}\left(\dfrac{\sin(\delta)A_{Gd}\left(1 - e^{-\frac{t}{\lambda_{mag}}}\right)}{A_{Co} + \cos(\delta)A_{Gd}\left(1 - e^{-\frac{t}{\lambda_{mag}}}\right)}\right). \tag{B.4}$$

Equations (B.3) and (B.4) are used to describe the data presented in figure 5.4a.
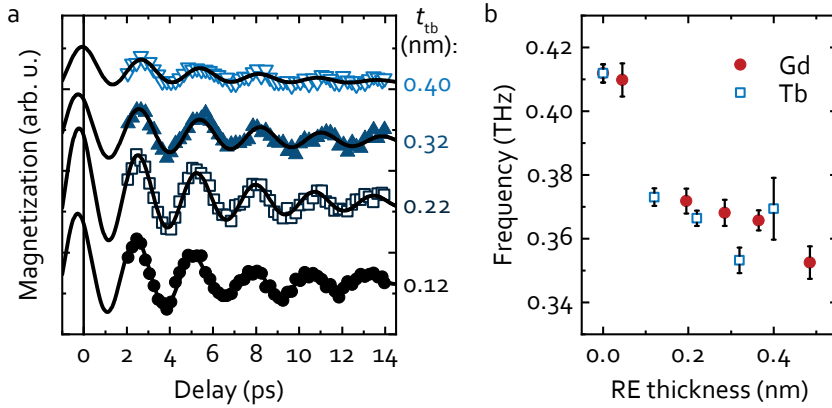
Figure B.2: (a) Spin wave measurements for the Co/Tb generation layer. (b) Extracted frequency as a function of Tb and Gd thickness. Data for Gd on a similar sample are included for comparison.

B.4 THz spin-waves excited by Co/Tb

THz spin-wave measurements are performed for the Co/Tb generation layers as well, as presented in figure B.2a. Due to strong attenuation of the measured signal for added Tb, only Tb thicknesses of up to 0.4 nm can be reliably considered. A decrease of the spin-wave frequency for increasing Tb thickness is observed (figure B.2b), similar to our observation for Gd, presented in section 5.3.2. We should note that these measurements were performed under slightly different growth conditions, leading to a slightly different absorption-layer thickness and thus a different spin-wave frequency. To be able to compare Gd and Tb, we performed the same experiments for a sample containing Gd, grown under the same conditions. As can be seen in figure B.2b, the frequency does not depend on the RE material, indicating that THz spin-wave generation is dominated by the Co. Furthermore, the observed frequency differences between identical samples gives us a strong indication that the observed anomalous frequency behavior is related to growth.

B.5   S-D MODELLING

B.5.1   THE DESCRIPTION OF THE MAGNETIC STACK

As mentioned in section 5.4, the generation layer is described as a system of layered CoGd alloys with a varying local Co concentration describing an intermixed Co/Gd bilayer.[133] Furthermore, this Co/Gd bilayer is connected to a Cu spacer layer of $d = 2.5$nm. We define the interface between the generation layer and the spacer layer as $z = 0$, where z represents the out-of-plane spatial coordinate. Now the local concentration of Co at position z is modeled by the function

$$x_{Co} = \frac{1}{2}\left[1 - \mathrm{erf}\big((z - z_{int})/w\big)\right], \tag{B.5}$$

where z_{int} is the position of the the (intermixed) Co/Gd interface. We set $w = 0.5$ nm. This yields an intermixing region with a width in the order of nanometers, an order of magnitude larger than the discretization step size (lattice spacing a).

Due to the intermixing region the layer thicknesses are not well defined. We define $\tilde{d}_{Gd} = z_{int} + a$, where a is the lattice constant. $\tilde{d}_{Gd}$ determines the total Gd in the system and plays the role analogue to a layer thickness. The total thickness of the system is then given $d = d_{Co} + \tilde{d}_{Gd}$, where $\tilde{d}_{Co} = 1$ nm is set constant and plays a the role of a thickness for the Co. To be clear, using this approach d_{Co} and $\tilde{d}_{Gd}$ do not precisely define a layer thickness, since we assume an intermixed interface. Nevertheless, for increasing value of $\tilde{d}_{Gd}$ the relative amount of Gd increases in an monotonuous way.

B.5.2   THE CALCULATION OF THE PHASE

To calculate the phase of the excited homogeneous precession in the absorption layer, we write down the Landau-Lifshitz-Gilbert-Slonzcewski equation for a homogeneous magnetization in the form[180]

$$\frac{d\mathbf{m}}{dt} = -\omega_o \mathbf{m} \times \hat{z} + \alpha \mathbf{m} \times \frac{d\mathbf{m}}{dt} + \boldsymbol{\tau}_{STT}, \tag{B.6}$$

where ω_o is the angular FMR frequency and α the effective Gilbert damping. $\boldsymbol{\tau}_{STT}$ is the (anti-damping) spin-transfer torque exerted by the absorbed spin current. The latter is

proportional to[180]

$$\tau_{\mathbf{STT}} \propto \mathbf{m} \times (j_s(t)\hat{x} \times \mathbf{m}). \tag{B.7}$$

We focus on small perturbations around the ground state $\mathbf{m} = \hat{z}$, assuming small transverse components in the x (OOP direction) and y direction $\delta m_x, \delta m_y \ll 1$. Furthermore, we define $\psi = \delta m_x + i\delta m_y$. Equations (B.6) and (B.7) then reduce to

$$-i(1 - i\alpha)\frac{d\psi}{dt} = \omega_0\psi - i\tau_{\mathrm{STT},x}(t), \tag{B.8}$$

which can easily be solved using the Green's function method. Assuming $|\alpha|^2 \ll 1$, we have the Green's function

$$G_0(t - t') \propto \vartheta(t - t')\exp(i\omega_0(1 + i\alpha)(t - t')). \tag{B.9}$$

The transverse magnetization is expressed in terms of a convolution

$$\delta m_x(t) \propto \mathrm{Re}\Big\{G_0 * j_s\Big\}. \tag{B.10}$$

Equation (B.10) is used to determine the phase of the homogeneous precession excited by $j_s(t)$ as calculated by the method in the previous section.

Extending the model to include the excited inhomogeneous modes can be accomplished by taking the following steps. The first step is to make the normalized magnetization $\mathbf{m}$ spatial dependent. The second step is to implement the exchange field in equation (B.6), which is of the form $\mathbf{H}_{\mathrm{ex}} \propto A\nabla^2\mathbf{m}$ with A the spin-wave stiffness.[109] In analogy with equation (B.8), the resulting equation of motion can be expressed in terms of the complex function $\psi(x, t)$, which is now dependent on spatial coordinate x. Importantly, it is assumed that all incoming (perpendicular) spins are absorbed at the interface. Now, the spin-transfer torque will appear as a boundary condition for the function $\psi(x, t)$. Finally, the function $\psi(x, t)$ is expanded in cosines $\cos(n\pi x/L)$ that represent the standing spin-wave solutions. In that way, an equation for every separate mode can be derived. It is straightforward to show that the contribution $\delta m_{x,n}$ of mode n to the amplitude of the transverse magnetization is equivalently determined by

$$\delta m_{x,n}(t) \propto \mathrm{Re}\Big\{G_n * j_s\Big\}, \tag{B.11}$$

with the response function $G_n(t)$ for mode n

$$G_n(t - t') \propto \vartheta(t - t')\exp(i\omega_n(1 + i\alpha_n)(t - t')), \tag{B.12}$$

where ω_n is the frequency of mode n and given by $\omega_n = \omega_0 + (A/\hbar)(n\pi/L)^2$ with L the thickness of the absorption layer. Furthermore, α_n is the mode-dependent damping parameter. For simplicity, the latter is assumed to be independent of the mode and set equal to the Gilbert damping.

B.5.3   SYSTEM PARAMETERS

The values of the material parameters as used in the calculations presented in section 5.4 are given in table B.1. We stress that although we use the terminology of Co/Gd components in the text, the material parameters presented here correspond to the values for a general TM-RE system. The latter is motivated by that the modeling only justifies qualitative statements, since the implementation required a large number of assumptions and approximations.

Table B.1: The typical values used for the material parameters in the calculation of section .. .

symbol	meaning	value
T_{amb}	ambient temperature	295 K
γ	electronic heat capacity parameter	$2000\ \mathrm{J\,m^{-3}\,K^{-2}}$
C_p	phonon heat capacity	$4 \cdot 10^6\ \mathrm{J\,m^{-3}\,K^{-1}}$
P_o	absorbed pulse energy	$2 \cdot 10^8\ \mathrm{J\,m^{-3}}$
σ	pulse duration	0.15 ps
τ_D *	heat dissipation time scale	100 ps
a	lattice spacing	0.25 nm
$T_{C,\mathrm{TM}}$	TM Curie temperature	1000 K
$T_{C,\mathrm{RE}}$	RE Curie temperature	292 K
S_{TM}	spin quantum number	1/2
S_{RE}	spin quantum number	7/2
$\mu_{at,\mathrm{TM}}$	TM atomic magnetic moment	2.0 μ_B
$\mu_{at,\mathrm{RE}}$	RE atomic magnetic moment	7.0 μ_B
ρ_{sd}	s-d coefficient Ref.[101]	1.0 eV
$\tau_{sd,\mathrm{TM}}$	TM s-d scattering time	0.1 ps
$\tau_{sd,\mathrm{RE}}$	RE s-d scattering time	20.0 ps
τ_s	spin-flip scattering time (magnetic region)	0.2 ps
$\tau_{s,N}$	spin-flip scattering time (nonmagnetic region)[145]	17 ps
σ	conductivity (magnetic region)[145]	$6.7 \cdot 10^6\ \mathrm{S\,m^{-1}}$
σ_N	conductivity (spacer layer)[145]	$39 \cdot 10^6\ \mathrm{S\,m^{-1}}$
D	spin diffusion coefficient (magnetic region)[145]	$250\ \mathrm{nm^2\,ps^{-1}}$
D_N	spin diffusion coefficient (spacer layer)[145]	$9500\ \mathrm{nm^2\,ps^{-1}}$
g	interfacial conductance parameter	$0.4 \cdot 10^6\ \mathrm{m^{-2}}$
$\omega_o/(2\pi)$	FMR frequency	12 GHz
α	effective damping	0.05
$j_{\mathrm{Co-Gd}}$	interatomic exchange constant	2.0 meV
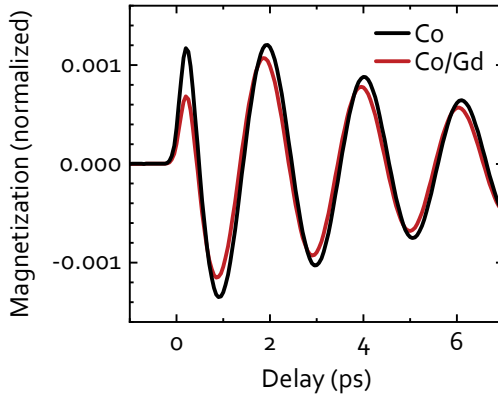
Figure B.3: Calculated THz mode excited by the spin cur- rent from a Co(1) (black) and Co(1)/Gd(2) (blue) generation layer.

B.6   MODELLING THZ SPIN WAVES USING THE S-D MODEL

Using the *s-d* framework discussed in Sec. IV of this, the THz response of the absorption layer is calculated. The results are plotted in figure B.3 for Co(1) (black line) and Co(1)/Gd(2) (red line).

Our calculations indicate a slight decrease of the amplitude, which in experiments we expect to be more pronounced due to spin diffusion in the Gd layer. Furthermore, a slight phase shift is expected. The calculated shift is in the order of 60 fs, which corresponds to a phase shift of about 10°. This is too small to pick up in our measurements.

B.7 POTENTIAL EXPLANATIONS FOR THE THz SPIN-WAVE FREQUENCY SHIFT

B.7.1 GROWTH RELATED FREQUENCY SHIFT

A growth-related change in the exchange stiffness scales linearly with the spin-wave frequency.[181] Eyrich *et al.* demonstrated that the effective exchange stiffness of ultrathin (< 10 nm) Co can drop significantly when alloyed with certain non-magnetic materials,[148] and similar effects were later reported in Cu/Co bilayers due to intermixing at the interface.[109] We postulate that due to the addition of a RE dusting below the Cu, subsequent growth becomes more disordered, leading to more intermixing and thus a lower exchange stiffness. Although we expect the ~45% reduction of the exchange stiffness required to explain the observed frequency shift completely is improbably large,[109,148] the order of magnitude of this effect is unknown for our system specifically and requires further research.

B.7.2 INTERLAYER COUPLING BETWEEN TWO EIGENMODES

We postulate that the frequency is significantly affected by the interlayer coupling of the simultaneous transverse magnetization dynamics in the generation layer and absorption layer. This coupling arises from the combination of spin pumping, interlayer spin transport, and the resulting spin-transfer torques. It will be maximized in case the eigenmodes of the absorption layer (the standing spin waves) and the eigenmodes of the generation layer (e.g., the exchange mode of the synthetic-ferrimagnetic multilayer) have a similar frequency.

In order to reach a mathematical description of this concept, we formulate an expression of the form of equation (B.6) for both layers separately. The noncollinear nature of the full magnetic stack is captured in the definitions of the effective fields within the distinct layers. In analogy with the previous subsection, the effective field within the absorption is pointing along the z axis, and its magnitude is expressed in terms of the eigenfrequency ω_A. For the generation layer, we define the effective field to be directed along the positive x direction, with a magnitude determined by ω_G. Additionally, we include the interlayer coupling terms. Specifically, the equation for the absorption layer

includes the torque[180]

$$\boldsymbol{\tau}_{\text{interlayer–STT}} \propto g_A \, \mathbf{m}_A \times \left(\left(\mathbf{m}_G \times \frac{d\mathbf{m}_G}{dt}\right) \times \mathbf{m}_A\right),$$ (B.13)

where $\mathbf{m}_A$ describes the normalized magnetization of the absorption layer and $\mathbf{m}_G$ the normalized magnetization of the generation layer. Furthermore, the dimensionless factor g_A is determined by the efficiency of spin pumping and the interlayer spin transfer, and mainly depends on the spin-mixing conductances. The expression describes an anti-damping spin-transfer torque mediated by the pumped spin current from the generation layer. A similar torque will be present in the equation for the magnetization dynamics in the generation layer, where the subscripts are interchanged $A \leftrightarrow G$. We linearize the set of equations using $\mathbf{m}_A = (\delta m_{A,x}, \delta m_{A,y}, 1)$ and $\mathbf{m}_G = (1, \delta m_{G,y}, \delta m_{G,z})$. By collecting the linear terms, and switching to the frequency domain, we find the following equation for the eigenfrequency ω

$$((\omega_A + i\alpha_A\omega)^2 - \omega^2)((\omega_G + i\alpha_G\omega)^2 - \omega^2) - g_A g_G \omega^2 (\omega_A + i\alpha_A \omega)(\omega_G + i\alpha_G \omega) = 0, \quad \text{(B.14)}$$

where α_A and α_G are the effective damping for the layer-specific eigenmodes. To purely extract the role of the effect discussed in this subsection, we remove the terms dependent on the damping $\alpha_A = \alpha_G \to 0$. By solving equation (B.14), it can be shown that the maximal shift of the frequency (compared to the layer-specific eigenfrequencies ω_A and ω_G) is reached in case the eigenfrequencies are equal $\omega_A = \omega_G \equiv \omega_0$. Then, the frequency is given by

$$\omega = \omega_0 \sqrt{1 + \frac{g_A g_G}{2} \pm \sqrt{g_A g_G}\sqrt{1 + \frac{g_A g_G}{4}}}.$$ (B.15)

For $\sqrt{g_A g_G} \ll 1$ this expression is equivalent to

$$\omega = \omega_0 \left(1 \pm \sqrt{g_A g_G}/2\right),$$ (B.16)

indicating that the change is linear in $\sqrt{g_A g_G}$.

Considering that the factors g_A and g_G are related to the effective damping (which for ultrathin films is strongly enhanced by spin pumping), using an effective damping of $\alpha = 0.1$ we estimate that the reduction of the frequency resulting from this effect is approximately 5 %. Considering that the (not investigated) eigenmode of the ferrimagnetic generation layer may have a stronger damping, higher values for the frequency shift may be possible. Although this mechanism can not explain the large frequency

reduction as observed in the experiments, the order of magnitude of this results proofs that this contribution is nonnegligible.

Appendix C

SUPPLEMENTARY INFORMATION FOR CHAPTER 6
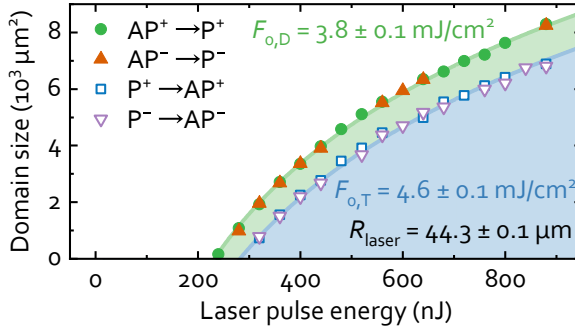
Figure C.1: Switched domain size extracted from Kerr microscopy images after irradiation of a $(Co/Ni)_{x4}/Co/Cu/Co/Gd$ sample with a ~100 fs laser pulse as a function of laser pulse energy. Fits are made to extract the threshold fluence, where each pair (P^+ and P^-, AP^+ and AP^-) is fitted simultaneously.

C.1 AOS THRESHOLD FLUENCES FOR ALL INITIAL STATES

In figure 6.2a we presented a measurement where we determined the threshold fluence for switching from the AP to the P state ($F_{o,D}$) and vice versa ($F_{o,T}$). For the sake of simplicity, we only showed data from measurements where the reference layer magnetization was in the positive direction out of the sample plane (plus-states). We assumed that, as the corresponding plus- and minus-states are time reversed versions of each other, only the relative orientation of the reference layer and free layer (P or AP) determines whether the spin current from the reference layer assists or hinders switching. Here we verify this assumption by determining the threshold fluence for switching when starting from all four possible magnetization states (P^+, AP^+, AP^-, and P^-).

In figure C.1 we present the switched domain size in a $(Co/Ni)_{x4}/Co/Cu/Co/Gd$ sample as a function of incident laser pulse energy, when starting from all four states. The domain sizes indeed do not depend on the sample starting in a plus- or a minus-state, confirming as expected that only the relative orientation of the reference and free layer is relevant. Note that these measurements were performed on a different sample than those in Fig. 1(c), yielding different values for the threshold fluence but showing the same qualitative behaviour.
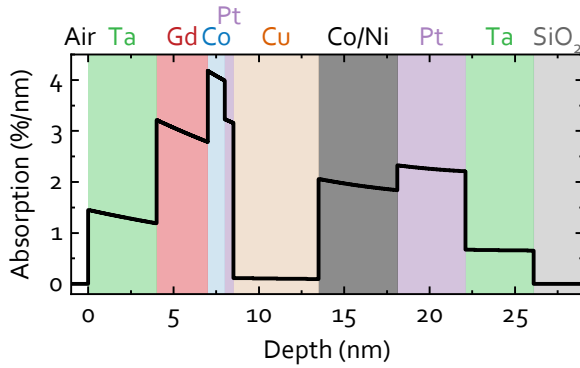
Figure C.2: Optical absorption per unit depth of a $SiO_2(100)/Ta(4)/Pt(4)/(Co(0.2)/Ni(0.9))_{x4}/Co(0.2)/Cu(5)/Pt(0.5)/Co(1)/Gd(3)/Ta(4)$ sample as used in this work (numbers between parentheses indicate thicknesses in nm). Note that the full SiO_2 layer and Si:B substrate are included in the calculation itself.

C.2 CALCULATED OPTICAL ABSORPTION IN SAMPLES

For the analysis presented in figure 6.4b, we calculated the theoretical optical absorption in the Co/Ni reference layer. As mentioned, this was done using a transfer matrix method. In this section we briefly expand on the process that was used. Using known values of the refractive index at 700 nm for all materials in the stack (from both our own measurements and literature[178]), we calculate an absorption profile of the entire stack, as shown in figure C.2. Note that due to the likely high degree of intermixing, we treat the full Co/Ni multilayer as having the refractive index of the dominant material by volume, being Ni. The absorption in this multilayer is subsequently calculated by integrating over the thickness of this layer.

In the same discussion we mentioned that the threshold fluences $F_{0,D}$ and $F_{0,T}$ were found to increase with increasing Ni thickness in the reference layer. To explain this, we posited that this could be partially explained by a difference in optical absorption in the Co/Gd layer. As the SiO_2 layer on our substrates acts as a reflective coating, the absorption is strongly affected by this reflection. Therefore, an increase in absorption in lower layers with increasing thickness could lead to a sizeable reduction of the absorption in the upper layers. To verify this, we calculated the absorption in the Co/Gd bilayer as a function of Ni thickness. We find that upon increasing the Ni thickness in each repeat from 0.5 to 1.0 nm, the optical absorption in the Co/Gd bilayer decreases by approximately 12 %. At the same time, the threshold fluences increase by ~ 19% in
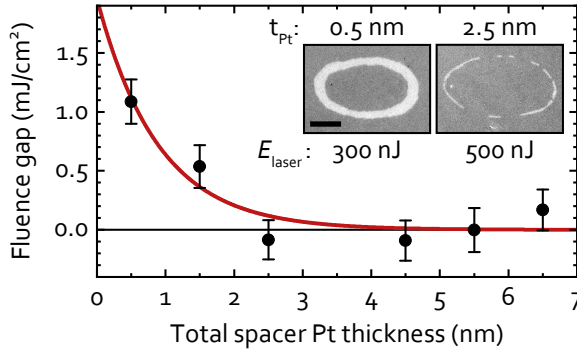
Figure C.3: Difference between threshold fluences for deterministic writing and toggle switching as a function of the total Pt thickness between the reference and free layer in a $SiO_2(100)/Ta(4)/Pt(4)/(Co(0.2)/Ni(0.9))_{x4}/Co(0.2)/Pt(X-0.5)/Cu(5)/Pt(0.5)/Co(1)/Gd(3)/Ta(4)$ sample. Line indicates a fit with an exponentially decaying function. Inset shows a two pulse experiment similar to figure 6.4a for two different Pt thicknesses in the spacer layer. Scale bar represents 20 µm Error bars represent the standard deviation obtained through fitting.

this same interval. The increase in threshold fluence can therefore to a large extent be attributed to the reduction in optical absorption in the Co/Gd bilayer. As mentioned in section 6.3, a higher roughness of the top layers could explain the additional increase, which could be verified by investigating the inverted stack (where the reference and free layer switch position).

C.3   Blocking spin transfer with a spin sink

In section 6.3 we showed that the difference between threshold fluences can quantitatively be explained by the behaviour of an optically generated spin current by tuning the reference layer. As a less quantitative, but more straightforward check that the effect is driven by a spin current we show a different approach here.

Following Iihama et al.,[111] in figure C.3 we present results of an experiment where we determine the difference between the two threshold fluences as a function of the thickness of a Pt insert layer between the reference layer and free layer. Note that we plot the total Pt thickness in the spacer, as a 0.5 nm Pt buffer layer on top of Cu is always included to induce PMA in the Co/Gd bilayer. It is clear here that the threshold fluence gap goes to zero within ~2.5 nm of total Pt thickness. From a fit of the data with an exponentially decaying function (solid line) we extract a characteristic decay length, the

Pt spin diffusion length, of (0.9 ± 0.3) nm, which is consistent with literature reports.[182] This is also demonstrated in the inset of figure C.3, where we show Kerr microscopy images of the same two pulse experiment shown in figure 6.4a. There, we exposed a sample prepared in the AP state to two subsequent laser pulses with the same energy. We have already seen that this results in a ring-shaped region where the second pulse does not switch the free layer again, due to the difference in threshold fluences. Here we additionally perform this experiment on a sample with an added Pt layer of 2 nm between the reference layer and the Cu spacer layer. It can be seen that no clear ring appears, as is to be expected when there is no difference in threshold fluences. The slight broken ring which remains is the result of pulse-to-pulse variations of the laser, as this same ring is also present when performing the experiment on a sample which is prepared in the P state. This same variation between pulses is also the main cause of the relatively large error bar, as well as the apparent zero crossing and subsequent rise of the fluence gap in these measurements.

C.4   Distinguishing between states in Kerr microscopy

The different contrast levels in the Kerr microscopy images in this work have thus far been labelled as different magnetization configurations. In this section we show how we determine which contrast level corresponds to which magnetization state.

In figure C.4a we show Kerr microscopy images of a sample that has been prepared in the AP$^+$ state which has been exposed to a train of laser pulses (left, green border) and a single laser pulse (right, blue border). After exposure with a train of laser pulses, a complex multidomain magnetization state appears due to excessive heating of the sample. The energy of the laser pulses used here was high enough that both the reference and free layer have been thermally demagnetized by the pulse train. Therefore both states of both layers, and consequently all four possible magnetization configurations, are present in this area. This can be seen directly in the four different contrast levels that can be distinguished. In the case of exposure with a single laser pulse, only two total contrast levels are present.

In figure C.4b we present histogram data of the gray values of all pixels in both images of figure C.4b, after application of a slight Gaussian blur to reduce noise. Here, gray values of 0 and 255 are black and white, respectively. In the area that has been exposed to a train of laser pulses, four peaks in gray value are indeed present, which correspond with the four possible magnetization states. Conversely, for exposure with
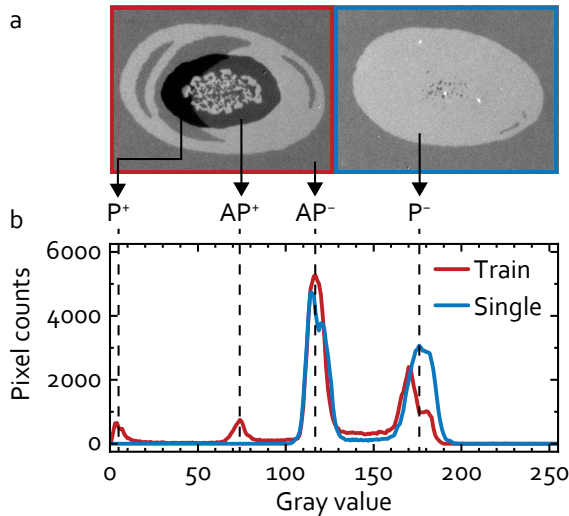
Figure C.4: (a) Kerr microscopy images of a typical $(Co/Ni)_{x4}$/Co/Cu/Co/Gd sample that has been exposed to a train of fs laser pulses (left) and a single laser pulse (right). (b) Histogram data of the gray values of each pixel in blurred versions of the images in (a). Four distinct contrast levels are observed and labelled with their corresponding magnetization states.

a single pulse only two peaks are present. We can now match the four contrast levels with their magnetization states by making use of the MOKE hysteresis loop presented in figure 6.1a. As mentioned previously, the sample has been prepared in the AP^+ state. This contrast level has the largest area, and therefore corresponds to the highest peak in figure C.4b, or the second highest gray value. Second, the P states have the highest total Kerr rotation, and are therefore represented by the darkest and lightest levels. The settings of the Kerr microscope were chosen such that lighter contrast corresponds to higher positive Kerr rotation, which means the lightest (darkest) contrast level corresponds to the P^+ (P^-) state. The final remaining state, which has the second lowest gray value, is then the AP^- state.

Here it is also clear that after a single pulse, only the free layer switches. When starting from a plus state, the appearance of a minus state is found only to occur after exposure to a train of laser pulses or a single laser pulse with high energy, both of which can lead to demagnetization of the reference layer. We note that the differences in gray value between the states do not precisely match with the steps found in the MOKE hysteresis loop. This is likely due to the use of white light in Kerr microscopy, as opposed to red

laser light (632 nm) in the MOKE measurements, leading to different penetration depths and relative sensitivities to each of the magnetic layers.

SUMMARY

The work described in this thesis concerns the excitation of magnetic material stacks with femtosecond (fs) laser pulses. The study of the dynamics arising from such excitation is commonly referred to as femtomagnetism. This field was kickstarted in 1996 with the discovery of sub-picosecond magnetization quenching in a ferromagnetic film after fs pulsed laser excitation. In later years it was revealed that mobile spin polarized electrons (spin currents) could be excited during such a demagnetization process, acting as carriers of spin angular momentum.

The field was shaken up in 2007 with the surprising demonstration of full magnetization reversal in a ferrimagnetic rare earth-transition metal (GdFeCo) alloy with a single fs laser pulse (all-optical switching or AOS). Later research demonstrated that AOS occurs via a symmetric toggle mechanism, and that the switch itself takes place on a picosecond timescale. The potential of this phenomenon for writing data in magnetic storage media in a non-dissipative and ultrafast manner was soon realized, and has driven research to this day. In particular, synthetic ferrimagnetic systems have proven to be promising candidates for integration in future hybrid photonic data storage devices.

Although subsequent research in the field of femtomagnetism has led to major new insights, several quandaries relevant for both fundamental physical understanding and future applications remain. In this thesis we shed new light on this field, by investigating both AOS and optically generated spin currents, as well as novel combinations of the two.

In the first research chapter we investigate the ultimate repetition rates at which AOS can take place. By exciting a synthetic ferrimagnet with two fs laser pulses separated by several picoseconds, we deduce the minimum time needed to consistently observe two switching events. Using specially engineered layered ferrimagnetic systems as well as careful tuning of heat conduction and laser pulse energy, we find a minimum timescale

of only 10 ps. This is in line with recent research on ferrimagnetic alloys, cementing the viability of synthetic ferrimagnets for AOS.

In the second research chapter we examine optically generated spin currents in all-optically switchable materials. Using collective magnetic excitations (spin waves) excited by the spin current generated in an adjacent layer, we are able to deduce characteristics of this spin current. We perform this experiment both for all-optically switchable Co/Gd systems as well as Co/Tb systems, which do not show AOS. We find a significant contribution to the spin current from both Co and Gd, but not from Tb, hinting at a reason for the lack of AOS in Tb-containing systems.

In the subsequent chapter we fully combine AOS and optical spin current generation to achieve novel device functionality. Here we show that spin currents excited in a magnetic reference layer can hinder or assist AOS in an adjacent synthetic ferrimagnet depending on their spin polarization. We demonstrate that this symmetry breaking can be used to deterministically write a desired magnetization state with no knowledge of the initial state.

We present an outlook on further research in the final chapter. Here we investigate synthetic ferrimagnets containing both Gd and Tb, the latter of which has a high intrinsic anisotropy. This leads to the possibility to stabilize sub-micron domains, whereas the addition of Gd enables all-optical switching. Furthermore we investigate the time-resolved dynamics of AOS in the presence of an external spin current with both experiments and modeling, providing valuable new insights into this process. The chapter concludes with a general outlook on the technological applications of the work presented in this thesis.

The results in this thesis add to the growing body of knowledge in the field of femtomagnetism that could, together with integrated photonics, provide unprecedented speed and energy efficiency to the digital data storage and processing devices of the future.

CURRICULUM VITAE

Youri Louis Winandus van Hees was born on December 21, 1994 in Geleen, the Netherlands. He attended high school at Graaf Huyn College in Geleen, and graduated in 2012. Subsequently he studied Applied Physics at Eindhoven University of Technology, and obtained his Bachelor of Science in 2015. His bachelor's project concerned photoluminescence spectroscopy of (Al)InGaP nanowires, and was performed in the group Photonics and Semiconductor Nanophysics.

Youri continued with the master's program in Applied Physics at Eindhoven University of Technology. During this program he interned in the Laboratory of Semiconductor Materials at École Polytechnique Fédérale in Lausanne, Switzerland. Under the supervision of dr. Heidi Potts he investigated the growth and characterization of non-vertical self-catalyzed InAs nanowires. His master's project was performed in the Physics of Nanostructures group, under the supervision of dr. ir. Reinoud Lavrijsen and dr. Jos van der Tol. Here he characterized and modeled magnetic claddings deposited on photonic waveguides for optical reading of data.

During his PhD project in the Physics of Nanostructures group Youri moved on to the study of ultrafast laser-induced magnetization dynamics, with a focus on all-optical switching and spin transport. The main results of this PhD project are presented in this thesis.

SCIENTIFIC OUTPUT

Publications

1. H. Potts, **Y.L.W. van Hees**, G. Tutuncuoglu, M. Friedl, J-B. Leran & A. Fontcuberta i Morral. Tilting catalyst-free InAs nanowires by 3D-twinning and unusual growth directions.
Crystal Growth & Design **17.7**, 3596-3605 (2017).

2. **Y.L.W. van Hees**, J.J.G.M. van der Tol, B. Koopmans & R. Lavrijsen. Periodically modulated ferromagnetic waveguide claddings with perpendicular magnetic anisotropy for enhanced mode conversion.
Proceedings of the 22nd Annual Symposium of the IEEE Photonics Society Benelux Chapter 196-199 (2017).

3. D-S. Han, K. Lee, J-P. Hanke, Y. Mokrousov, K-W. Kim, W. Yoo, **Y.L.W. van Hees**, T-W. Kim, R. Lavrijsen, C-Y. You, H.J.M. Swagten, M-H. Jung & M. Kläui. Long-range chiral exchange interaction in synthetic antiferromagnets.
Nature Materials **18.7**, 703-708 (2019).

4. L. Wang, **Y.L.W. van Hees**, R. Lavrijsen, W. Zhao & B. Koopmans. Enhanced all-optical switching and domain wall velocity in annealed synthetic-ferrimagnetic multilayers.
Applied Physics Letters **117.2**, 022408 (2020).

5. **Y.L.W. van Hees**, P. van de Meugheuvel, B. Koopmans & R. Lavrijsen. Deterministic all-optical magnetization writing facilitated by non-local transfer of spin angular momentum.
Nature Communications **11.1**, 1-7 (2020).

6. A. Cao, **Y.L.W. van Hees**, R. Lavrijsen, W. Zhao & B. Koopmans. Dynamics of all-optically switched magnetic domains in Co/Gd heterostructures with Dzyaloshinskii-Moriya interaction.
   Physical Review B **102.10**, 104412 (2020).

7. P. Li, M.J.G. Peeters, **Y.L.W. van Hees**, R. Lavrijsen & B. Koopmans. Ultra-low energy threshold engineering for all-optical switching of magnetization in dielectric-coated Co/Gd based synthetic-ferrimagnet.
   Applied Physics Letters **119.25**, 252402 (2021).

8. L. Wang, H. Cheng, P. Li, **Y.L.W. van Hees**, Y. Liu, K. Cao, R. Lavrijsen, X. Lin, B. Koopmans & W. Zhao. Picosecond optospintronic tunnel junctions.
   Proceedings of the National Academy of Science **119.24**, e2204732119 (2022).

9. **Y.L.W. van Hees**, B. Koopmans & R. Lavrijsen. Toward high all-optical data writing rates in synthetic ferrimagnets.
   Applied Physics Letters **120**, 252401 (2022).

10. T. Lichtenberg[†], **Y.L.W. van Hees**[†], M. Beens, C.J. Levels, R. Lavrijsen, R.A. Duine & B. Koopmans. Probing laser-induced spin-current generation in synthetic ferrimagnets using spin waves.
    Physical Review B **106**, 094436 (2022)
    [†]*These authors contributed equally.*

11. Z. Wang, P. Li, Y. Yao, **Y.L.W. van Hees**, C.F. Schippers, R. Lavrijsen, A. Fert, W. Zhao & B. Koopmans. Field-free spin orbit torque switching of synthetic antiferromagnet through interlayer Dzyaloshinskii-Moriya interaction.
    Submitted.

Conference presentations

1. Ultimate speed limits for deterministic all-optical toggle switching.
   64th Annual Conference on Magnetism and Magnetic Materials (2019).

2. Selective all-optical toggle switching defined by spin currents in FM/Cu/Co/Gd systems.
   64th Annual Conference on Magnetism and Magnetic Materials (2019).

3. Deterministic writing of magnetization via spin current-assisted all-optical switching.
   Physics@Veldhoven (2020).

4. Spin-current-enhanced all-optical switching in synthetic ferrimagnets.
   MAGNETOFON General Action Meeting and Workshop (2020).

5. Deterministic all-optical magnetization writing driven by spin currents.
   Joint European Magnetism Symposia (2020).

6. Using spin waves to probe ultrafast spin current generation in rare earth ferromagnets.
   15th Joint MMM-Intermag Conference (2022).

7. Enhancing all-optical magnetization writing with spin currents.
   15th Joint MMM-Intermag Conference (2022).

ACKNOWLEDGEMENTS

And so we come to the end of this thesis. It goes without saying that no PhD project can succeed without the help of many people, both on a scientific and a personal front. Therefore I would now like to thank some of the people who have been instrumental in making this project a success.

Als eerste wil ik mijn twee promotoren en dagelijkse begeleiders bedanken, die allebei altijd klaar stonden met een behulpzaam woord of een luisterend oor. **Bert**, jouw scherpe fysische blik en creatieve denkvermogen hebben mij regelmatig geholpen om meer uit mijn onderzoek te halen dan ik zelf voor mogelijk hield. Vooral jouw inzet om het overzicht te houden en het grotere plaatje niet uit het oog te verliezen wordt zeer gewaardeerd. **Reinoud**, het enthousiasme dat jij dagelijks tentoonstelt voor onderzoek en het overdragen van kennis is aanstekelijk. Ook op de momenten waar het onderzoek wat moeizamer ging, wist jij mij te motiveren met je positive instelling, waarvoor dank.

I would also like to thank the other scientific staff members of FNA, **Henk**, **Diana**, and **Rembert** for valuable feedback during PhD meetings and discussions.

Next, I wish to express my gratitude to the members of my doctorate committee, **dr. Kees Flipse, prof. dr. Theo Rasing, prof. dr. Martin Weinelt**, and **dr. Gregory Malinowski**. Thank you for agreeing to take seat in my committee, and for taking the time to evaluate my work.

Geen enkele zichzelf respecterende onderzoeksgroep kan functioneren zonder ondersteunende staf. **Jeroen** en **Bart**, van harte bedankt voor jullie inzet om de labs draaiende te houden met hard werk en creatieve oplossingen. In het bijzonder bedankt voor het uitvoeren van de vele opgelegde target changes (waarvoor excuses). **Karin**, zonder jouw hulp om door de administratieve rompslomp te navigeren zou de bureaucratie op de universiteit haast ondraaglijk worden. Ook wil ik je bedanken voor het

organiseren van de vele sociale activiteiten om van de groep vooral ook een gezellige plek te maken.

Tijdens dit project heb ik de kans gehad om een aantal studenten te begeleiden bij hun bachelor- of masterprojecten. Om bij de eerste groep te beginnen wil ik de ex-bachelorstudenten **Paul**, **Gijs**, en **Cas** bedanken; het was een genoegen om jullie in een korte tijd te zien ontwikkelen tot beginnende wetenschappers met een eigen, kritische blik op onderzoek.

Vervolgens de masterstudenten, in chronologische volgorde. **Kenneth**, hoewel jouw werk geen expliciete plek heeft gekregen in deze thesis, is het wel essentieel geweest voor het beter begrijpen van de materialen die we onderzoeken. In die zin heeft het een groot deel van dit onderzoek mogelijk gemaakt, waarvoor dank. **Maarten P.**, al heb je bijzonder veel last gehad van bepaalde omstandigheden in 2020, toch heb je dankzij je doorzettingsvermogen interessante resultaten weten te behalen. Ik ben je dankbaar voor dit mooie werk, dat ook een plekje heeft gevonden in deze thesis (sectie 7.2). **Roy**, jouw creatieve maar toch georganiseerde aanpak heeft geleid tot uitvoerige resultaten over een volledig nieuw systeem (beschreven in sectie 7.1). Mijn dank voor de manier waarop je dit onderzoek in een relatief kort project succesvol hebt opgezet.

For making FNA a pleasant working enviroment, I would like to thank the current and former PhD students and postdocs of the group, **Adrien**, **Anni**, **Ece**, **Fanny**, **Floris**, **Hamed**, **Jianing**, **Julian**, **Lorenzo**, **Luding**, **Marcos**, **Mariia**, **Mark L.**, **Michał**, **Pingzhi**, **Tunç**, and **Zilu**. In het bijzonder wil ik **Juriaan**, **Marielle**, **Mark de J.**, **Mark P.**, **Thomas B.**, en **Thomas K.** bedanken voor de vele gezellige etentjes en andere activiteiten die we samen ondernomen hebben. **Maarten**, ook bedankt hiervoor, alsmede voor het gezelschap tijdens twee mooie reizen en bij het fitnessen.

Dan ben ik aanbeland bij mijn twee rotsen in de branding, mijn kantoorgenoten en goede vrienden, **Tom** en **Casper**. Het was een waar genoegen om met jullie vanaf onze masterprojecten een kantoor te delen. Voor de sfeer op kantoor en de manier waarop we altijd konden discussiëren, hardop nadenken, of gewoon zeuren, zal ik jullie altijd dankbaar zijn. Ook onze gezamenlijke reizen, concerten, en andere uitjes zal ik nooit vergeten; dat er nog veel mogen volgen!

Tenslotte wil ik nog een paar mensen buiten de academische wereld bedanken. **Tristan** en **Jasper**, bedankt voor jullie langdurige vriendschap, die hopelijk nog veel langer stand mag houden.

Pap en mam, **Lou** en **Thera**, bedankt voor de continue steun en aanmoediging. Ik weet dat jullie altijd voor me klaar staan, en ik hou van jullie.

REFERENCES

1. IOT ANALYTICS. State of IoT (2022). URL: iot-analytics.com/number-connected-iot-devices/.

2. D. REINSEL, J. RYDNING & J. F. GANTZ. Worldwide Global DataSphere Forecast, 2021–2025: The world keeps creating more data — now, what do we do with it all? *IDC Corporate USA* (2021). URL: www.idc.com/getdoc.jsp?containerId=US46410421.

3. N. JONES. How to stop data centres from gobbling up the world's electricity. *Nature* **561**, 163–167 (2018). DOI: 10.1038/d41586-018-06610-y.

4. A. SHEHABI ET AL. United States data center energy usage report. *Lawrence Berkeley National Laboratory* (2016). URL: eta.lbl.gov/publications/united-states-data-center-energy.

5. R. BLÄSING ET AL. Magnetic racetrack memory: From physics to the cusp of applications within a decade. *Proceedings of the IEEE* **108**, 1303–1321 (2020). DOI: 10.1109/JPROC.2020.2975719.

6. A. W. FANG ET AL. Electrically pumped hybrid AlGaInAs-silicon evanescent laser. *Optics Express* **14**, 9203–9210 (2006). DOI: 10.1364/OE.14.009203.

7. L. KIMERLING ET AL. Electronic-photonic integrated circuits on the CMOS platform. *Silicon Photonics* **6125**, 6–15 (2006). DOI: 10.1117/12.654455.

8. H. TAKAHASHI, S. SUZUKI, K. KATO & I. NISHI. Arrayed-waveguide grating for wavelength division multi/demultiplexer with nanometre resolution. *Electronics Letters* **26**, 87–88 (1990). DOI: 10.1049/el:19900058.

9. M. SMIT, K. WILLIAMS & J. VAN DER TOL. Past, present, and future of InP-based photonic integration. *APL Photonics* **4**, 050901 (2019). DOI: 10.1063/1.5087862.

10. J. YAO. Microwave photonics. *Journal of Lightwave Technology* **27**, 314–335 (2009). DOI: 10.1109/JLT.2008.2009551.

11. J. Hulme et al. Fully integrated hybrid silicon two dimensional beam scanner. *Optics Express* **23**, 5861–5874 (2015). DOI: 10.1364/OE.23.005861.

12. S. Fathololoumi et al. 1.6 Tbps silicon photonics integrated circuit and 800 Gbps photonic engine for switch co-packaging demonstration. *Journal of Lightwave Technology* **39**, 1155–1161 (2020). DOI: 10.1109/JLT.2020.3039218.

13. T. Komljenovic et al. Photonic integrated circuits using heterogeneous integration on silicon. *Proceedings of the IEEE* **106**, 2246–2257 (2018). DOI: 10.1109/JPROC.2018.2864668.

14. D. Liang & J. E. Bowers. Recent progress in heterogeneous III-V-on-silicon photonic integration. *Light: Advanced Manufacturing* **2**, 59–83 (2021). DOI: 10.37188/lam.2021.005.

15. C. D. Stanciu et al. All-optical magnetic recording with circularly polarized light. *Physical Review Letters* **99**, 047601 (2007). DOI: 10.1103/PhysRevLett.99.047601.

16. T. Ostler et al. Ultrafast heating as a sufficient stimulus for magnetization reversal in a ferrimagnet. *Nature Communications* **3**, 666 (2012). DOI: 10.1038/ncomms1666.

17. J. Gorchon et al. Role of electron and phonon temperatures in the helicity-independent all-optical switching of GdFeCo. *Physical Review B* **94**, 184406 (2016). DOI: 10.1103/PhysRevB.94.184406.

18. A. V. Kimel & M. Li. Writing magnetic memory with ultrashort light pulses. *Nature Reviews Materials* **4**, 189–200 (2019). DOI: 10.1038/s41578-019-0086-3.

19. I. Radu et al. Transient ferromagnetic-like state mediating ultrafast reversal of antiferromagnetically coupled spins. *Nature* **472**, 205–208 (2011). DOI: 10.1038/nature09901.

20. M. L. M. Lalieu, M. J. G. Peeters, S. R. R. Haenen, R. Lavrijsen & B. Koopmans. Deterministic all-optical switching of synthetic ferrimagnets using single femtosecond laser pulses. *Physical Review B* **96**, 220411 (2017). DOI: 10.1103/PhysRevB.96.220411.

21. S. S. Parkin, M. Hayashi & L. Thomas. Magnetic domain-wall racetrack memory. *Science* **320**, 190–194 (2008). DOI: 10.1126/science.1145799.

22. S. Parkin & S.-H. Yang. Memory on the racetrack. *Nature Nanotechnology* **10**, 195–198 (2015). DOI: 10.1038/nnano.2015.41.

23. F. E. Demirer et al. An integrated photonic device for on-chip magneto-optical memory reading. *Nanophotonics* (2022). DOI: 10.1515/nanoph-2022-0165.

24. R. Bläsing et al. Exchange coupling torque in ferrimagnetic Co/Gd bilayer maximized near angular momentum compensation temperature. *Nature Communications* **9**, 1–8 (2018). DOI: 10.1038/s41467-018-07373-w.

25. M. L. Lalieu, R. Lavrijsen & B. Koopmans. Integrating all-optical switching with spintronics. *Nature Communications* **10**, 110 (2019). DOI: 10.1038/s41467-018-08062-4.

26. T. Miyazaki & N. Tezuka. Giant magnetic tunneling effect in $Fe/Al_2O_3/Fe$ junction. *Journal of Magnetism and Magnetic Materials* **139**, L231–L234 (1995). DOI: 10.1016/0304-8853(95)90001-2.

27. J. S. Moodera, L. R. Kinder, T. M. Wong & R. Meservey. Large magnetoresistance at room temperature in ferromagnetic thin film tunnel junctions. *Physical Review Letters* **74**, 3273 (1995). DOI: 10.1103/PhysRevLett.74.3273.

28. S. Ikegawa, F. B. Mancoff & S. Aggarwal. Commercialization of MRAM – historical and future perspective. *2021 IEEE International Interconnect Technology Conference (IITC)*, 1–3 (2021). DOI: 10.1109/IITC51362.2021.9537434.

29. K. Garello et al. Manufacturable 300mm platform solution for field-free switching SOT-MRAM. *2019 Symposium on VLSI Circuits*, T194–T195 (2019). DOI: 10.23919/VLSIC.2019.8778100.

30. K. Cai et al. Ultrafast and energy-efficient spin–orbit torque switching in compensated ferrimagnets. *Nature Electronics* **3**, 37–42 (2020). DOI: 10.1038/s41928-019-0345-8.

31. J.-Y. Chen, L. He, J.-P. Wang & M. Li. All-optical switching of magnetic tunnel junctions with single subpicosecond laser pulses. *Physical Review Applied* **7**, 021001 (2017). DOI: 10.1103/PhysRevApplied.7.021001.

32. L. Wang et al. Picosecond optospintronic tunnel junctions. *Proceedings of the National Academy of Sciences* **119**, e2204732119 (2022). DOI: 10.1073/pnas.2204732119.

33. R. Soref. Tutorial: Integrated-photonic switching structures. *APL Photonics* **3**, 021101 (2018). DOI: 10.1063/1.5017968.

34. E. K. Sobolewska et al. Integration platform for optical switching of magnetic elements. *Active Photonic Platforms XII* **11461**, 54–72 (2020). DOI: 10.1117/12.2567662.

35. A. Ceballos et al. Role of element-specific damping in ultrafast, helicity-independent, all-optical switching dynamics in amorphous (Gd, Tb) Co thin films. *Physical Review B* **103**, 024438 (2021). DOI: 10.1103/PhysRevB.103.024438.

36. G. Malinowski et al. Control of speed and efficiency of ultrafast demagnetization by direct transfer of spin angular momentum. *Nature Physics* **4**, 855 (2008). DOI: 10.1038/nphys1092.

37. G. Eesley. Observation of nonequilibrium electron heating in copper. *Physical Review Letters* **51**, 2140 (1983). DOI: 10.1103/PhysRevLett.51.2140.

38. C. V. Shank. Investigation of ultrafast phenomena in the femtosecond time domain. *Science* **233**, 1276–1280 (1986). DOI: 10.1126/science.233.4770.1276.

39. R. Schoenlein, W. Lin, J. Fujimoto & G. Eesley. Femtosecond studies of nonequilibrium electronic processes in metals. *Physical Review Letters* **58**, 1680 (1987). DOI: 10.1103/PhysRevLett.58.1680.

40. M. H. Kryder. Magneto-optic recording technology. *Journal of Applied Physics* **57**, 3913–3918 (1985). DOI: 10.1063/1.334915.

41. A. Vaterlaus, T. Beutler & F. Meier. Spin-lattice relaxation time of ferromagnetic gadolinium determined with time-resolved spin-polarized photoemission. *Physical Review Letters* **67**, 3314 (1991). DOI: 10.1103/PhysRevLett.67.3314.

42. A. Vaterlaus, T. Beutler, D. Guarisco, M. Lutz & F. Meier. Spin-lattice relaxation in ferromagnets studied by time-resolved spin-polarized photoemission. *Physical Review B* **46**, 5280 (1992). DOI: 10.1103/PhysRevB.46.5280.

43. E. Beaurepaire, J.-C. Merle, A. Daunois & J.-Y. Bigot. Ultrafast spin dynamics in ferromagnetic nickel. *Physical Review Letters* **76**, 4250 (1996). DOI: 10.1103/PhysRevLett.76.4250.

44. E. Carpene et al. Dynamics of electron-magnon interaction and ultrafast demagnetization in thin iron films. *Physical Review B* **78**, 174422 (2008). DOI: 10.1103/PhysRevB.78.174422.

45. J. Güdde, U. Conrad, V. Jähnke, J. Hohlfeld & E. Matthias. Magnetization dynamics of Ni and Co films on Cu (001) and of bulk nickel surfaces. *Physical Review B* **59**, R6608 (1999). DOI: 10.1103/PhysRevB.59.R6608.

46. T. Ogasawara et al. General features of photoinduced spin dynamics in ferromagnetic and ferrimagnetic compounds. *Physical Review Letters* **94**, 087202 (2005). DOI: 10.1103/PhysRevLett.94.087202.

47. J. Walowski et al. Energy equilibration processes of electrons, magnons, and phonons at the femtosecond time scale. *Physical Review Letters* **101**, 237401 (2008). DOI: 10.1103/PhysRevLett.101.237401.

48. A. MELNIKOV ET AL. Nonequilibrium magnetization dynamics of gadolinium studied by magnetic linear dichroism in time-resolved 4f core-level photoemission. *Physical Review Letters* **100**, 107202 (2008). DOI: 10.1103/PhysRevLett.100.107202.

49. M. WIETSTRUK ET AL. Hot-electron-driven enhancement of spin-lattice coupling in Gd and Tb 4f ferromagnets observed by femtosecond x-ray magnetic circular dichroism. *Physical Review Letters* **106**, 127401 (2011). DOI: 10.1103/PhysRevLett.106.127401.

50. G. ZHANG & W. HÜBNER. Laser-induced ultrafast demagnetization in ferromagnetic metals. *Physical Review Letters* **85**, 3025 (2000). DOI: 10.1103/PhysRevLett.85.3025.

51. M. KRAUSS ET AL. Ultrafast demagnetization of ferromagnetic transition metals: The role of the Coulomb interaction. *Physical Review B* **80**, 180407 (2009). DOI: 10.1103/PhysRevB.80.180407.

52. M. BATTIATO, K. CARVA & P. M. OPPENEER. Superdiffusive spin transport as a mechanism of ultrafast demagnetization. *Physical Review Letters* **105**, 027203 (2010). DOI: 10.1103/PhysRevLett.105.027203.

53. Ł. CYWIŃSKI & L.J. SHAM. Ultrafast demagnetization in the sp-d model: A theoretical study. *Physical Review B* **76**, 045205 (2007). DOI: 10.1103/PhysRevB.76.045205.

54. B. KOOPMANS, J. RUIGROK, F. DALLA LONGA & W. DE JONGE. Unifying ultrafast magnetization dynamics. *Physical Review Letters* **95**, 267207 (2005). DOI: 10.1103/PhysRevLett.95.267207.

55. B. KOOPMANS ET AL. Explaining the paradoxical diversity of ultrafast laser-induced demagnetization. *Nature Materials* **9**, 259 (2010). DOI: 10.1038/nmat2593.

56. C. DORNES ET AL. The ultrafast Einstein–de Haas effect. *Nature* **565**, 209–212 (2019). DOI: 10.1038/s41586-018-0822-7.

57. S. R. TAUCHERT ET AL. Polarized phonons carry angular momentum in ultrafast demagnetization. *Nature* **602**, 73–77 (2022). DOI: 10.1038/s41586-021-04306-4.

58. G. ZHANG, W. HÜBNER, E. BEAUREPAIRE & J.-Y. BIGOT. Laser-induced ultrafast demagnetization: Femtomagnetism, a new frontier? *Spin Dynamics in Confined Magnetic Structures I,* 245–289 (2002). DOI: 10.1007/3-540-40907-6_8.

59. L. MAYER. Curie-point writing on magnetic films. *Journal of Applied Physics* **29**, 1003–1003 (1958). DOI: https://doi.org/10.1063/1.1723319.

60. L. MAYER. Magnetic writing with an electron beam. *Journal of Applied Physics* **29**, 1454–1456 (1958). DOI: 10.1063/1.1722967.

61.   G. LEWICKI. Curie-point switching in Mn-Bi films. *IEEE Transactions on Magnetics* **5,** 298–299 (1969). DOI: 10.1109/TMAG.1969.1066591.

62.   D. TREVES, R. P. HUNT & B. DICKEY. Laser-beam recording on a magnetic film. *Journal of Applied Physics* **40,** 972–973 (1969). DOI: 10.1063/1.1657804.

63.   R. S. MEZRICH. Curie-point writing of magnetic holograms on MnBi. *Applied Physics Letters* **14,** 132–134 (1969). DOI: 10.1063/1.1652746.

64.   N. GOLDBERG. A high-density magneto-optic memory. *IEEE Transactions on Magnetics* **3,** 605–611 (1967). DOI: 10.1109/TMAG.1967.1066154.

65.   J. CHANG, J. DILLON JR. & U. GIANOLA. Magneto-optical variable memory based upon the properties of a transparent ferrimagnetic garnet at its compensation temperature. *Journal of Applied Physics* **36,** 1110–1111 (1965). DOI: 10.1063/1.1714122.

66.   R. MACDONALD & J. BECK. Magneto-Optical Recording. *Journal of Applied Physics* **40,** 1429–1435 (1969). DOI: 10.1063/1.1657706.

67.   M. HARTMANN, J. BRAAT & B. JACOBS. Erasable magneto-optical recording media. *IEEE Transactions on Magnetics* **20,** 1013–1018 (1984). DOI: 10.1109/TMAG.1984.1063168.

68.   K. A. IMMINK & J. J. BRAAT. Experiments toward an erasable compact disc digital audio system. *Journal of the Audio Engineering Society* **32,** 531–538 (1984). URL: www.aes.org/e-lib/browse.cfm?elib=4492.

69.   N. IMAMURA, S. TANAKA, F. TANAKA & Y. NAGAO. Magneto-optical recording on amorphous films. *IEEE Transactions on Magnetics* **21,** 1607–1612 (1985). DOI: 10.1109/TMAG.1985.1063924.

70.   P. HANSEN. Magneto-optical recording materials and technologies. *Journal of Magnetism and Magnetic Materials* **83,** 6–12 (1990). DOI: 10.1016/0304-8853(90)90411-l.

71.   S. TSUNASHIMA. Magneto-optical recording. *Journal of Physics D: Applied Physics* **34,** R87 (2001). DOI: 10.1088/0022-3727/34/17/201.

72.   R. E. ROTTMAYER ET AL. Heat-assisted magnetic recording. *IEEE Transactions on Magnetics* **42,** 2417–2421 (2006). DOI: 10.1109/TMAG.2006.879572.

73.   M. H. KRYDER ET AL. Heat assisted magnetic recording. *Proceedings of the IEEE* **96,** 1810–1835 (2008). DOI: 10.1109/JPROC.2008.2004315.

74.   A. Q. WU ET AL. HAMR areal density demonstration of 1+ Tbpsi on spinstand. *IEEE Transactions on Magnetics* **49,** 779–782 (2013). DOI: 10.1109/TMAG.2012.2219513.

75. A. R. KHORSAND ET AL. Role of magnetic circular dichroism in all-optical magnetic recording. *Physical Review Letters* **108**, 127205 (2012). DOI: 10.1103/PhysRevLett.108.127205.

76. Y. HASHIMOTO ET AL. Ultrafast time-resolved magneto-optical imaging of all-optical switching in GdFeCo with femtosecond time-resolution and a μm spatial-resolution. *Review of Scientific Instruments* **85**, 063702 (2014). DOI: 10.1063/1.4880015.

77. M. PEETERS, Y. VAN BALLEGOOIE & B. KOOPMANS. Influence of magnetic fields on ultrafast laser-induced switching dynamics in Co/Gd bilayers. *Physical Review B* **105**, 014429 (2022). DOI: 10.1103/PhysRevB.105.014429.

78. F. STEINBACH ET AL. Accelerating double pulse all-optical write/erase cycles in metallic ferrimagnets. *Applied Physics Letters* **120**, 112406 (2022). DOI: 10.1063/5.0080351.

79. U. ATXITIA, P. NIEVES & O. CHUBYKALO-FESENKO. Landau-Lifshitz-Bloch equation for ferrimagnetic materials. *Physical Review B* **86**, 104414 (2012). DOI: 10.1103/PhysRevB.86.104414.

80. J. H. MENTINK ET AL. Ultrafast spin dynamics in multisublattice magnets. *Physical Review Letters* **108**, 057202 (2012). DOI: 10.1103/PhysRevLett.108.057202.

81. S. WIENHOLDT, D. HINZKE, K. CARVA, P. M. OPPENEER & U. NOWAK. Orbital-resolved spin model for thermal magnetization switching in rare-earth-based ferrimagnets. *Physical Review B* **88**, 020406 (2013). DOI: 10.1103/PhysRevB.88.020406.

82. A. J. SCHELLEKENS & B. KOOPMANS. Microscopic model for ultrafast magnetization dynamics of multisublattice magnets. *Physical Review B* **87**, 020407 (2013). DOI: 10.1103/PhysRevB.87.020407.

83. C. GRAVES ET AL. Nanoscale spin reversal by non-local angular momentum transfer following ultrafast laser excitation in ferrimagnetic GdFeCo. *Nature Materials* **12**, 293–298 (2013). DOI: 10.1038/nmat3597.

84. V. GRIDNEV. Ultrafast heating-induced magnetization switching in ferrimagnets. *Journal of Physics: Condensed Matter* **28**, 476007 (2016). DOI: 10.1088/0953-8984/28/47/476007.

85. V. GRIDNEV. Ferromagneticlike states and all-optical magnetization switching in ferrimagnets. *Physical Review B* **98**, 014427 (2018). DOI: 10.1103/PhysRevB.98.014427.

86. C. S. DAVIES ET AL. Pathways for single-shot all-optical switching of magnetization in ferrimagnets. *Physical Review Applied* **13,** 024064 (2020). DOI: 10.1103/PhysRevApplied.13.024064.

87. A. EL-GHAZALY ET AL. Ultrafast magnetization switching in nanoscale magnetic dots. *Applied Physics Letters* **114,** 232407 (2019). DOI: 10.1063/1.5098453.

88. Y. XU ET AL. Ultrafast magnetization manipulation using single femtosecond light and hot-electron pulses. *Advanced Materials* **29,** 1703474 (2017). DOI: 10.1002/adma.201703474.

89. M. BEENS, M. L. M. LALIEU, A. J. DEENEN, R. A. DUINE & B. KOOPMANS. Comparing all-optical switching in synthetic-ferrimagnetic multilayers and alloys. *Physical Review B* **100,** 220409 (2019). DOI: 10.1103/PhysRevB.100.220409.

90. S. ALEBRAND ET AL. Light-induced magnetization reversal of high-anisotropy TbCo alloy films. *Applied Physics Letters* **101,** 162408 (2012). DOI: 10.1063/1.4759109.

91. L. AVILÉS-FÉLIX ET AL. Integration of Tb/Co multilayers within optically switchable perpendicular magnetic tunnel junctions. *AIP Advances* **9,** 125328 (2019). DOI: 10.1063/1.5129821.

92. L. AVILÉS-FÉLIX ET AL. Single-shot all-optical switching of magnetization in Tb/Co multilayer-based electrodes. *Scientific Reports* **10,** 1–8 (2020). DOI: 10.1038/s41598-020-62104-w.

93. B. FRIETSCH ET AL. The role of ultrafast magnon generation in the magnetization dynamics of rare-earth metals. *Science Advances* **6,** eabb1601 (2020). DOI: 10.1126/sciadv.abb1601.

94. Y. TSERKOVNYAK, A. BRATAAS & G. E. BAUER. Enhanced Gilbert damping in thin ferromagnetic films. *Physical Review Letters* **88,** 117601 (2002). DOI: 10.1103/PhysRevLett.88.117601.

95. Y. TSERKOVNYAK, A. BRATAAS & G. E. BAUER. Spin pumping and magnetization dynamics in metallic multilayers. *Physical Review B* **66,** 224403 (2002). DOI: 10.1103/PhysRevB.66.224403.

96. M. COSTACHE, M. SLADKOV, S. WATTS, C. VAN DER WAL & B. VAN WEES. Electrical detection of spin pumping due to the precessing magnetization of a single ferromagnet. *Physical Review Letters* **97,** 216603 (2006). DOI: 10.1103/PhysRevLett.97.216603.

97. J. KIMLING & D. G. CAHILL. Spin diffusion induced by pulsed-laser heating and the role of spin heat accumulation. *Physical Review B* **95**, 014402 (2017). DOI: 10.1103/PhysRevB.95.014402.

98. M. BATTIATO, K. CARVA & P. M. OPPENEER. Theory of laser-induced ultrafast superdiffusive spin transport in layered heterostructures. *Physical Review B* **86**, 024404 (2012). DOI: 10.1103/PhysRevB.86.024404.

99. G.-M. CHOI, B.-C. MIN, K.-J. LEE & D. G. CAHILL. Spin current generated by thermally driven ultrafast demagnetization. *Nature Communications* **5**, 4334 (2014). DOI: 10.1038/ncomms5334.

100. G.-M. CHOI & B.-C. MIN. Laser-driven spin generation in the conduction bands of ferrimagnetic metals. *Physical Review B* **97**, 014410 (2018). DOI: 10.1103/PhysRevB.97.014410.

101. M. BEENS, R.A. DUINE & B. KOOPMANS. s- d model for local and nonlocal spin dynamics in laser-excited magnetic heterostructures. *Physical Review B* **102**, 054442 (2020). DOI: 10.1103/PhysRevB.102.054442.

102. E. TURGUT ET AL. Controlling the competition between optically induced ultrafast spin-flip scattering and spin transport in magnetic multilayers. *Physical Review Letters* **110**, 197201 (2013). DOI: 10.1103/PhysRevLett.110.197201.

103. A. J. SCHELLEKENS, N. DE VRIES, J. LUCASSEN & B. KOOPMANS. Exploring laser-induced interlayer spin transfer by an all-optical method. *Physical Review B* **90**, 104429 (2014). DOI: 10.1103/PhysRevB.90.104429.

104. A. MELNIKOV ET AL. Ultrafast transport of laser-excited spin-polarized carriers in Au/Fe/MgO (001). *Physical Review Letters* **107**, 076601 (2011). DOI: 10.1103/PhysRevLett.107.076601.

105. T. HUISMAN ET AL. Femtosecond control of electric currents in metallic ferromagnetic heterostructures. *Nature nanotechnology* **11**, 455–458 (2016). DOI: 10.1038/nnano.2015.331.

106. T. HUISMAN ET AL. Spin-photo-currents generated by femtosecond laser pulses in a ferrimagnetic GdFeCo/Pt bilayer. *Applied physics letters* **110**, 072402 (2017). DOI: 10.1063/1.4976202.

107. T. S. SEIFERT ET AL. Femtosecond formation dynamics of the spin Seebeck effect revealed by terahertz spectroscopy. *Nature Communications* **9**, 1–11 (2018). DOI: 10.1038/s41467-018-05135-2.

108. P. Jiménez-Cavero et al. Transition of laser-induced terahertz spin currents from torque-to conduction-electron-mediated transport. *Physical Review B* **105**, 184408 (2022). DOI: 10.1103/PhysRevB.105.184408.

109. M. L. M. Lalieu, P. L. J. Helgers & B. Koopmans. Absorption and generation of femtosecond laser-pulse excited spin currents in noncollinear magnetic bilayers. *Physical Review B* **96**, 014417 (2017). DOI: 10.1103/PhysRevB.96.014417.

110. T. Lichtenberg, M. Beens, M. H. Jansen, B. Koopmans & R. A. Duine. Probing optically induced spin currents using terahertz spin waves in noncollinear magnetic bilayers. *Physical Review B* **105**, 144416 (2022). DOI: 10.1103/PhysRevB.105.144416.

111. S. Iihama et al. Single-shot multi-level all-optical magnetization switching mediated by spin transport. *Advanced Materials* **30**, 1804004 (2018). DOI: 10.1002/adma.201804004.

112. Q. Remy et al. Energy efficient control of ultrafast spin current to induce single femtosecond pulse switching of a ferromagnet. *Advanced Science* **7**, 2001996 (2020). DOI: 10.1002/advs.202001996.

113. J. Igarashi et al. Engineering single-shot all-optical switching of ferromagnetic materials. *Nano Letters* **20**, 8654–8660 (2020). DOI: 10.1021/acs.nanolett.0c03373.

114. M. Faraday. On the magnetization of light and the illumination of magnetic lines of force. *Philosophical Transactions of the Royal Society of London* **136**, 1–20 (1846). DOI: 10.5479/sil.389644.mq591299.

115. J. Kerr. On rotation of the plane of polarization by reflection from the pole of a magnet. *The London, Edinburgh, and Dublin Philosophical Magazine and Journal of Science* **3**, 321–343 (1877). DOI: 10.1080/14786447708639245.

116. Z. Qiu & S. D. Bader. Surface magneto-optic Kerr effect. *Review of Scientific Instruments* **71**, 1243–1255 (2000). DOI: 10.1063/1.1150496.

117. M. L. Lalieu & B. Koopmans. Optical studies of magnetically ordered metallic thin films. *Handbook of Magnetism and Magnetic Materials*, 1–71 (2021). DOI: 10.1007/978-3-030-63101-7_10-2.

118. M. Freiser. A survey of magnetooptic effects. *IEEE Transactions on Magnetics* **4**, 152–161 (1968). DOI: 10.1109/TMAG.1968.1066210.

119. K. Hipps & G. Crosby. Applications of the photoelastic modulator to polarization spectroscopy. *Journal of Physical Chemistry* **83**, 555–562 (1979). DOI: 10.1021/j100468a001.

120. F. DALLA LONGA. PhD Thesis. *Eindhoven University of Technology* (2008). DOI: 10.6100/IR635203.

121. A. J. SCHELLEKENS. PhD Thesis. *Eindhoven University of Technology* (2014). DOI: 10.6100/IR770953.

122. M. L. M. LALIEU. PhD Thesis. *Eindhoven University of Technology* (2019). URL: pure.tue.nl/ws/files/118304457/20190311_Lalieu.

123. B. KOOPMANS, M. VAN KAMPEN, J. KOHLHEPP & W. DE JONGE. Ultrafast magneto-optics in nickel: Magnetism or optics? *Physical Review Letters* **85**, 844 (2000). DOI: 10.1103/PhysRevLett.85.844.

124. R. SCHÄFER. Investigation of domains and dynamics of domain walls by the magneto-optical Kerr-effect. *Handbook of magnetism and advanced magnetic materials* (2007). DOI: 10.1002/9780470022184.hmm310.

125. Y. XU ET AL. From single to multiple pulse all-optical switching in GdFeCo thin films. *Physical Review B* **100**, 064424 (2019). DOI: 10.1103/PhysRevB.100.064424.

126. Y. L. W. VAN HEES, B. KOOPMANS & R. LAVRIJSEN. Toward high all-optical data writing rates in synthetic ferrimagnets. *Applied Physics Letters* **120**, 252401 (2022). DOI: 10.1063/5.0094540.

127. L. B. P. J. LE GUYADER ET AL. Demonstration of laser induced magnetization reversal in GdFeCo nanostructures. *Applied Physics Letters* **101**, 022410 (2012). DOI: 10.1063/1.4733965.

128. M. SAVOINI ET AL. Highly efficient all-optical switching of magnetization in GdFeCo microstructures by interference-enhanced absorption of light. *Physical Review B* **86**, 140404 (2012). DOI: 10.1103/PhysRevB.86.140404.

129. U. ATXITIA & T. OSTLER. Ultrafast double magnetization switching in GdFeCo with two picosecond-delayed femtosecond pump pulses. *Applied Physics Letters* **113**, 062402 (2018). DOI: 10.1063/1.5044272.

130. S. WANG ET AL. Dual-shot dynamics and ultimate frequency of all-optical magnetic recording on GdFeCo. *Light: Science & Applications* **10**, 1–8 (2021). DOI: 10.1038/s41377-020-00451-z.

131. T. H. PHAM ET AL. Very large domain wall velocities in Pt/Co/GdOx and Pt/Co/Gd trilayers with Dzyaloshinskii-Moriya interaction. *Europhysics Letters* **113**, 67001 (2016). DOI: 10.1209/0295-5075/113/67001.

132. L. WANG, Y. L. W. VAN HEES, R. LAVRIJSEN, W. ZHAO & B. KOOPMANS. Enhanced all-optical switching and domain wall velocity in annealed synthetic-ferrimagnetic multilayers. *Applied Physics Letters* **117**, 022408 (2020). DOI: 10.1063/5.0012269.

133. M. Beens, M. L. Lalieu, R. A. Duine & B. Koopmans. The role of intermixing in all-optical switching of synthetic-ferrimagnetic multilayers. *AIP Advances* **9**, 125133 (2019). DOI: 10.1063/1.5129892.

134. R. Moreno, T. Ostler, R. Chantrell & O. Chubykalo-Fesenko. Conditions for thermally induced all-optical switching in ferrimagnetic alloys: Modeling of TbCo. *Physical Review B* **96**, 014409 (2017). DOI: 10.1103/PhysRevB.96.014409.

135. T. Lichtenberg, Y.L.W. van Hees et al. Probing laser-induced spin-current generation in synthetic ferrimagnets using spin waves. *Phys. Rev. B* **106**, 094436 (2022). DOI: 10.1103/PhysRevB.106.094436.

136. D. Rudolf et al. Ultrafast magnetization enhancement in metallic multilayers driven by superdiffusive spin current. *Nature Communications* **3**, 1037 (2012). DOI: 10.1038/ncomms2029.

137. J. Hurst, P.-A. Hervieux & G. Manfredi. Spin current generation by ultrafast laser pulses in ferromagnetic nickel films. *Physical Review B* **97**, 014424 (2018). DOI: 10.1103/PhysRevB.97.014424.

138. J. K. Dewhurst, P. Elliott, S. Shallcross, E. K. Gross & S. Sharma. Laser-induced intersite spin transfer. *Nano Letters* **18**, 1842–1848 (2018). DOI: 10.1021/acs.nanolett.7b05118.

139. R. Rouzegar et al. Laser-induced terahertz spin transport in magnetic nanostructures arises from the same force as ultrafast demagnetization. *arXiv preprint* (2021). DOI: 10.48550/arXiv.2103.11710.

140. Y. L. W. van Hees, P. van de Meugheuvel, B. Koopmans & R. Lavrijsen. Deterministic all-optical magnetization writing facilitated by non-local transfer of spin angular momentum. *Nature Communications* **11**, 1–7 (2020). DOI: 10.1038/s41467-020-17676-6.

141. D. Haskel et al. Enhanced interfacial magnetic coupling of Gd/Fe multilayers. *Physical Review Letters* **87**, 207201 (2001). DOI: 10.1103/PhysRevLett.87.207201.

142. A. J. Schellekens, K. Kuiper, R. De Wit & B. Koopmans. Ultrafast spin-transfer torque driven by femtosecond pulsed-laser excitation. *Nature Communications* **5**, 1–7 (2014). DOI: 10.1038/ncomms5333.

143. I. Razdolski et al. Nanoscale interface confinement of ultrafast spin transfer torque driving non-uniform spin dynamics. *Nature Communications* **8**, 1–5 (2017). DOI: 10.1038/ncomms15007.

144. E.G. Tveten, A. Brataas & Y. Tserkovnyak. Electron-magnon scattering in magnetic heterostructures far out of equilibrium. *Physical Review B* **92**, 180412(R) (2015). DOI: 10.1103/PhysRevB.92.180412.

145. I.-H. Shin, B.-C. Min, B.-K. Ju & G.-M. Choi. Ultrafast spin current generated by electron–magnon scattering in bulk of ferromagnets. *Japanese Journal of Applied Physics* **57**, 090307 (2018). DOI: 10.7567/JJAP.57.090307.

146. H. Eichler, D. Langhans & F. Massmann. Coherence peaks in picosecond sampling experiments. *Optics Communications* **50**, 117–122 (1984). DOI: 10.1016/0030-4018(84)90147-0.

147. C. C. Katsidis & D. I. Siapkas. General transfer-matrix method for optical multilayer systems with coherent, partially coherent, and incoherent interference. *Applied Optics* **41**, 3978–3987 (2002). DOI: 10.1364/AO.41.003978.

148. C. Eyrich et al. Effects of substitution on the exchange stiffness and magnetization of Co films. *Physical Review B* **90**, 235408 (2014). DOI: 10.1103/PhysRevB.90.235408.

149. A. Manchon, Q. Li, L. Xu & S. Zhang. Theory of laser-induced demagnetization at high temperatures. *Physical Review B* **85**, 064408 (2012). DOI: 10.1103/PhysRevB.85.064408.

150. J. A. De Jong et al. Coherent control of the route of an ultrafast magnetic phase transition via low-amplitude spin precession. *Physical Review Letters* **108**, 157601 (2012). DOI: 10.1103/PhysRevLett.108.157601.

151. A. Hassdenteufel et al. Thermally assisted all-optical helicity dependent magnetic switching in amorphous $Fe_{100-x}Tb_x$ alloy films. *Advanced Materials* **25**, 3122–3128 (2013). DOI: 10.1002/adma.201300176.

152. C. H. Lambert et al. All-optical control of ferromagnetic thin films and nanostructures. *Science* **345**, 1337–1340 (2014). DOI: 10.1126/science.1253493.

153. S. Mangin et al. Engineered materials for all-optical helicity-dependent magnetic switching. *Nature Materials* **13**, 286 (2014). DOI: 10.1038/nmat3864.

154. M. S. El Hadri et al. Two types of all-optical magnetization switching mechanisms using femtosecond laser pulses. *Physical Review B* **94**, 064412 (2016). DOI: 10.1103/PhysRevB.94.064412.

155. K. T. Yamada et al. Efficient all-optical helicity dependent switching of spins in a Pt/Co/Pt film by a dual-pulse excitation. *Frontiers in Nanotechnology*, 6 (2022). DOI: 10.3389/fnano.2022.765848.

156. Y. QUESSAB ET AL. Resolving the role of magnetic circular dichroism in multishot helicity-dependent all-optical switching. *Physical Review B* **100**, 024425 (2019). DOI: 10.1103/PhysRevB.100.024425.

157. C. BANERJEE ET AL. Single pulse all-optical toggle switching of magnetization without gadolinium in the ferrimagnet Mn_2Ru_xGa. *Nature Communications* **11**, 1–6 (2020). DOI: 10.1038/s41467-020-18340-9.

158. K. VAHAPLAR ET AL. Ultrafast path for optical magnetization reversal via a strongly nonequilibrium state. *Physical Review Letters* **103**, 117201 (2009). DOI: 10.1103/PhysRevLett.103.117201.

159. F. J. JEDEMA, A. FILIP & B. VAN WEES. Electrical spin injection and accumulation at room temperature in an all-metal mesoscopic spin valve. *Nature* **410**, 345 (2001). DOI: 10.1038/35066533.

160. A. ALEKHIN ET AL. Femtosecond spin current pulses generated by the nonthermal spin-dependent Seebeck effect and interacting with ferromagnets in spin valves. *Physical Review Letters* **119**, 017202 (2017). DOI: 10.1103/PhysRevLett.119.017202.

161. T.-M. LIU ET AL. Nanoscale confinement of all-optical magnetic switching in TbFeCo-competition with nanoscale heterogeneity. *Nano Letters* **15**, 6862–6868 (2015). DOI: 10.1021/acs.nanolett.5b02743.

162. S. J. BYRNES. Multilayer optical calculations. *arXiv preprint* (2016). DOI: 10.48550/arXiv.1603.02720.

163. T. ROTH ET AL. Temperature dependence of laser-induced demagnetization in Ni: A key for identifying the underlying mechanism. *Physical Review X* **2**, 021006 (2012). DOI: 10.1103/PhysRevX.2.021006.

164. A. HERNANDO ET AL. Curie-temperature enhancement of ferromagnetic phases in nanoscale heterogeneous systems. *Physical Review B* **53**, 8223 (1996). DOI: 10.1103/PhysRevB.53.8223.

165. L. LE GUYADER ET AL. Deterministic character of all-optical magnetization switching in GdFe-based ferrimagnetic alloys. *Physical Review B* **93**, 134402 (2016). DOI: 10.1103/PhysRevB.93.134402.

166. A. CAO, Y. L. W. VAN HEES, R. LAVRIJSEN, W. ZHAO & B. KOOPMANS. Dynamics of all-optically switched magnetic domains in Co/Gd heterostructures with Dzyaloshinskii-Moriya interaction. *Physical Review B* **102**, 104412 (2020). DOI: 10.1103/PhysRevB.102.104412.

167. M. COLARIETI-TOSTI ET AL. Origin of magnetic anisotropy of Gd metal. *Physical Review Letters* **91**, 157201 (2003). DOI: 10.1103/PhysRevLett.91.157201.

168. N. Nishimura et al. Magnetic tunnel junction device with perpendicular magnetization films for high-density magnetic random access memory. *Journal of Applied Physics* **91**, 5246–5249 (2002). DOI: 10.1063/1.1459605.

169. S. Miyanishi et al. High-density laser-assisted magnetic recording on TbFeCo media with an Al underlayer. *Journal of Applied Physics* **93**, 7801–7803 (2003). DOI: 10.1063/1.1557336.

170. A. R. Khorsand et al. Element-specific probing of ultrafast spin dynamics in multisublattice magnets with visible light. *Physical Review Letters* **110**, 107205 (2013). DOI: 10.1103/PhysRevLett.110.107205.

171. S. Alebrand et al. Subpicosecond magnetization dynamics in TbCo alloys. *Physical Review B* **89**, 144404 (2014). DOI: 10.1103/PhysRevB.89.144404.

172. Z. Xu et al. Giant Spin Hall Effect in Cu–Tb Alloy Thin Films. *ACS Applied Materials & Interfaces* **12**, 32898–32904 (2020). DOI: 10.1021/acsami.0c07441.

173. P. Haazen et al. Domain wall depinning governed by the spin Hall effect. *Nature Materials* **12**, 299–303 (2013). DOI: 10.1038/nmat3553.

174. N. Ashcroft & N. Mermin. Solid State Physics. *Saunders College Publishing* (1976). ISBN: 0-03-083993-9.

175. D. O. Ignatyeva et al. Plasmonic layer-selective all-optical switching of magnetization with nanometer resolution. *Nature Communications* **10**, 1–7 (2019). DOI: 10.1038/s41467-019-12699-0.

176. P. Li, M. J. G. Peeters, Y. L. W. van Hees, R. Lavrijsen & B. Koopmans. Ultra-low energy threshold engineering for all-optical switching of magnetization in dielectric-coated Co/Gd based synthetic-ferrimagnet. *Applied Physics Letters* **119**, 252402 (2021). DOI: 10.1063/5.0077491.

177. J. Liu. Simple technique for measurements of pulsed Gaussian-beam spot sizes. *Optics Letters* **7**, 196–198 (1982). DOI: 10.1364/OL.7.000196.

178. *Refractive index data from Sopra S.A., Accessed: 2022-05-01* URL: www.sspectra.com/sopra.html.

179. L. A. Akashev, N. A. Popov & V. G. Shevchenko. Optical properties of gadolinium in the condensed state. *High Temperature* **57**, 49–53 (2019). DOI: 10.1134/S0018151X18060032.

180. Y. Tserkovnyak, A. Brataas, G. E. Bauer & B. I. Halperin. Nonlocal magnetization dynamics in ferromagnetic heterostructures. *Reviews of Modern Physics* **77**, 1375 (2005). DOI: 10.1103/RevModPhys.77.1375.

181.   S. Vernon, S. Lindsay & M. Stearns. Brillouin scattering from thermal magnons in a thin Co film. *Physical Review B* **29**, 4439 (1984). doi: 10.1103/PhysRevB.29.4439.

182.   M. Isasa, E. Villamor, L. E. Hueso, M. Gradhand & F. Casanova. Temperature dependence of spin diffusion length and spin Hall angle in Au and Pt. *Physical Review B* **91**, 024402 (2015). doi: 10.1103/PhysRevB.91.024402.